Influence of non-erodible particles on aeolian erosion

Maria Clara Schuwartz Ferreira

ANNÉE 2017

THÈSE / UNIVERSITÉ DE RENNES 1
sous le sceau de l'Université Bretagne Loire

En Cotutelle Internationale avec
Universidade Federal do Espírito Santo, Brésil

pour le grade de

DOCTEUR DE L'UNIVERSITÉ DE RENNES 1

Mention : Physique

École doctorale Science de la Matière

présentée par

Maria Clara Schuwartz Ferreira CALIMAN

préparée à l'unité de recherche IPR – UMR CNRS 6251
Institut de Physique de Rennes
UFR Structure et Propriétés de la Matière

Influence de particules non-erodables dans le processus d'érosion éolienne

Thèse soutenue à Rennes
le 5 janvier 2017

devant le jury composé de :

Bruno ANDREOTTI
Professeur / *Rapporteur*

Murilo PEREIRA DE ALMEIDA
Professeur / *Rapporteur*

Hassan PEERHOSSAINI
Professeur / *Examinateur*

Neyval COSTA REIS JUNIOR
Professeur / *Examinateur*

Taciana TOLEDO DE ALMEIDA ALBUQUERQUE
Professeur / *Examinatrice*

Ahmed OULD EL MOCTAR
Professeur / *Directeur de thèse*

Alexandre VALANCE
Professeur / *Directeur de thèse*

Jane Méri SANTOS
Professeur / *Directrice de thèse*

Jean-Luc HARION
Professeur / *Directeur de thèse*

UNIVERSIDADE FEDERAL DO ESPÍRITO SANTO
CENTRO TECNOLÓGICO
PROGRAMA DE PÓS-GRADUAÇÃO EM ENGENHARIA AMBIENTAL

MARIA CLARA SCHUWARTZ FERREIRA CALIMAN

Influence of non-erodible particles on aeolian erosion

Influência das partículas não-erodíveis na erosão eólica

Vitória
2017

MARIA CLARA SCHUWARTZ FERREIRA CALIMAN

Influence of non-erodible particles on aeolian erosion

Influência das partículas não-erodíveis na erosão eólica

Thesis submitted to Programa de Pós-Graduação em Engenharia Ambiental of Centro Tecnológico da Universidade Federal do Espírito Santo, for the degree of Doctor of Science in Environmental Engineering.

Supervisors: Prof. Alexandre Valance, PhD, Prof. Jane Méri Santos, PhD.
Co-supervisors: Prof. Ahmed Ould El Moctar, PhD, Prof. Jean-Luc Harion, PhD.

Vitória
2017

Dados Internacionais de Catalogação-na-publicação (CIP)
(Biblioteca Setorial Tecnológica,
Universidade Federal do Espírito Santo, ES, Brasil)

Caliman, Maria Clara Schuwartz Ferreira, 1984-
C153i Influência das partículas não-erodíveis na erosão eólica / Maria Clara Schuwartz Ferreira Caliman. – 2017.
124 f. : il.

Orientador: Jane Méri Santos.
Orientador: Alexandre Valance.
Coorientador: Ahmed Ould El Moctar.
Coorientador: Jean-Luc Harion.
Tese (Doutorado em Engenharia Ambiental) – Universidade Federal do Espírito Santo, Centro Tecnológico.

1. Erosão eólica. 2. Partículas. 3. Pavimentos. 4. Erosão – Modelos. 5. Materiais granulados – Armazenamento. 6. Emissões fugitivas. I. Santos, Jane Méri. II. Valance, Alexandre. III. El Moctar, Ahmed Ould. IV. Harion, Jean-Luc. V. Universidade Federal do Espírito Santo. Centro Tecnológico. VI. Título.

CDU: 628

UNIVERSIDADE FEDERAL DO ESPÍRITO SANTO
CENTRO TECNOLÓGICO
PROGRAMA DE PÓS-GRADUAÇÃO EM ENGENHARIA AMBIENTAL

"INFLUENCE OF NON-ERODIBLE PARTICLES ON AEOLIAN EROSION".

MARIA CLARA SCHUWARTZ FERREIRA CALIMAN

Banca Examinadora:

Profa. Dra. Jane Méri Santos
Orientadora – DEA/CT/UFES

Prof. Dr. Alexandre Valance
Orientador – Université de Rennes 1 - França

Prof. Dr. Ahmed Ould el Moctar
Coorientador – Université de Nante - França

Prof. Dr. Jean-Luc Harion
Coorientador – École des Mines de Douai - França

Prof. Neyval Costa Reis Jr.
Examinador Interno – DEA-CT-UFES

Profa. Dra. Taciana T. de Almeida Albuquerque
Examinadora Interna – PPGEA-UFES

Prof. Dr. Murilo Pereira de Almeida
Examinador Externo – UFC

Prof. Dr. Bruno Andreotti
Examinador Externo - Université Paris Didero – França

Prof. Dr. Hassan Peerhossaini
Examinador Externo - Université Paris Didero - França

A defesa foi realizada em conformidade com o acordo de cotutela do Programa de Pós-graduação em Engenharia Ambiental, da Universidade Federal do Espírito Santo com o Institut de Physique de Rennes, da Université de Rennes 1 – França.

Em conformidade com as normas prescritas na portaria normativa nº. 02/2016, as assinaturas dos membros da banca (Prof. Dr. Alexandre Valance; Prof. Dr. Ahmed Ould el Moctar; Prof. Dr. Jean-Luc Harion; Prof. Dr. Bruno Andreotti e o Prof. Dr. Hassan Peerhossaini) foram representadas neste documento pela respectiva assinatura da presidente da comissão julgadora, a Profa. Dra. Jane Méri Santos.

Coordenador do PPGEA, em exercício: Prof. Dr. Antônio Sérgio Ferreira Mendonça
UNIVERSIDADE FEDERAL DO ESPÍRITO SANTO
Vitória, ES, 05 de Janeiro de 2017.

Acknowledgements

I would like to express my sincere gratitude to Prof. Jane Méri Santos for her patience, encouragement and immense knowledge. Without her valuable guidance, this thesis would not have been possible.

I also wish to deeply thank Prof. Jean-Luc Harion for the insights into the beginning steps of the research and the continuous support, fundamental to the development of this work.

My sincere thanks go to Prof. Ahmed Ould El Moctar, Prof. Alexandre Valance and Prof. Pascal Dupont for sharing knowledge and expertise with me. They really inspired me to be curious about the research and it was a privilege to be part of their team during my stay in France.

I also wish to thank Prof. Bruno Andreotti, Prof. Hassan Peerhossaini, Prof. Murilo Pereira de Almeida, Prof. Neyval Costa Reis Junior and Prof. Taciana Toledo de Almeida Albuquerque, members of the jury of this thesis, for having provide insightful discussions about the research.

A special gratitude goes to Prof. Bruno Furieri. Bruno was there from the first beginning, helping me all the time during the research. After these years, he became a great friend and a role model for a scientist.

I would like to acknowledge the Brazilian Government Agency Capes for the funding support that enabled the collaboration agreement between University of Rennes and Federal University of Espírito Santo.

I take this opportunity to express gratitude to all of the staff members from Federal University of Espírito Santo, Mines Douai and University of Nantes, with a special mention to Rose and Chrystele, that with a lot of goodwill and sympathy facilitated my daily life and helped with the experiments.

I would like to thank my dear friends from UFES and fellow doctoral students, especially Bruno, Cristina, Enilene, Edilson, Fernanda, Israel and Lya, for their cooperation and feedback. It was great sharing the laboratory with all of you during these years.

I am also deeply grateful to the Federal Institute of Espírito Santo and all my colleagues from the Mathematics Department for giving me the opportunity to dedicate to my PhD in full time, granting me license from my activities.

Special thanks to my parents Maria José and José Armínio, my brothers André and Antônio Luiz and all my family for their unconditional love, affection and encouragement. I am also grateful to all my friends for supporting me spiritually throughout writing this thesis and my life in general.

Finally, I would like to dedicate this work to Marcelo. These past several years have not been easy and I truly thank Marcelo for staying by my side during my good and bad times. I would not have made it this far without him.

Contents

List of Figures

List of Tables

List of Symbols

Acronyms

ABL	Atmospheric Boundary Layer
CFD	Computational Fluid Dynamics
DNS	Direct Numerical Simulation
LES	Large Eddy Simulation
$PM_{2.5}$	Particulate matter - 2.5 micrometres or less
PM_{10}	Particulate matter - 10 micrometres or less
RANS	Reynolds averaged Navier-Stokes
SST	Shear-Stress Transport
USEPA	United States Environmental Protection Agency

Roman symbols

A, M, N	Numerical coefficients
CR	Cover rate of the surface by non-erodible particles (%)
CR_f	Final cover rate (%)
CR_i	Initial cover rate (after pavement) (%)
C_μ	Empirical constant in the $k-\varepsilon$ model
d	Distance to the nearest wall in the $k-\omega$ SST model (m)
D	Particle diameter (m)
D_E	Erodible particles diameter (m)
D_{NE}	Non-erodible particles diameter (m)
D_r	Roughness element diameter (m)
$\dot{e}(t)$	Emission rate (kg/sm)
$E_{erosion}$	Erosion depth (m)
E_f	Emitted mass (kg)
EF	Emission factor in the USEPA methodology (kg/m^2)
F_1, F_2	Blending functions of the $k-\omega$ SST model
F_{ad}	Adhesion force (N)
F_c	Interparticle cohesion force (N)
F_d	Aerodynamic drag force (N)
F_l	Aerodynamic lift force (N)
F_g	Gravitational force (N)
F_{imp}	Impact force (N)

F_R	Drag force component acting on the roughness elements (N)
F_S	Drag force component acting on the surface (N)
g	Gravity acceleration (m/s^2)
h	Stockpile height (m)
h_r	Roughness element height (m)
H	Eroded depth (m)
H_b	Building height (m)
H_{bed}	Particles bed height (m)
H_f	Final eroded depth (m)
k	Turbulent kinetic energy (m^2/s^2)
k_s	Nikuradse roughness length (m)
K	Particle size multiplier in the USEPA methodology
l_m	Prandtl mixing length (m)
L	Saltation length (m)
L_{bed}	Particles bed length (m)
m	Parameter to express the maximum shear on the surface
M_i	Mass of particles with representative diameter D_i (kg)
M_{tot}	Total mass of particles in the bed (kg)
n_i	Number of particles with representative diameter D_i
$n_{i/l}$	Number of particles per layer for each representative diameter D_i
n_r	Number of roughness elements in a rough particle bed
p	Static pressure (Pa)
P_i	Erosion potential in the USEPA methodology (kg/m^2)
P_{mod}	Modified erosion potential considering the amount of non-erodible particles (kg/m^2)
Q	Mass flow rate (kg/sm)
r	Radius of the round crest shape of a stockpile (m)
Re_r	Roughness Reynolds number
Re^*	Particle Reynolds number
Re_t^*	Particle Reynolds number at the threshold friction velocity
R_{fric}	Friction velocity ratio
R_{MIN}	Minimum value of R_{fric} in the emission model
S_{bed}	Bed surface (m^2)
S_{ij}	Strain rate tensor $(1/s)$
S_{floor}	Roughness element basal surface (m^2)
$S_{frontal}$	Roughness element frontal surface (m^2)
t	Time (s)
T	Number of perturbations in the USEPA methodology
T_B	Average temporal periodicity of coherent structures (s)
u^*	Friction velocity (m/s)
u_0^*	Friction velocity for a surface without roughness elements (non-erodible particles) (m/s)

u_{10}^{+}	Fastest wind for a period between disturbances (height of 10 m) in the USEPA methodology (m/s)
u_1, u_2	Horizontal particle velocity at take-off and at impact (m/s)
u_i'	Velocity fluctuations in i direction (m/s)
u_{MIN}^{*}	Minimum value of the friction velocity in the emission model (m/s)
u_r	Approach wind velocity (height of 10 m) in the USEPA methodology (m/s)
u_s	Surface wind velocity (25 cm from the pile) in the USEPA methodology (m/s)
$u_{t_d}^{*}$	Dynamic threshold friction velocity (m/s)
$u_{t_s}^{*}$	Static threshold friction velocity (m/s)
u_S^{*}	Friction velocity on the surface representing erodible particles (m/s)
U, V, W	Velocity components in directions x, y and z (m/s)
U_∞	Freestream air velocity (m/s)
U_f	Velocity on the focus point (m/s)
U_i	Velocity components in i direction (m/s)
V_{bed}	Volume of the particles bed (m^3)
V_{D_i}	Volume of a particle with diameter D_i (m^3)
V_i	Volume of particles with representative diameter D_i (m^3)
V_{imp}	Impact velocity of a particle (m/s)
V_{tot}	Total volume occupied by the particles of the bed (m^3)
w_1, w_2	Vertical particle velocity at take-off and at impact (m/s)
W_{bed}	Particles bed length (m)
x, y, z	Streamwise, spanwise and vertical coordinates (m)
x_i	Coordinate in i direction (m)
z_0	Aerodynamic roughness length (m)
z_0'	Saltation roughness length (m)
z_{0S}	Aerodynamic roughness length of the erodible surface (m)
z_f	Height of the focus point (m)

Greek symbols

α, β, σ_k, σ_ω	Constants in the $k-\omega$ SST model
α_1, β_1, σ_{k_1}, σ_{ω_1}	Constants in the $k-\omega$ SST model from the $k-\omega$ model
α_2, β_2, σ_{k_2}, σ_{ω_2}	Constants in the $k-\omega$ SST model from the $k-\varepsilon$ model
α_i	Mass fraction of particles with representative diameter D_i (%)
α_{NE}	Mass fraction of non-erodible particles (%)
β'	Ratio of roughness element to surface drag coefficients
β^*	Empirical coefficient of the $k-\omega$ model
γ	Surface energy which characterises the cohesion (kg/s^2)
δ	Height of the boundary layer (m)
ε	Kinetic energy dissipation (m^2/s^3)

θ	Inclination angle of a sloped surface (°)
Θ_D	Dynamic threshold shields number
Θ_S	Static threshold shields number
Θ	Shields number
κ	Von Kármán constant
λ	Roughness density
λ_x, λ_y	Average streamwise and spanwise spatial periodicities of coherent structures (m)
μ	Dynamic viscosity (Ns/m^2)
μ_t	Eddy viscosity (Ns/m^2)
ν	Kinematic viscosity (m^2/s^2)
ξ	Angle of repose of a granular material (°)
ρ	Air density (kg/m^3)
ρ_{bed}	Bulk density of the granular material (kg/m^3)
ρ_P	Particle density (kg/m^3)
σ	Ratio of roughness elements basal to frontal area
τ	Total shear stress (N/m^2)
τ_a	Airborne shear stress (N/m^2)
τ_{ij}	Stress tensor (N/m^2)
${\tau_{ij}}^t$	Reynolds turbulent stress tensor (N/m^2)
${\tau_{ij}}^v$	Viscous Stress tensor (N/m^2)
τ_p	Particle shear stress (N/m^2)
τ^t	Reynolds turbulent shear stress (N/m^2)
τ^v	Viscous shear stress (N/m^2)
τ_z	Vertical component of the shear stress (N/m^2)
τ_R	Shear stress component due to F_R (N/m^2)
τ_S	Shear stress component due to F_S (N/m^2)
τ_S'	Shear stress on the erodible surface (N/m^2)
τ_S''	Maximum shear stress on the erodible surface (N/m^2)
φ	Volume fraction
φ_i	Partial volume fraction of particles with diameter D_i
φ_{NE}	Partial volume fraction of non-erodible particles
ω	Specific turbulence dissipation rate ($1/s$)

Subscript

i,j,k	Indicial notation
min, max	Minimum and maximum values
ref	Reference value

Superscript

$'$	Fluctuations
$-$	Average value
$+$	Dimensionless values using the variables u^* and ν

Résumé étendu

L'érosion éolienne est un processus naturel caractérisé par entraînement, transport et de dépôt de particules en raison de l'action du vent. Elle peut mener à plusieurs problèmes environnementaux tels que la désertification, la dégradation des terres, la pollution atmosphérique, entre autres. L'érosion éolienne promeut des émissions de particules provenant des tas de stockage de matériaux granulaires trouvés couramment dans les yards ouverts sur des sites industriels. Les caractéristiques géométriques des tas et son orientation vers le sens d'écoulement du vent principal ont une influence forte sur la quantité de particules émises. En outre, la présence d'autres obstacles tels que des bâtiments ou des tas supplémentaires dans les zones environnantes peut également influer sur la dynamique des écoulements et par conséquent influencer les émissions globales. L'Agence Américaine pour la Protection de l'Environnement (US EPA) a proposé un modèle d'émission, d'après les données de soufflerie des tas isolés avec deux formes différentes et trois orientations des tas à la direction du vent. Il a été le modèle plus largement utilisé pour la quantification d'émissions de poussière des sources diffuses. Toutefois, les différentes configurations des formes et des compositions des tas que l'on retrouve dans des sites industriels ne sont pas couvertes par ce modèle.

La distribution de matériaux granulaires typiques disponibles en sites sidérurgiques, tels que le minerai et le charbon, sont généralement constitués d'un mélange d'une large gamme de diamètres, allant de quelques micromètres à un centimètre. Par conséquent, le mélange contient des particules plus grosses qui sont non-érodables même avec de fortes rafales de vent. Un lit ou un tas de matériaux granulaires avec un spectre granulométrique large contenant des particules érodables et non-érodables expérimente une accumulation de particules non-érodables à la surface, qui joue un rôle protecteur pour les particules érodables, en posant du pavage sur la surface et en réduisant des émissions. Les particules non-érodables créent les zones de sillage en aval qui protègent la fraction érodable de la surface. Certains modèles d'émission tiennent compte la largeur du spectre granulométrique de particules (Marticorena and Bergametti, 1995; Kok et al., 2014). Cependant, il est supposé généralement que la quantité de particules érodables est illimitée et la variation temporelle de la distribution de particules du matériau granulaire n'est pas considérée.

Par conséquent, l'objectif principal de ce travail est de proposer un modèle pour

estimer les émissions dues à l'érosion éolienne, en tenant compte l'influence du pavage causée par les particules non-érodables et d'évaluer l'impact de la présence de bâtiments et/ou plusieurs tas en yards de stockage sur l'ensemble d'émissions de particules. Par conséquent, les tâches suivantes ont été réalisées :

- Évaluation de l'influence des particules non-érodables sur la distribution des contraintes de cisaillement (vitesse de frottement) sur la surface par moyen de simulation numérique de l'écoulement sur des lits de matériaux granulaires ;
- Analyse de l'influence de pavage et des phénomènes de l'impact sur les émissions causées par l'érosion éolienne ;
- Analyse de l'influence d'une surface inclinée (tas de stockage) sur les émissions ;
- Recherche sur l'impact de la présence de bâtiments et/ou plusieurs tas sur l'érosion éolienne.

Le modèle analytique proposé a été initialement développé pour quantifier les émissions des lits de particules. Il prend en compte deux phénomènes importants au cours de l'érosion éolienne : pavages et saltations. Les effets de saltation ont été inclus en utilisant le seuil dynamique au lieu du seuil statique. Les effets du processus de pavage sont incorporés dans le modèle par la diminution de la vitesse de frottement moyenne sur la surface d'érosion que s'accumulent les particules non-érodables. La distribution de la vitesse de frottement sur la surface d'érosion d'un lit de particules a été évaluée par moyen de simulations numériques sur un domaine partiellement couvert par des éléments de rugosité. Des travaux précédents ont défini une relation mathématique entre l'évolution de la vitesse de frottement sur la surface d'érosion et la géométrie des éléments de rugosité (Turpin et al., 2010; Furieri et al., 2013a). Néanmoins, la formulation n'était valide que à des taux de couverture limitée de particules non-érodables ($< 12\%$). Des simulations numériques supplémentaires ont été effectuées dans ce travail pour étendre la formulation afin d'y inclure d'autres cas rencontrés dans des situations réelles (avec plus grandes quantités de particules non-érodables). Il a été révélé que la forme mathématique de la relation proposée précédemment pour la vitesse de frottement en fonction des paramètres géométriques des éléments de rugosité (diamètre, hauteur émergente et taux de couverture) est toujours valable, mais les constantes numériques devaient être modifiées afin de couvrir le large éventail de cas rencontrés dans la nature. Les résultats numériques ont permis la modélisation du processus de pavage puisque les particules non-érodables accumulent sur la surface du lit de particules.

Le modèle d'émission proposé décrit la relation entre la valeur minimale de la vitesse de frottement (au cours de laquelle les émissions cessent), prenant avantage des résultats numériques, et la profondeur finale érodée du lit, qui à son tour,

fournit la masse émise. Un des avantages du modèle est qu'il est une expression algébrique simple qui exige l'effort de calcul faible. Le modèle prédit avec succès la diminution des émissions avec la proportion de l'augmentation de particules non-érodables. En outre, le taux de couverture des particules non-érodables après le phénomène du pavage a été quantifié.

Des expériences en soufflerie ont été menées afin de mieux comprendre le phénomène du pavage et d'estimer les émissions d'un lit de particules. Les résultats expérimentaux ont aussi servi à valider la modélisation, y compris la masse globale émise et les caractéristiques finales de la surface du lit. Une granulométrie bimodale de sable avec des particules érodables et non-érodables pour les vitesses testées a été utilisée. Trois types de mesures ont été effectuées : (i) pesée successive de la masse émise, (ii) profondeur d'érosion du lit (iii) taux de couverture finale des particules non-érodables en utilisant l'analyse numérique des photos du lit de sable après expériences. Un bon accord a été trouvé entre les résultats expérimentaux et modélisées pour les émissions et la profondeur du lit érodé.

Le modèle d'émission a été étendu pour décrire l'érosion des tas de stockage. Dans ce cas, l'érodabilité des particules est plus complexe car la vitesse de frottement et les conditions de seuil ne sont pas spatialement homogènes. La vitesse de frottement n'est pas constante sur la surface du tas une fois que le tas se comporte comme un obstacle et modifie l'écoulement de vent. Les conditions de seuil d'émission ne sont pas uniformes sur toute la surface du tas une fois que la pente crée des contributions distinctes des forces qui agissent sur les particules. La vitesse de frottement du seuil locale sur la pile dépend de la pente et de la direction de la contrainte de cisaillement basale locale. Par conséquent, la distribution de cisaillement sur le tas est requise comme données d'entrée pour le modèle d'émissions pour les tas de stockage.

L'idée du modèle d'émission de tas est de diviser la surface du tas. Tout d'abord, il se subdivise en des isosurfaces où les critères de seuil sont constants. Une fois que le seuil est défini pour chaque partie du tas, les domaines avec le même dégrée d'exposition au vent sont regroupés. Ainsi, chacun de ces domaines est séparé dans des isosurfaces avec vitesse de frottement constante. Après les deux subdivisions, chaque isosurface dans lequel les conditions de seuil et la vitesse de frottement sont constantes est considérée comme une source différente, où le modèle d'émission peut être appliqué.

Des expérimentations en soufflerie ont été également effectué afin d'estimer les émissions d'un tas de sable contenant une distribution granulométrique bimodale. La modélisation et les résultats expérimentaux ont été comparés pour la configuration d'un tas de stockage isolé (oriented 60 and 90° à la direction de l'écoulement principal) et un bon accord a été trouvé entre l'estimation et la masse émise mesuré.

L'impact de la présence d'un obstacle sur l'émission de particules a également été évalué une fois que les sites industriels comprennent habituellement plusieurs tas de matériaux granulaires et bâtiments à proximité. Des expérimentations de soufflerie et des simulations numériques ont été réalisées pour plusieurs configurations, en évaluant les effets de : (i) orientation du flux de vent principal, (ii)

vitesse d'écoulement de vent, (iii) l'écart entre les obstacles et (iv) la quantité de particules non-érodables.

Dans l'étude expérimentale, les particules dans les tas avaient une granulométrie bimodale, composé de sable qui a été érodable (blanc) et non-érodable (noir) dans la gamme de vitesse étudié. Les couleurs contrastantes ont permis la visualisation de l'accumulation de sable non-érodable. La distribution du cisaillement et des lignes de flux prévues par les simulations numériques a été associé aux visualisations pariétales de l'érosion. En plus, la masse émise a été quantifiée expérimentalement comme la différence entre les poids des tas initiaux et finaux. Il a été constaté que les interférences de l'écoulement entre les deux tas augmentent les émissions et le montant global peut être plus de deux fois les émissions d'un tas isolé. Le tas en aval est beaucoup plus affecté que le tas en amont. Les particules du tas en amont incident sur le tas en aval, ce qui promeut des éjections en plus. En outre, il a été constaté que les changements de l'écoulement en raison de la présence du bâtiment augmentent les émissions, en particulier de la partie en amont du tas. Par conséquent, toutes les perturbations du vent ont un impact significatif et doivent être reprises dans l'estimation des émissions de poussière et modélisation.

Cette étude est une étape importante vers une évaluation plus précise des émissions de l'érosion éolienne des lits et tas de stockage de matériaux granulaires. Cependant, des recherches sont encore nécessaires pour étudier le processus de pavage dans des situations plus générales pour des applications pour des conditions réelles telles que celles trouvées sur les sites industriels. Il est recommandé d'effectuer des analyses de similarité entre le modèle de soufflerie et un tas réel afin de représenter fidèlement le comportement du champ. En outre, il y a des limites dans le modèle proposé et de plus amples recherches sont également nécessaires. Du travail en plus pour améliorer la modélisation en incluant un critère de suspension de particules afin d'enquêter sur le comportement des particules après l'entraînement et déterminer s'ils restent en suspension ou sont éliminés par les dépôts. L'influence des autres paramètres, tels que les conditions de stabilité atmosphérique, la température et l'humidité peut aussi être importante.

La thèse est organisée en 5 chapitres. Chapitre 1 présente les informations de fond sur l'écoulement atmosphérique et l'érosion éolienne et une revue de la littérature scientifique pertinente. Chapitre 2 présente les résultats obtenus par l'étude expérimentale de l'érosion éolienne des lits, décrivant le développement théorique du modèle d'émissions pour les surfaces horizontales qui utilise les résultats numériques de la partition de la contrainte de cisaillement sur un lit contenant des particules non-érodables, et présente la validation du modèle. Chapitre 3 présente le modèle étendu d'émission pour les tas de stockage et discute l'impact sur les émissions des obstacles supplémentaires en sites ouverts, comme un autre tas ou d'un bâtiment, à l'aide de simulations numériques pour obtenir le champ de contraintes de cisaillement et des données expérimentales obtenues en soufflerie pour valider le modèle d'émission. Enfin, les chapitres 4 et 5 présentent les conclusions de cette thèse et les recommandations pour les travaux futurs.

Resumo

O processo de erosão eólica pode levar a várias consequências ambientais: desertificação, degradação da terra, poluição do ar, etc. Esta última está relacionada com as emissões de partículas provenientes de materiais granulares comumente encontrados em indústrias, como minério e carvão. A distribuição granulométrica destes materiais normalmente consiste em uma mistura com uma ampla gama de tamanhos, incluindo partículas maiores que não são erodíveis mesmo com fortes rajadas de vento. As partículas não erodíveis desempenham um papel protetor para as partículas erodíveis, pavimentando a superfície e reduzindo as emissões. O objetivo principal desta tese é estimar com maior acurácia as emissões devidas à erosão eólica considerando a influência da pavimentação causada pelas partículas não-erodíveis.

Um modelo analítico foi proposto para quantificar as emissões de leitos de partículas e pilhas com ampla distribuição granulométrica. Os efeitos do processo da pavimentação são incorporados no modelo por meio da diminuição da velocidade de fricção média na superfície erodível à medida que as partículas não-erodíveis se acumulam. Trabalhos anteriores definiram uma relação matemática entre a evolução da velocidade de fricção na superfície erodível e a geometria dos elementos rugosos. No entanto, a formulação é válida apenas para limitadas taxas de cobertura de partículas não-erodíveis ($< 12\%$). Simulações numéricas foram realizadas neste trabalho para estender a formulação de modo a incluir outros casos encontrados em situações reais (com maiores quantidades de partículas não-erodíveis). O modelo de emissão proposto descreve a relação entre o valor mínimo da velocidade de fricção (para qual as emissões cessam), utilizando os resultados numéricos, e a profundidade final erodida do leito, que, por sua vez, fornece a massa emitida.

Experimentos em túnel de vento foram realizados para melhor compreender o fenômeno da pavimentação e estimar as emissões de um leito de partículas contendo uma distribuição granulométrica bimodal. Os resultados experimentais foram também utilizados para validar a modelagem, incluindo a massa global emitida e as características finais da superfície do leito. Uma boa concordância foi encontrada entre os resultados experimentais e modelados para as emissões globais e a profundidade erodida do leito.

O modelo de erosão foi estendido para aplicação em pilhas de estocagem. Neste caso, a erodibilidade das partículas é mais complexa, uma vez que a velocidade

de fricção e as condições de limiar não são espacialmente homogêneas. A ideia do modelo é subdividir a pilha em isosuperfícies em que as condições de limiar e a velocidade de fricção são constantes e, em seguida, tratar cada uma dessas áreas como uma fonte diferente onde o modelo de emissão pode ser aplicado. Foram realizados ensaios experimentais em túnel de vento para estimar as emissões de uma pilha de areia contendo uma distribuição de tamanho bimodal. Os resultados experimentais e modelados foram comparados para a configuração de uma pilha isolada (orientada 60 e 90° em relação a direção do escoamento) e uma boa concordância foi encontrada entre a massa estimada e a emitida.

O impacto na emissão da presença de um edifício e de uma pilha de estocagem sucessiva também foi avaliado. Experimentos em túnel de vento e simulações numéricas foram realizados para várias configurações avaliando os efeitos de: (i) orientação do vento, (ii) velocidade do vento, (iii) espaçamento entre os obstáculos e (iv) quantidade de partículas não erodíveis. Verificou-se que as interferências do escoamento entre os obstáculos aumentam as emissões. Portanto, todas as perturbações no escoamento têm um impacto significativo e devem ser contabilizadas na estimativa e modelagem de emissões de partículas.

Abstract

Wind erosion process can lead to several environmental consequences: desertification, land degradation, air pollution, etc. This last one is related to particulate matter emissions from granular materials commonly found on industrial sites, such as ore and coal. The particle size distribution of these granular materials usually consist of a mixture of a wide range of diameters, which include larger particles that are non-erodible even with strong gusts of wind. The non-erodible particles play a protective role for erodible particles, paving the surface and reducing emissions. The main objective of this thesis is to estimate more accurately emissions due to wind erosion considering the influence of the pavement caused by non-erodible particles.

An analytical model was proposed to quantify emissions from particle beds and stockpiles with a wide size distribution. The effects of pavement process are incorporated in the model through the decrease of the mean friction velocity on the erodible surface as the non-erodible particles accumulate. Previous works have defined a mathematical relation between the evolution of the friction velocity over the erodible surface and the geometry of the roughness elements. Nonetheless, the formulation was only valid to limited cover rates of non-erodible particles ($< 12\%$). Numerical simulations were carried out in this work to extend the formulation in order to include other cases encountered in real situations (with larger amounts of non-erodible particles). The proposed emission model describes the relationship between the minimum value of friction velocity (at which emissions cease), taking advantage of the numerical findings, and the final eroded depth of the bed, which in turn, provides the emitted mass.

Wind tunnel experiments were carried out in order to better understand the pavement phenomenon and estimate emissions from a bed of particles containing a bimodal size distribution. The experimental results were also used to validate the modelling, including the global emitted mass and the final characteristics of the bed surface. A good agreement was found between experimental and modelled results for the global emissions and the bed eroded depth.

The erosion model was extended for application in stockpiles. In this case, the erodibility of the particles is more complex as the friction velocity and the threshold conditions are not spatially homogeneous. The idea of the model was to subdivide the pile in isosurfaces in which the threshold conditions and the friction velocity are constant and then treat each one of these areas as a different source where

the emission model can be applied. Wind tunnel experiments were carried out in order to estimate emissions from a sand pile containing a bimodal size distribution. The modelled and the experimental results were compared for the configuration of an isolated stockpile (oriented 60 and 90° to the main flow direction) and a good agreement was found between the estimated and the measured emitted mass.

The impact of the presence of a building and a successive parallel stockpiles on the overall particles emission was also evaluated. Wind tunnel experiments and numerical simulations were carried out for several configurations evaluating the effects of: (i) main wind flow orientation, (ii) wind flow velocity, (iii) gap between the obstacle and (iv) amount of non-erodible particles. It was found that the flow interferences between the obstacles increase emissions. Therefore, all wind perturbations have a significant impact and have to be accounted in dust emission estimation and modelling.

Introduction

Wind erosion is a natural process characterised by particle entrainment, transport and deposition due to the action of wind. The understanding of the phenomenon is important in several research fields such as land degradation in agricultural areas, deserts expansion, dunes morphology and dynamics, dust storms, air pollution, etc. Wind erosion can lead to serious environmental impacts once the emissions can extend for large distance from the source.

Particulate air pollutants have diverse chemical compositions and cover a wide range of sizes, from 0.001 nm to 100 μm. Although the particles larger than 10 μm have a shorter atmospheric lifetime and settle closer to the sources of emission, they can cause annoyance related to dirtiness, eye irritation, cough and allergic reaction. The long-range transport of the smallest particles, such as PM_{10} (< 10 μm), $PM_{2.5}$ (< 2.5 μm) and ultrafine particle fractions (< 0.1 μm), can reach atmospheric lifetimes of days, weeks, or even years. These particles are responsible for a variety of serious harmful effects on health, especially related to cardiovascular and respiratory diseases (WHO, 2006).

Granular materials used in industrial processes are commonly stored as stockpiles in open air yards (Figure 1). Dust emissions due to wind erosion of these stockpiles may have a significant contribution to air quality degradation. Despite of the importance of quantifying these fugitive emissions, the accuracy and practicality of the measurement are challenges once the emissions are not confined.

The geometric characteristics of the pile and its orientation to the main wind flow direction have strong influence on emissions. In addition, the presence of other obstacles such as buildings or additional piles on the surrounding can also affect the flow dynamics, and consequently influence overall emissions. The United States Environmental Protection Agency (USEPA) proposed an emission model, based on wind tunnel data of isolated piles with two different shapes and three wind orientations. It has been the most widely used model for dust emissions quantification of diffuse sources. However, the various configurations of pile shapes and compositions that can be found on industrial sites are not covered by the USEPA (2006) model.

Bagnold, in 1941, was a pioneer describing the physics of wind erosion and developed a theory based on experimental tests carried out in a wind tunnel and on the field. He analysed the behaviour of particles exposed to the atmospheric flow and determined the threshold conditions for emissions. The erosion mechanisms

Figure 1: Storage yard of granular material from Arcelor Mittal Tubarão facility, located in Espírito Santo, Brazil

depend on interactions among stockpile surface, atmospheric flow and airborne particles. Particles lifted from the surface and transported by wind affects the wind velocity profile due to momentum transfer from the flow to the particles.

Three main modes of particle transportation are defined: (i) Suspension, if the grains are small enough ($\lesssim$ 20 μm) such that aerodynamic forces are dominant and the particles are completely carried out by the flow, (ii) Creep, if the grains are large enough ($\gtrsim$ 500 μm) such that the gravitational force is dominant and they roll along the surface, and (iii) Saltation, if the grains size is sufficiently small such that they are entrained in the flow, but their weight is high enough such that they fall back onto the bed and rebound, entering in motion again. Saltation plays a central role in aeolian processes since the impact of the saltating particles on the surface usually initiates the other forms of transport.

Following the work of Bagnold (1941), several studies have been devoted to better understand the physical processes and the transport mechanisms associated with wind erosion (Durán et al., 2011; Kok et al., 2012; Valance et al., 2015). Nonetheless, some aspects still need to be investigated. For instance, large part of the work found in the literature focuses on the transport of sand with nearly uniform granulometry. However, several applications deal with granular materials with a non-uniform particle size distribution, which considerably influences the erosion process.

Figure 2 shows the particle size distribution of typical granular materials, such

as ore and coal, found in steelwork facilities. These materials consist of a mixture of different diameters, ranging from few micrometres to a centimetre. The characteristics of the particles (size and density) influence their erodibility and trajectories. Coarser particles may be non-erodible even with strong gusts of wind.

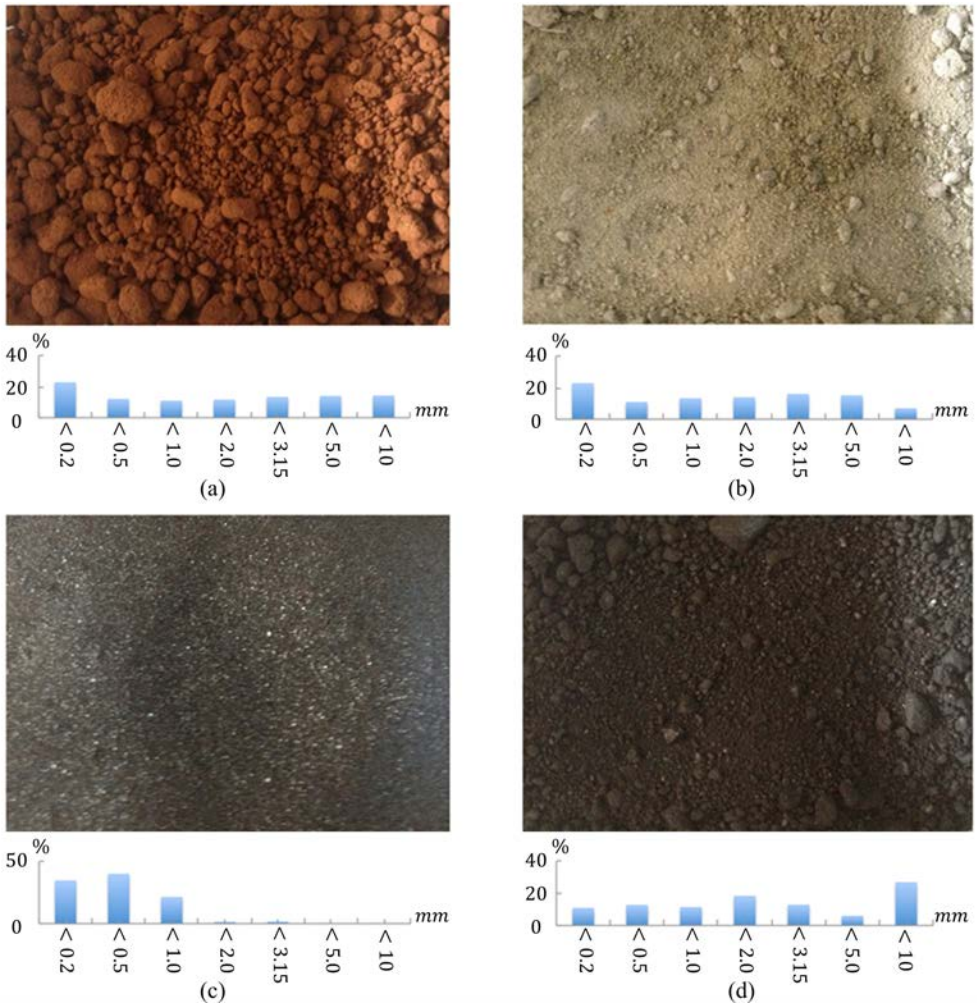

Figure 2: Typical granular materials used in steel industries: Minerals (a) Ore 1, (b) Ore 2, (c) Ore 3, and (d) Coal

A bed or pile of granular materials with wide size distribution containing erodible and non-erodible particles experiences an accumulation of non-erodible particles on the surface, which plays a protective role for erodible particles emission. The non-erodible particles create wake zones of reduced wind shear stress that shelter the erodible fraction of the surface (Gillette and Stockton, 1989; Iversen et al., 1991; Raupach et al., 1993).

Some emission models account for a wide range of particle size distribution (Marticorena and Bergametti, 1995; Kok et al., 2014). However, it is usually assumed that the amount of erodible particles is unlimited and the time variation of

granular material size distribution is not considered. Experimental results showed that the presence of non-erodible particles promotes a temporal decrease of the emitted mass flux and erosion ceases even before all erodible particles on the surface are emitted (Lyles et al., 1976; Descamps, 2004; Furieri et al., 2013b). This phenomenon is known as pavement.

Descamps et al. (2005) developed a stochastic model to quantify the temporal evolution of the mass flux in a bed of particles with a wide range of size distribution exposed to a turbulent flow. The authors modelled the pavement considering a temporal decrease on the aerodynamic lift forces acting on the particle. However, Descamps et al. (2005) assumed that erosion ceases when the bed is completely overlaid by non-erodible particles. This assumption disagrees with experimental observations. Thus, an alternative approach to model emission including the pavement phenomenon is needed.

The present work proposes a model to quantify emissions due to erosion of granular materials with a wide range of particle sizes, which is based on the shear stress partition between the non-erodible roughness elements and the erodible fraction of the surface. As the concentration of non-erodible particles on the surface increases, the shear stress in the erodible surface decreases until it is no longer significant to cause emissions. The proposed model can be applied to beds or piles of particles.

The thesis is organised in 5 chapters. Following this introduction, the main objectives of the thesis are stated. Chapter 1 presents the background information about atmospheric flows and wind erosion, and a review of the relevant scientific literature. Chapter 2 presents the results obtained from an experimental study that enables a better comprehension of wind erosion of beds, describes the theoretical development of the emission model for horizontal beds which uses numerical results of the shear stress partition on a bed containing non-erodible particles, and presents the model validation. Chapter 3 discusses the impact on emissions of additional obstacles in open yards, such as another stockpile or a building, using numerical simulations to obtain the shear stress field and experimental data obtained in wind tunnel to validate the emission model. Finally, Chapters 4 and 5 present the conclusions of this thesis and the recommendations for future works.

Objectives

The main objective of this work is to propose a model to estimate emissions due to wind erosion including the influence of saltation and the pavement caused by non-erodible particles, and to evaluate the impact of the presence of buildings and/or multiple piles in storage yards on the overall particles emission. In particular, the work has the following aims:

- To assess the influence of non-erodible particles on shear stress distribution (friction velocity) over the surface by means of numerical simulation of the flow over granular material beds;
- To analyse the influence of pavement and impact phenomena on emission caused by wind erosion;
- To analyse the influence of an inclined surface (stockpiles) on emission due to wind erosion;
- To investigate the impact of the presence of buildings and/or multiple piles on wind erosion.

Chapter 1

Aeolian Erosion Background

This chapter provides a review of the past and recent studies on aeolian erosion and gives important background information on the theory. The chapter starts with an overview of the atmospheric boundary layer flows in Section 1, covering the boundary layer structure, momentum transfer from the atmosphere to the surface and wind velocity profiles. Section 2 focuses on the mathematical representation and turbulence modelling of atmospheric turbulent flows. Section 3 presents the basic aspects of wind erosion phenomenon and discusses the modelling of steady state saltation. Section 4 deals with a non-equilibrium regime and the influence of a wide particle size distribution on emissions is considered. Lastly, Section 5 discusses how an obstacle disturbs the flow and its influence on emissions from stockpiles.

1.1 Atmospheric boundary layer

Atmospheric boundary layer (ABL) is the part of the atmosphere under the influence of the exchanges of energy, momentum and mass between air and Earth's surface on time periods of hours. ABL flows are predominantly turbulent, composed by eddies of a wide range of length and time scales that can range from millimetres up to few kilometres and from a second to several minutes, respectively.

The turbulent intensity of the flow is indicated by a turbulent kinetic energy associated to the eddies. Energy is extracted from the mean flow to form the largest eddies and transferred down to the smaller ones through a cascade process. At the smallest scales (Kolmogorov's scales) where viscous effects dominate, this energy is dissipated by molecular viscosity.

Turbulence is generated by wind shear and buoyancy. Wind shear invariably leads to a positive contribution on turbulent kinetic energy. On the other hand, buoyancy can either generate or suppress turbulence. Buoyancy occurs due to heat transfer from/to the surface to/from the air if the temperatures of the two media

are different. Heat flux is due to solar radiation during the day (positive flux) or to surface cooling at night (negative flux). If there is a positive heat flux, buoyancy pushes upwards the warmer air close to the surface producing turbulent kinetic energy and consequently generating turbulence, which characterises a convective boundary layer. On the other hand, if there is a negative heat flux, the air near the wall remains thermally stable, which characterises a stable boundary layer. If the heat flux is zero, buoyancy can be neglected and the boundary layer is said to be neutral.

Particles emissions due to wind erosion take place in the lower portion of the ABL (about 10% of its height), known as surface layer, in which physical quantities such as wind velocity and temperature vary rapidly with height. In the present study, the influence of thermal stratification is not addressed, that is, the atmosphere is considered neutral.

Figure 1.1 shows, for a classical turbulent boundary layer, the variations with height (z) of the total shear stress (τ) and its viscous and turbulent components (τ^v and τ^t, respectively). The total shear stress τ, as a sum of τ^v andτ^t, remains approximately constant with height in the surface layer. According to the distance from the surface and the relative importance of τ^t and τ^v, three different layers are identified: (i) Viscous layer is the thin near wall region within turbulence is weak and the flow is dominated by viscosity, that is, turbulent stress is negligible compared to viscous stress ($\tau \approx \tau^v$), (ii) Transitional layer, within viscous and turbulent stresses are of similar magnitude and (iii) Logarithmic layer, within turbulence is strong and viscosity has little effect ($\tau \approx \tau^t$).

A characteristic scale of velocity representing the moment flux at the surface by the wind shear is the friction velocity:

$$u^* = \sqrt{\frac{\tau}{\rho}}\,, \tag{1.1}$$

where ρ is the air density.

The magnitude of the dimensionless height $z^+ = z\frac{u^*}{\nu}$ (where ν is the kinematic viscosity of air) determines the relative importance of viscous and turbulent processes. The upper limit of the viscous layer is about $z^+ = 5$ and the logarithmic layer extend from $z^+ = 30$ to about $z^+ = 500$ (Pope, 2000).

A common way to model τ^t, proposed by Boussinesq, uses the analogy with the Newton's law of viscosity, replacing the molecular viscosity of the fluid μ by an eddy viscosity μ_t. Using the fact that the mean vertical velocity is near zero throughout the surface layer and, with a coordinate system in which the x-axis is aligned with the mean wind flow direction U and assuming horizontal homogeneity, the downward momentum flux through both viscous and turbulent mixing can be modelled as:

$$\tau = \tau^v + \tau^t = (\mu + \mu_t)\frac{dU}{dz}\,. \tag{1.2}$$

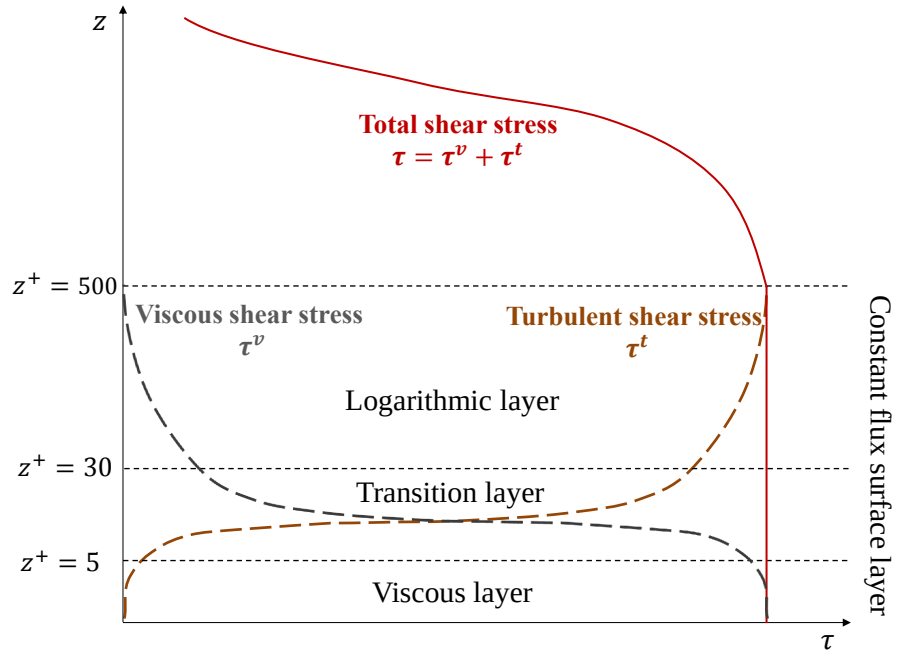

Figure 1.1: Profiles of the total stress τ, Reynolds shear stress τ^t, and viscous shear stress τ^v

For a smooth surface, the velocity profile in a neutral atmospheric surface layer presents three typical regions, according to the layers described in Figure 1.1.

In the first region, the viscous layer, $\tau \approx \tau^v$. Thus Equation 1.2 can be rewritten using Equation 1.1 as:

$$\rho u^{*2} = \mu \frac{dU}{dz} \,. \tag{1.3}$$

An integration of Equation 1.3 over z from $z = 0$ to an arbitrary height z in the viscous layer yields a linear law with the height for wind velocity (Equation 1.4).

$$U(z) = \frac{\rho u^{*2}}{\mu} z \,. \tag{1.4}$$

In the second region, there is a transition between the linear to the logarithmic profile.

In the third region, the logarithmic layer, $\tau \approx \tau^t$, and Equation 1.2 becomes:

$$\rho u^{*2} = \mu_t \frac{dU}{dz} \,. \tag{1.5}$$

Using the mixing length theory of Prandtl, an approximation to the turbulent viscosity is given by:

$$\mu_t = \rho u^* l_m \,, \tag{1.6}$$

where l_m is the mixing length, the typical size of the turbulent eddies. In the surface layer l_m is limited by the distance from the surface and can be expressed as $l_m = \kappa z$, where $\kappa \approx 0.4$ is the von Kármán constant. Therefore, Equation 1.5 can be rewritten as:

$$\frac{dU}{dz} = \frac{u^*}{\kappa z} \,. \tag{1.7}$$

Equation 1.7 is valid if z is greater than or equal to a positive value z_0, known as the aerodynamic roughness length, which represents the capacity of the surface in absorbing momentum. Therefore, an integration over z from $z = z_0$ to an arbitrary z provides the logarithmic profile:

$$U(z) = \frac{u^*}{\kappa} \ln\left(\frac{z}{z_0}\right) \,. \tag{1.8}$$

The aerodynamic roughness length z_0 generally depends on the surface characteristics such as the geometric features of the roughness elements and their spatial arrangement. A useful parameter to determine whether a surface is considered rough or smooth is the roughness Reynolds number Re_r, defined by:

$$Re_r = \frac{u^* k_s}{\nu} \,, \tag{1.9}$$

where k_s is a characteristic height of the roughness elements (Nikuradse roughness).

The pioneer experimental study of Nikuradse (1933) established a criterion that classifies the flow in three different regimes: hydraulically smooth regime if $Re_r < 5$, fully rough regime if $Re_r > 70$ and transitional regime for intermediate values of Re_r.

Figure 1.2 shows an scheme of the wind velocity profile in the surface layer for a smooth and a rough surface. For a smooth surface, the logarithmic profile matches the linear profile at the upper part of the viscous layer. If the surface is rough, a roughness layer is formed close to the wall. In this case, the relationship between z_0 and the physical size of the roughness elements is not simple, but depends on the interferences of the turbulent wakes generated by the roughness elements.

The logarithmic profile (Equation 1.8) can be rewritten as:

$$U(z) = \frac{u^*}{\kappa} \ln\left(\frac{z}{k_s}\right) + B \,, \tag{1.10}$$

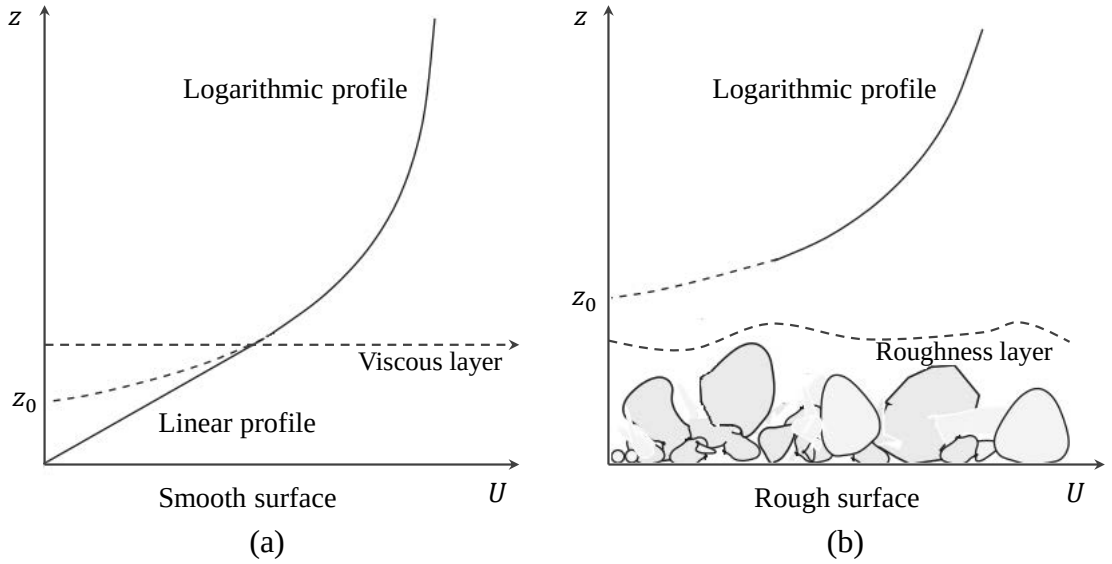

Figure 1.2: Mean velocity profiles in the surface layer over (a) a smooth surface and (b) a rough surface, from Shao (2008)

where B is the roughness function (Schlichting, 1979):

$$\begin{cases} B = 5.5 + \frac{1}{\kappa} \ln \frac{k_s u^*}{\nu} & \text{for hydraulically smooth flow}\,, \\ B = 8.5 & \text{for fully rough flow}\,. \end{cases} \tag{1.11}$$

Using Equations 1.8 and 1.10 yields:

$$z_0 = \frac{k_s}{e^{B\kappa}}\,. \tag{1.12}$$

In a fully rough regime, z_0 is related to the Nikuradse roughness k_s:

$$z_0 \approx \frac{k_s}{30}\,. \tag{1.13}$$

Therefore, if k_s is taken to be the grain size D, $z_0 \approx \frac{D}{30}$.

On the other hand, in a smooth flow, z_0 is independent of the roughness element geometry and is determined only by the flow characteristics:

$$z_0 \approx \frac{\nu}{9u^*}\,. \tag{1.14}$$

The presence of sediment transport also influence the aerodynamic roughness length z_0 due to the saltation layer above the surface. More details are discussed in Section 1.3.3.1.

1.2 Mathematical modelling of turbulent flows

The atmospheric fluid flow is governed by the transport equations which are based on physical principles of conservation of mass, momentum and energy. In the present work it is assumed that the flow is incompressible since the pressure variation observed is not large enough to produce density variations. Then, the continuity and momentum equations are decoupled from the energy equation and are solved separately. In addition, it is considered neutral atmospheric conditions. Therefore, the temperature vertical profile is adiabatic and energy equation does not need to be solved as potential temperature is constant. Under these assumptions, the Continuity and the Momentum equations for Newtonian fluids can be written in tensor notation (where repeated indices imply summation) as:

Continuity equation

$$\frac{\partial U_i}{\partial x_i} = 0 \,, \tag{1.15}$$

Momentum equation

$$\frac{\partial(\rho U_i)}{\partial t} + \frac{\partial(\rho U_i U_j)}{\partial x_j} = \frac{\partial \tau_{ij}}{\partial x_j} - \frac{\partial p}{\partial x_i} \,, \tag{1.16}$$

where t is time, x_i and U_i are the cartesian coordinates and the velocity components in the i-direction, respectively, p is the static pressure and τ_{ij} is the stress tensor, determined by Newton's law of viscosity (Equation 1.17).

$$\tau_{ij} = 2\mu S_{ij} \,, \tag{1.17}$$

where S_{ij} is the strain rate tensor, given by:

$$S_{ij} = \frac{1}{2}\left(\frac{\partial U_i}{\partial x_j} + \frac{\partial U_j}{\partial x_i}\right) \,. \tag{1.18}$$

The terms in the left side of the momentum equation represent the acceleration (unsteady and convective accelerations) and the terms in the right side represent

the summation of forces acting on a fluid element, which are the tangential and the normal forces as shear and pressure, respectively.

In order to numerically solve the turbulent atmospheric flow, the governing equations and its boundary conditions must be discretized in time and space. Depending on the grid resolution, there is a classification of the solution methodology: Direct Numerical Simulation (DNS), Large Eddy Simulation (LES) and Reynolds averaged Navier-Stokes (RANS). DNS solve all turbulent scales of the flow, hence it requires the grid spacing to be smaller than the Kolmogorov scales size. There are no approximations or simplifications by turbulence modelling and the errors are related only to the numerical method used. However, the high computational requirements still limit the practical implementation of DNS to relatively simple flows. Flows with complex geometry and high values of Reynolds number require a mathematical modelling to account for turbulence effects. LES models solve the largest scales, and model the smallest ones. Once the large scales are the main responsible for the transport, LES seems to be a good alternative to DNS. Nonetheless, the computational resources also impose a limitation since a transient solution is necessary. Reynolds averaged Navier-Stokes (RANS) models are frequently used to describe the effects of turbulence due to their low computational demands compared to DNS and LES as only the average values are resolved and all scales of turbulence are modelled. The next section presents the statistical approach of RANS modelling and a brief description of turbulence modelling.

1.2.1 Reynolds Averaged Navier-Stokes (RANS)

Osborne Reynolds proposed that the instantaneous values of the flow variables, seen as a stochastic process, can be written as a sum of the variable mean value ($\overline{\phi}$) and its fluctuating component (ϕ') (see Figure 1.3).

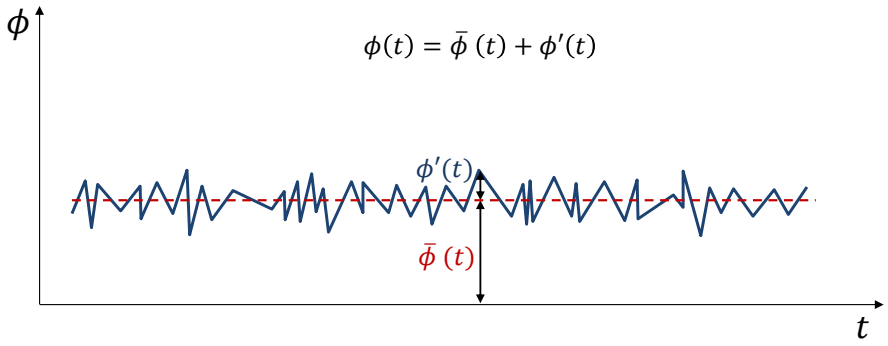

Figure 1.3: Schematic representation of the random variation of a scalar property of the flow, adapted from Santos (2000)

For instance, the instantaneous velocity in the i-direction is decomposed as:

$$U_i = \overline{U}_i + u_i' \,. \tag{1.19}$$

The decomposed variables are introduced in the conservation equations of mass and momentum (Equations 1.15 and 1.16) and averaged over a time interval taken large enough to exceed the time scales of the largest eddies. Assuming that the mean flow is steady, the Reynolds governing equations can be written as:

Continuity equation

$$\frac{\partial \overline{U}_i}{\partial x_i} = 0 \,, \tag{1.20}$$

Momentum equation

$$\frac{\partial(\rho \overline{U}_i \overline{U}_j)}{\partial x_j} = \frac{\partial}{\partial x_j}({\tau_{ij}}^v + {\tau_{ij}}^t) - \frac{\partial \overline{p}}{\partial x_i} \,, \tag{1.21}$$

where ${\tau_{ij}}^v$ is the viscous stress tensor:

$${\tau_{ij}}^v = 2\mu \overline{S}_{ij} \,, \qquad \text{with} \qquad \overline{S}_{ij} = \frac{1}{2}\left(\frac{\partial \overline{U}_i}{\partial x_j} + \frac{\partial \overline{U}_j}{\partial x_i}\right) \,, \tag{1.22}$$

and ${\tau_{ij}}^t$ is the Reynolds stress tensor:

$${\tau_{ij}}^t = -\rho \overline{u_i' u_j'} \,. \tag{1.23}$$

Reynolds-averaged Navier-Stokes equations (Equations 1.20 and 1.21) have the same general form of Equations 1.15 and 1.16, with the variables now representing mean values. However, an additional term appears in the Momentum equation, namely, the cross correlation of the fluctuations velocities $\rho \overline{u_i' u_j'}$, which represent the effects of turbulence. Therefore, there are more unknowns than equations and it is necessary to develop turbulence models with new hypotheses to estimate ${\tau_{ij}}^t$ and close the system of equations.

1.2.2 Turbulence modelling

A common way to model ${\tau_{ij}}^t$ is using the analogy with the Newtons law of viscosity, proposed by Boussinesq, in which the Reynolds stresses are expressed in terms of the mean strain rate $\overline{S}_{ij}$ similarly to viscous stress, replacing the molecular viscosity by an eddy viscosity μ_t:

$${\tau_{ij}}^t = 2\mu_t \overline{S}_{ij} \,. \tag{1.24}$$

The eddy viscosity μ_t carries all information regarding the turbulent fluctuation of the flow. The turbulence eddy viscosity models can be categorised according to the number of additional equations to be solved as: (i) Zero-differential equation, (ii) One-differential equation, and (iii) Two-differential equation.

Zero-differential equation models solve only algebraic equations for the turbulence quantities. This class of models are characterised by simplicity to implement but produces unreliable results in more complex cases such as separated flows. Nowadays, zero-equation models are used rarely and only for getting an initial prediction of the flow field (Argyropoulos and Markatos, 2015).

One-differential equation models use a differential equation to describe the transport of the turbulent kinetic energy k, given by $k = 1/2(\overline{u_1'^2} + \overline{u_2'^2} + \overline{u_3'^2})$. Nonetheless, to close the system there is still need to prescribe a turbulent length scale l, which is usually based on empirical data and can be virtually impossible to obtain in complex flows. In spite of the improvement as compared with the zero-differential equation model, there are still drawbacks related to the generality of the algebraic relations describing the length scales, which is strong dependent on the problem considered (Alfonsi, 2009).

Two-differential equation models include two additional equations to describe the turbulence quantities, in which one of them is usually a equation for k. The second equation is a transport conservation equation of dissipation. The $k-\varepsilon$ model is a popular two-differential equation model that additionally solves an equation for the turbulent dissipation rate (ε). The key point is given by the Kolmogorov theorem: the equation $\varepsilon \propto \frac{k^{3/2}}{l}$ shows that if k and ε are known, the length scale, which is the main problem for turbulence modelling, is simply defined. The eddy viscosity is estimated as a function of the k and ε values:

$$\mu_t = \rho C_\mu \frac{k^2}{\varepsilon} \,, \tag{1.25}$$

where C_μ is an empirical constant.

$k-\varepsilon$ model usually requires extra terms in the equations in order to account for the damping of turbulence which occurs close to walls and ensure proper limiting behaviour of k and ε. In spite of a good performance in some engineering applications and the relatively low computational cost, the $k-\varepsilon$ models may present low accuracy for complex flows with an adverse pressure gradient (Blazek, 2015).

The $k-\omega$ model is an alternative to $k-\varepsilon$, in which the additional differential equation introduced is for ω, the specific turbulent dissipation rate, defined in terms of k and ε by:

$$\omega = \frac{\varepsilon}{\beta^* k} \,, \tag{1.26}$$

where $\beta^* = 0.09$ is an empirical coefficient.

The eddy viscosity is determined based on k and ω values:

$$\mu_t = \rho \frac{k}{\omega} \,. \tag{1.27}$$

The $k-\omega$ is more accurate than $k-\varepsilon$ in the near wall layers giving better predictions for boundary layers with adverse pressure gradient (Yu and Righetto, 2001; Argyropoulos and Markatos, 2015). However, $k-\omega$ model has as disadvantage the strong sensitivity of the equations to the values of ω in the freestream outside the boundary layer (Menter, 1992). Menter (1994) proposed an hybrid model between $k-\varepsilon$ and $k-\omega$, the Shear-Stress Transport (SST) $k-\omega$. The $k-\omega$ SST combines the advantages of both models by using the $k-\omega$ formulation near the wall boundary and gradually change to $k-\varepsilon$ formulation away from the wall. In addition, once $k-\omega$ model needs no damping function, the $k-\omega$ SST model has significantly higher numerical stability in comparison to $k-\varepsilon$ (Blazek, 2015).

The transport equations for k and ω used in $k-\omega$ SST model, for stationary conditions, are:

$$\frac{\partial(\rho k \overline{U}_j)}{\partial x_j} = P_k - \beta^* \rho k \omega + \frac{\partial}{\partial x_j}\left[(\mu + \sigma_k \mu_t)\frac{\partial k}{\partial x_j}\right] \,, \tag{1.28}$$

$$\frac{\partial(\rho \omega \overline{U}_j)}{\partial x_j} = \frac{\alpha \rho}{\mu_t} P_k - \beta \rho \omega^2 + \frac{\partial}{\partial x_j}\left[(\mu + \sigma_\omega \mu_t)\frac{\partial \omega}{\partial x_j}\right] + 2(1-F_1)\rho \sigma_{\omega_2} \frac{1}{\omega}\frac{\partial k}{\partial x_j}\frac{\partial \omega}{\partial x_j}, \tag{1.29}$$

where P_k is the production of k:

$$P_k = \min\left(2\mu_t \overline{S}_{ij}\frac{\partial \overline{U}_i}{\partial x_j}, 10\beta^* \rho k \omega\right) \,. \tag{1.30}$$

A production limiter is introduced with the term $10\beta^* \rho k \omega$ to prevent over-prediction of the turbulent kinetic energy near stagnation points, a well known disadvantage of $k-\varepsilon$ and $k-\omega$ models.

The last term of Equation 1.29 is activated by the blending function F_1 that makes the transition between the $k-\omega$ formulation near the wall ($F_1 = 1$) and the $k-\varepsilon$ formulation in the outer part of the boundary layer ($F_1 = 0$):

$$F_1 = \tanh\left(\left[\min\left(\max\left(\frac{\sqrt{k}}{\beta^* \omega d}, \frac{500\mu}{d^2 \rho \omega}\right), \frac{4\rho \sigma_{\omega_2} k}{CD_{k\omega} d^2}\right)\right]^4\right) \,, \tag{1.31}$$

where d is the distance to the nearest wall and

$$CD_{k\omega} = \max\left(2\rho\sigma_{\omega_2}\frac{1}{\omega}\frac{\partial k}{\partial x_j}\frac{\partial \omega}{\partial x_j}, 10^{-10}\right) . \tag{1.32}$$

Each of the constants α, β, σ_k and σ_ω are computed from the corresponding constants of $k-\varepsilon$ and $k-\omega$ using the blending function F_1 via $\alpha = \alpha_1 F_1 + \alpha_2(1-F_1)$, etc. The models constants are: $\alpha_1 = 5/9$, $\beta_1 = 3/40$, $\sigma_{k_1} = 0.85$, $\sigma_{\omega_1} = 0.5$, $\alpha_2 = 0.44$, $\beta_2 = 0.0828$, $\sigma_{k_2} = 1$ and $\sigma_{\omega_2} = 0.856$.

Finally, the eddy viscosity in $k-\omega$ SST is expressed as:

$$\mu_t = \frac{0.31\rho k}{\max(a_1\omega, SF_2)} , \tag{1.33}$$

where $S = \sqrt{2\overline{S}_{ij}\overline{S}_{ij}}$, and F_2 is a second blending function defined by:

$$F_2 = \tanh\left(\left[\max\left(\frac{2\sqrt{k}}{\beta^*\omega d}, \frac{500\mu}{d^2\rho\omega}\right)\right]^2\right) . \tag{1.34}$$

The turbulence model choice for the numerical simulations in this work is the $k-\omega$ SST, since this model combines the advantages of $k-\varepsilon$ and $k-\omega$ models, ensuring an adequate behaviour in both near-wall and far-field zones. The $k-\omega$ SST model is appropriate for the prediction of adverse pressure gradient flows and is superior concerning numerical stability (Menter, 1994). In addition, it is the recommended model from previous works that evaluated the cost-benefit of various turbulence models for similar configurations and flow conditions of this thesis (Badr and Harion, 2005; Turpin et al., 2010).

1.3 Wind erosion: basic aspects

This section presents fundamental concepts involving erodibility, particle take-off by aerodynamic and impact entrainment, and the modes of particle transport. Furthermore, models of particle transport for steady-state regime are discussed.

1.3.1 Threshold for initiation of particle motion

If a bed of particulate matter is exposed to atmospheric flow, several kinds of forces are exerted on the particles lying at the surface. Each particle experiences forces that are against the movement (the gravitational force F_g and the inter-particle cohesion force F_c) and lift forces exerted by the wind flow. The driving lift forces are the aerodynamic drag F_d and the aerodynamic lift F_l which are

related to the shear near the surface and hence are functions of the friction velocity (Shao, 2008). As drag and lift on the particles increase, there is a critical value of u^* at which the movement is initiated, named threshold friction velocity or static threshold ($u^*_{t_s}$), which is determined by the balance of the forces acting on the particles, schematically represented in Figure 1.4. In order to lift the grain, the moments coming due to forces F_d and F_l about the point P must exceed the resisting moments due to forces F_c and F_g:

$$r_d F_d + r_g F_l \geq r_c F_c + r_g F_g \,, \tag{1.35}$$

where r_d, r_g and r_c are the corresponding moment arm lengths associated with the forces.

In order to determine $u^*_{t_s}$, Bagnold (1941) analysed the balance of forces exerted on a spherical particle just before the take-off, considering only the gravitational force F_g and the aerodynamic drag F_d, which are expressed by:

$$F_g = \frac{\pi}{6}(\rho_P - \rho) g D^3 \,, \tag{1.36}$$

$$F_d = K_D D^2 \rho u^{*2} \,, \tag{1.37}$$

where ρ_P is the particle density, g is the gravity acceleration and K_D is a dimensionless parameter function of the particle Reynolds number, defined as $Re^* = \frac{u^* D}{\nu}$.

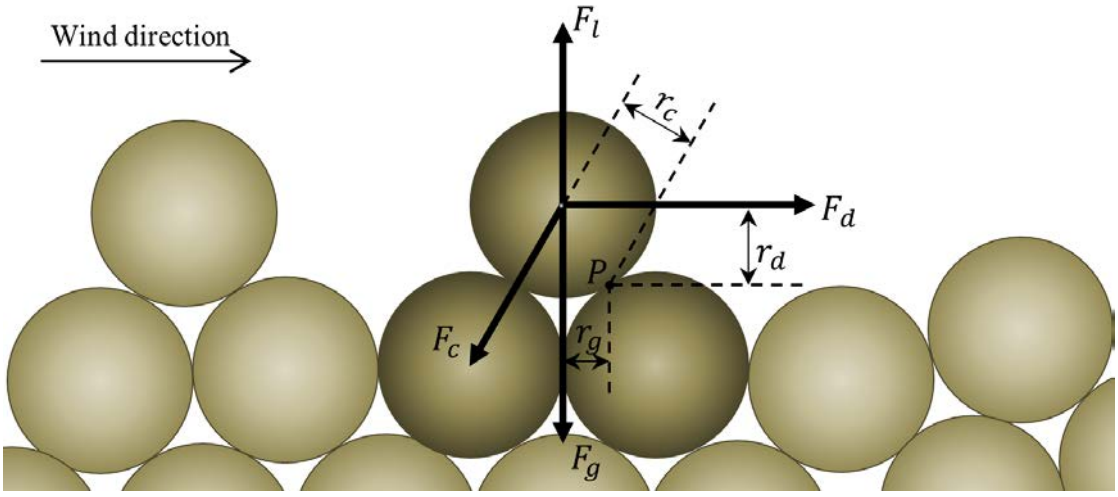

Figure 1.4: Forces acting on a particle resting on a bed surface

Combining Equations 1.35, 1.36 and 1.37, Bagnold (1941) developed an ex-

pression for the static threshold friction velocity:

$$u_{t_s}^* = A_B \left(\frac{\rho_P - \rho}{\rho} g D \right)^{\frac{1}{2}} , \tag{1.38}$$

where A_B is a dimensionless parameter, function of the friction Reynolds number at the threshold friction velocity $Re_t^* = \frac{u_{t_s}^* D}{\nu}$.

Bagnold (1941) found that A_B is nearly constant (≈ 0.1) for R_t^* larger than 3.5, which implies that $u_{t_s}^*$ increases with the square root of grain diameter. However, for $R_t^* < 3.5$, A_B is not constant due to the importance of the interparticle cohesion forces for the smaller diameters ($D \lesssim 100\mu m$).

Several expressions for $u_{t_s}^*$ considering also the influence of cohesion forces have been proposed, combining theory and fitting to experimental data (Iversen and White, 1982; Greeley and Iversen, 1985; Foucaut and Stanislas, 1996; Shao and Lu, 2000). The main cohesive forces for particles free of chemical binding are:
- Van der Walls forces, due to interatomic and intermolecular interactions;
- Electrostatic forces, due to interactions between electric charged neighbouring particles;
- Capillary forces, due to the moisture that forms liquid bridges between neighbouring particles.

In the idealised situation without the influence of humidity in which capillary forces can be neglected, a linear proportion between the interparticle cohesion force and the particles size is often adopted (Shao and Lu, 2000; Cornelis et al., 2004), although Claudin and Andreotti (2006) found that the force scales with $D^{4/3}$ (instead of D). Nonetheless, it is difficult to determine accurately each of these forces, since they are sensitive to the granular material properties, such as particle shape, surface texture, soil mineralogy and packing arrangement (Shao, 2008).

Figure 1.5 shows the relative importance of the gravity force ($\sim D^3$), the interparticle cohesion force ($\sim D$), and the aerodynamic force ($\sim D^2$) as a function of particle size, at $u^* = 0.4\ m/s$ (Shao, 2008). The three forces decrease with decreasing particle size, but cohesion decrease slower than the others. Therefore, for fine particles (less than 10 μm), the cohesive force dominates over the gravity and the aerodynamic forces.

The above discussion for the threshold velocity was developed in the context of monodisperse granular bed. New issues arise when the granular bed is composed of polydisperse particles or includes non-erodible roughness elements. This issues are discussed in Section 1.4.

1.3.1.1 Influence of bed slope on the threshold

The threshold friction velocity $u_{t_s}^*(\theta)$ on a surface with a slope $\tan\theta$ is significantly different from that found in a flat bed due to the distinct relative contributions of the forces acting on the particle. In this case, the gravitational force

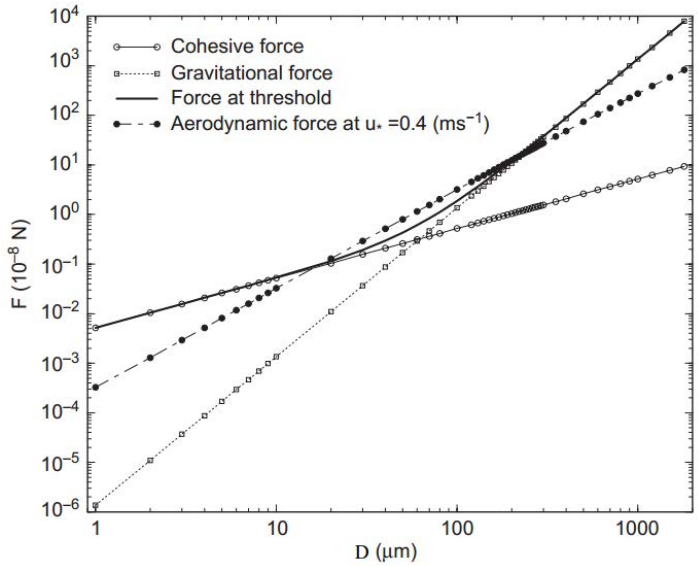

Figure 1.5: Plots of the gravity force, the cohesion force and the aerodynamic force as a function of particle size, at $u^* = 0.4\ m/s$, from Shao (2008)

has normal and tangential components given by ${F_g}^n = F_g \cos\theta$ and ${F_g}^t = F_g \sin\theta$, respectively (Figure 1.6).

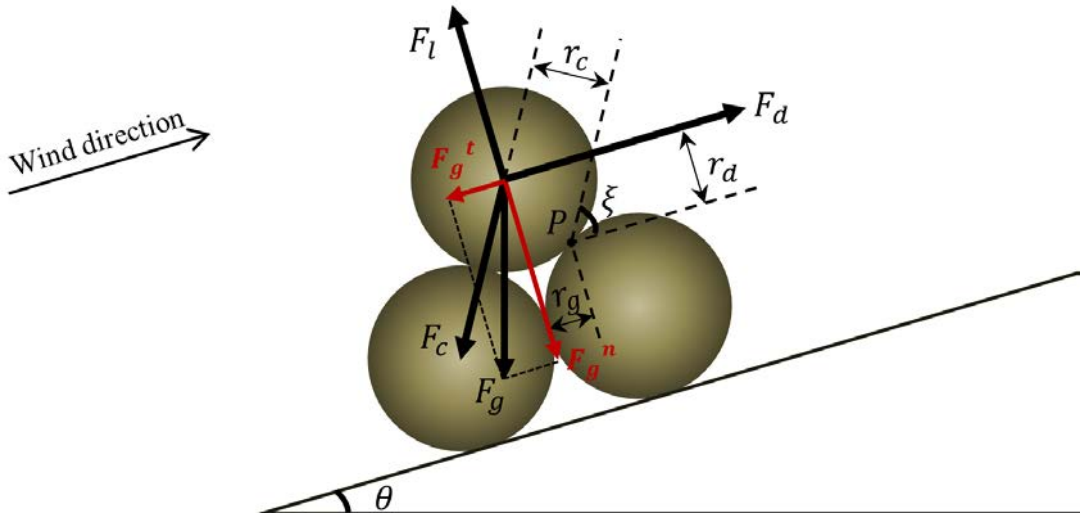

Figure 1.6: Forces acting on a particle resting on inclined surface with slope $\tan\theta$

Iversen and Rasmussen (1994) proposed a relation between $u^*_{t_s}(\theta)$ and $u^*_{t_s}(0)$ through a momentum balance about the point P, considering gravitational and

drag forces:

$$\frac{u_{t_s}^*(\theta)^2}{u_{t_s}^*(0)^2} = \cos\theta + \frac{\sin\theta}{\tan\xi}\,, \tag{1.39}$$

where ξ is the angle of internal friction (see Figure 1.6).

If the slope is positive (flow upwards), the gravity is a resistive force and thus the flow velocity must be stronger to lift the grains, that is, the threshold is higher. In contrast, if the slope is negative (flow downwards), the threshold is lower. In particular, if $\theta = -\xi$, the threshold $u_{t_s}^*(\theta)$ reaches zero. Therefore, if the slope becomes steeper than $\tan\xi$, avalanches would take place, which means that the maximum angle of stability at which particles begin to slide (the angle of repose) provides an approximation of ξ (Durán et al., 2011). However, Iversen and Rasmussen (1994) found $\xi \approx 37°$ for particles with $D > 150\ \mu m$, which is larger than the typical avalanche angles.

1.3.2 Modes of particle transport

Once the threshold friction velocity is reached, the particles get in motion. The trajectory of a particle is influenced by the atmospheric flow and also by the physical characteristics of the particle such as density and size. Bagnold (1941) was the first to define three main modes of transport by wind based on the balance of forces acting on the particles: suspension, creep and saltation (see Figure 1.7). The suspension mode is characterised by weightless grains and small enough to be driven by the turbulent flow. The suspended particles can be transported over large distances from the emission source. This type of transport occurs if aerodynamical forces are dominant. However, if the particles are too heavy to be lifted, they usually roll or slide along the surface, in the mode of transport known as creep. An intermediary situation can occur in which both the aerodynamic forces and weight are important on the transport. Thus, the particles take-off but after lifting, they fall back onto the bed and rebound, entering in motion again, characterising the saltation mode. The impact of the saltating particles on the surface can cause emissions of other particles (splash process). Saltation plays a central role in aeolian processes since it usually initiates other forms of transport, including of dust aerosols that travel in suspension (Kok et al., 2012). Therefore, to model dust emission, the transport by saltation should not be neglected.

1.3.3 Saltation transport

Particles entrainment is initiated by the aerodynamic lift of a small number of particles if the static threshold is reached. After initiation, particles are predominantly entrained by the impact of the saltating particles, which causes an exponential increase of the number of particles within the transport layer. The

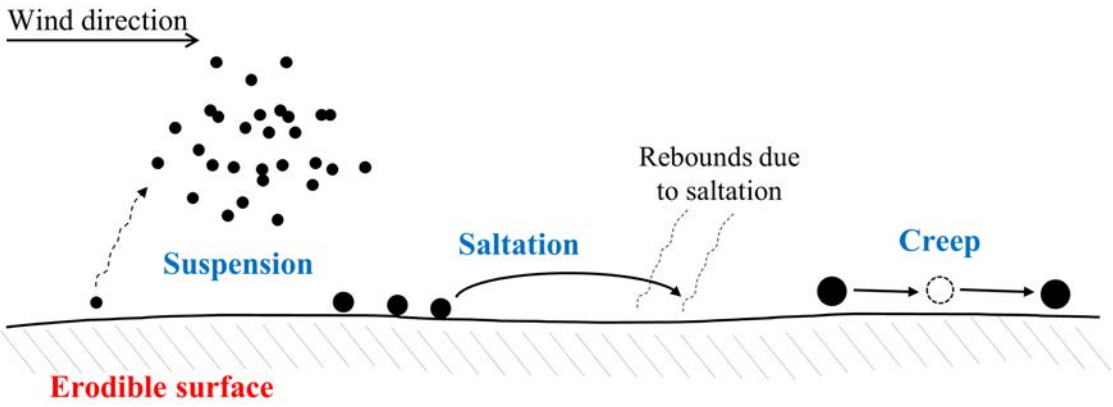

Figure 1.7: Transport modes, adapted from Furieri (2012)

great concentration of particles in a layer close to the surface, called saltation layer, results in extraction of momentum from the near-surface wind (Nickling and McKenna Neuman, 2009). Thus, there is a reduction in local wind velocity that limits further entrainments since the grains are less accelerated and impact the bed with less energy. This process causes a self-regulating feedback mechanism of saltating particles and wind (Ren and Huang, 2010; Andreotti and Claudin, 2012). A steady state is reached if there is no net erosion nor deposition of grains. An equilibrium between flow and transport is reached.

In steady state saltation, surface particles are rarely lifted by aerodynamic entrainment. Transport is sustained even if the friction velocity is lower than the static threshold. The lowest friction velocity at which saltation can be sustained after it has been started defines a dynamic (or impact) threshold ($u^*_{t_d}$).

The onset of grain motion is commonly described by the Shields number Θ, defined as:

$$\Theta = \frac{\rho u^{*2}}{(\rho_P - \rho) g D} \tag{1.40}$$

Durán et al. (2011) found an expression relating the dynamic and static Shields thresholds Θ_D and Θ_S (associated with $u^*_{t_d}$ and $u^*_{t_s}$, respectively):

$$\Theta_D = \frac{\Theta_S}{1 + b\frac{\rho_P}{\rho}\Theta_S}\,, \tag{1.41}$$

where b is a numerical constant. Therefore, if $\rho \ll \rho_P$ (the aeolian case), the dynamic threshold is lower than the static threshold. Bagnold (1941) estimated that the dynamic threshold is about 80% of the static threshold.

1.3.3.1 Equilibrium wind velocity profile

Bagnold (1941) was the first to note the differences on the wind profile in situations with and without transport. With transport, it was observed that there is a height (z_f) where the wind velocity remains almost the same (U_f), independently of how strong is the wind (see Figure 1.8). Therefore, the air velocity profiles converge to a focus points $O' = (U_f, z_f)$, being modelled as:

$$U(z) = U_f + \frac{u^*}{\kappa} \ln\left(\frac{z}{z_f}\right) , \tag{1.42}$$

where z_f and U_f are the height and the wind velocity of the focus O'.

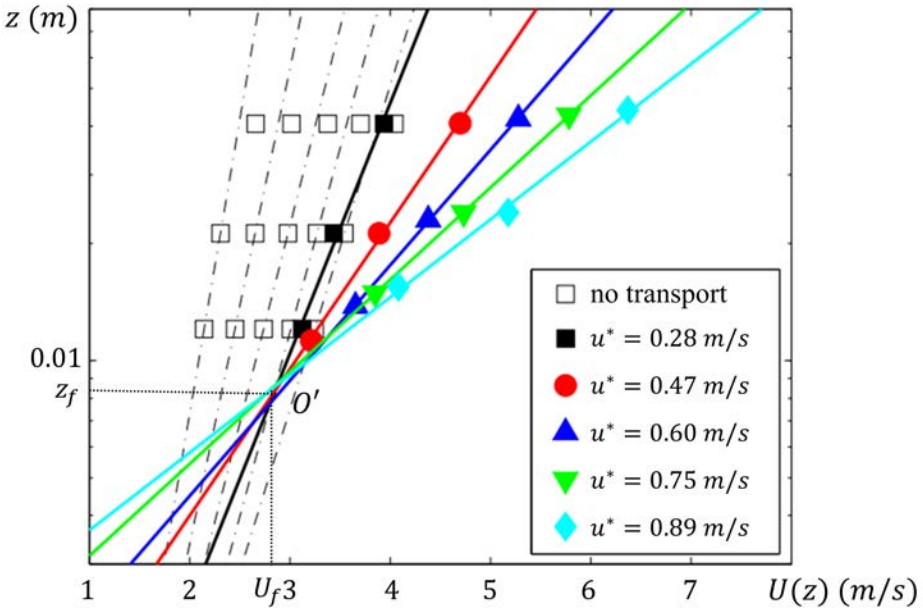

Figure 1.8: Air velocity profiles measurements obtained with sand ($D \approx 230\ \mu m$) for different friction velocities without transport (dotted lines) and with transport (solid lines), data from Ho (2012)

Equation 1.42 can be rewritten as:

$$U(z) = \frac{u^*}{\kappa} \ln\left(\frac{z}{z_0'}\right) , \tag{1.43}$$

with

$$z_0' = z_f \exp\left(\frac{-\kappa U_f}{u^*}\right) . \tag{1.44}$$

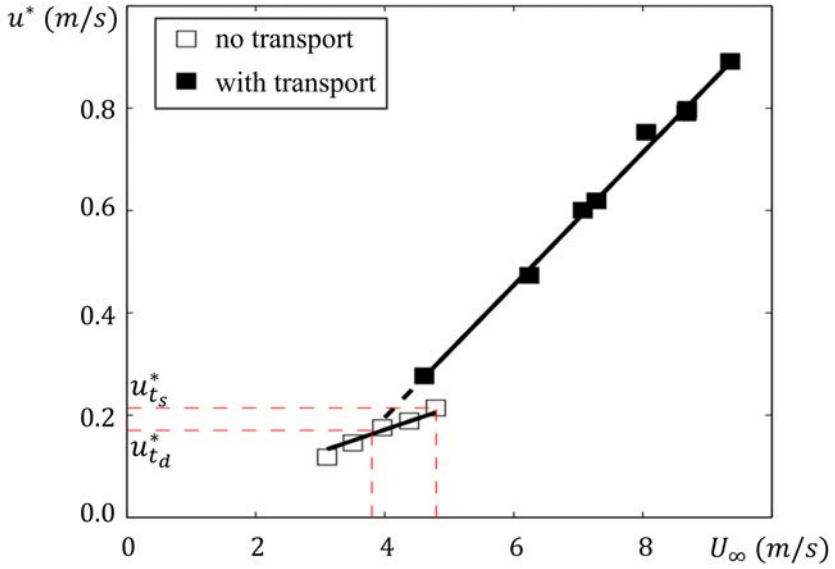

Figure 1.9: Friction velocity u^* as a function of the flow velocity U_∞ for situations without and with sand transport, data from Ho (2012)

The roughness length z_0' corresponds to the effective roughness length in presence of transport and increases with increasing friction velocity. The saltation layer thus plays a role analog to roughness elements.

Figure 1.9 shows the evolution of u^* as a function of the flow velocity U_∞, from wind tunnel measurements obtained by Ho (2012) with natural sand of mean diameter $D \approx 230\ \mu m$, revealing a discontinuous transition between no transport and transport regimes. The static threshold is obtained by the highest value of the friction velocity in the regime without transport. The dynamic threshold $u^*_{t_d}$ also can be determined from these data by extrapolating down the transport curve to intersect the curve characterised by no transport (see Figure 1.9). Ho (2012) found $u^*_{t_d} \approx 0.8 u^*_{t_s}$, which is consistent to Bagnold (1941) results.

1.3.3.2 Transport models for steady state saltation

Owen (1964) proposed that the total momentum flux in the saltation layer is partitioned between the particles and the fluid:

$$\tau = \tau_p + \tau_a \ , \tag{1.45}$$

where τ_p is the grain borne shear stress and τ_a is the air borne shear stress.

For steady state saltation, the magnitude of the air borne shear stress at the

surface, $\tau_a(z=0)$, is approximately equal to $\rho {u^*_{t_d}}^2$ (Owen, 1964). Therefore:

$$\tau_p(z=0) = \rho({u^*}^2 - {u^*_{t_d}}^2)\,. \tag{1.46}$$

Assuming that the trajectories of the saltating particles are identical, Bagnold (1941) proposed that $\tau_p(z=0)$ can be approximated by:

$$\tau_p(z=0) = \frac{Q}{L}(u_2 - u_1) \approx \frac{Q}{L}u_2\,, \tag{1.47}$$

where Q is the mass transport rate (saltation flux), defined as the mass of particles per unit of time that cross a surface of unit width perpendicular to the flow direction, u_1 and u_2 are the horizontal particle velocity at the take-off and at the impact, respectively, and L is the saltation length (Figure 1.10).

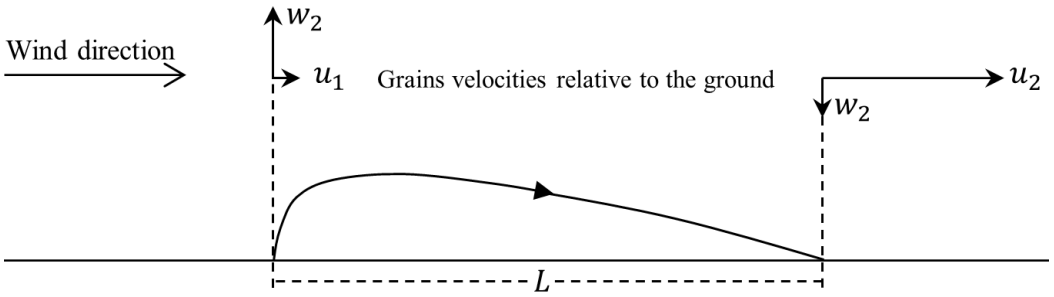

Figure 1.10: Characteristic path of a saltating particle, adapted from Bagnold (1941)

Bagnold (1941) considered $\tau_p(z=0) \approx \rho {u^*}^2$, which is valid for strong saltation when $u^* \gg u^*_{t_d}$, and assumed that the saltation length and the particle velocity at the bed scale respectively with ${u^*}^2$ and u^*. Therefore, Equation 1.47 yields the well-known Bagnold (1941) law for the mass flow rate Q, with a cubic dependence on the friction velocity u^*:

$$Q = \frac{C_B \rho}{g} {u^*}^3\,, \tag{1.48}$$

where C_B is an empirical constant.

After the classical model of Bagnold (1941), several saltation models with a cubic scaling with u^* have been developed. Most of them include a dependency with the threshold friction velocity. Sherman et al. (2013) evaluated and calibrated the empirical constants of six commonly employed transport rate models (Bagnold, 1941; Kawamura, 1951; Zingg, 1953; Owen, 1964; Hsu, 1971; Lettau and Lettau, 1978). The comparison showed that the models (all of them with a cubic scaling) produce greatly different prediction for identical environmental con-

ditions, although the general physics represented by the models are similar. Most of the models substantially over-predict transport rates. After the calibrations, the authors concluded that the disparity between the predictions from the different models is reduced from about an order of magnitude to about a quarter of an order of magnitude, but more work was necessary to better predict the saltation flux.

Recent wind tunnel experiments revealed that the saltation length and the particle velocity do not scale, respectively, with u^{*2} and u^*, but are independent of the flow strength (Creyssels et al., 2009; Ho et al., 2014). As a consequence, in contradiction with most of the laws proposed in the literature, there is a quadratic dependence of Q with the air friction velocity:

$$Q = C_H \sqrt{\frac{D}{g}} \rho (u^{*2} - u_{t_d}^{*\,2}) \,, \tag{1.49}$$

where C_H is a constant which depends on the grain size.

This quadratic relation was first suggested by Ungar and Haff (1987) and was confirmed by later numerical models (Andreotti, 2004; Almeida et al., 2007; Creyssels et al., 2009). Durán et al. (2011) found that for friction velocities well above the threshold, Q starts to scale as u^{*3}. However, the transition between the two different scaling behaviours occurs at winds larger than ordinary natural field conditions ($u^* \gtrsim 4u_{t_d}^*$). The cubic scaling also holds in the case of saltation over a rigid non-erodible bed (Ho et al., 2011; Jenkins and Valance, 2014; Berzi et al., 2015).

1.4 Influence of particle size distribution on wind erosion

The transport models usually consider materials with particles of uniform size. Aiming to apply these models to natural surfaces it is important to consider the particle size distribution of the granular material, usually described by the function $P(D)$, defined as the mass fraction of particles with diameter less than or equal to D. The corresponding particle size density function is $p(D) = \frac{dP(d)}{dD}$. Thus, the total horizontal flux for a polydisperse bed is computed by integrating the relative contributions of each size range of particles (Shao, 2008):

$$Q = \int_D Q(D) p(D) dD \,. \tag{1.50}$$

Considering a bed of particle containing non-erodible particles, Equation 1.50

is rewritten as:

$$Q = (1 - CR) \int_{D_E} Q(D)p(D)dD \,, \tag{1.51}$$

where D_E varies among all diameters of the erodible particles and CR is the cover rate of non-erodible particles, defined as the ratio of non-erodible to total surface.

Marticorena and Bergametti (1995) proposed a similar approach to account for the particle size distribution of the granular material, assuming that the relative contribution to the total flux Q of each size range is proportional to the relative surface area it occupies:

$$Q = (1 - CR) \int_{D_E} Q(D)dS(D) \,, \tag{1.52}$$

where $dS(D)$ is the normalised distribution of basal surfaces, which is computed from the particle size distribution (assuming spherical particles) as:

$$dS(D) = \frac{1}{S_{total}} \frac{3}{2\rho_P D} p(D)dD \,, \tag{1.53}$$

where S_{total} is the total bed surface.

Although Marticorena and Bergametti (1995) model considered the size distribution of the particles, it does not account for the modification of the granulometry with time (CR remains constant). Therefore, it is implicitly assumed that saltation takes place under the condition that the supply of particles for the process is unlimited. According to Nickling and McKenna Neuman (2009), the researchers tend to view the wind erosion processes from a transport limited perspective, in which the sediment flux is limited by the availability of wind momentum to transport the grains and the surface is supposed to supply an unlimited amount of particles. However, in natural conditions the surfaces tend to be supply limited, and thus the sediment flux is limited by the availability of erodible particles. However, not enough research has been done on supply limited saltation yet (Shao, 2008). The next section presents the model for wind erosion of a particle bed containing erodible and non-erodible particles developed by Descamps (2004). The model predicts emissions and the temporal decrease of the mass flow rate due to pavement phenomenon.

1.4.1 Particle emission quantification

In order to estimate accurately emissions due to wind erosion, Descamps (2004) has developed a model to quantify emissions from a bed of particles with a wide size distribution and assess the temporal evolution of the mass flow rate. Descamps (2004) model is based on the narrow correlation between particles take-off and near

wall turbulence. A possibility of a particle take-off was associated to an ejection event, which consist of a sudden displacement of a low velocity fluid parcel away from the wall region, due to the presence of streamwise counter rotating vortices. Then, for each of these possibilities, a take-off criterion based on the forces acting on the particles was tested. The bed pavement was modelled by an increment on the lift force as erosion occurs.

The turbulent vortex structures appear with spatial periodicities λ_p, whose values are dependent on the flow properties (λ_p values are adimensionalized with the kinematic viscosity and the friction velocity as $\lambda_p^+ = \frac{\lambda_p u^*}{\nu}$). Based on numerical simulations of Jimenez and Moin (1991), Descamps (2004) considered the streamwise and the spanwise spatial periodicities of the coherent structures over the particle bed as $\lambda_x^+ = 100$ and $\lambda_y^+ = 250$, respectively. The principle of the model is to subdivide the bed surface into boxes having length and width given by λ_x^+ and λ_y^+ and it was assumed that each box, which contains an ejection of fluid, is associated with a possibility of taking-off. Thus, the number of possibilities of taking-off along the bed was estimated. Vortex structures also have a time average periodicity of occurrence, given by $T_B^+ = \frac{T_B u^{*2}}{\nu} \approx 250$ (Blackwelder and Haritonidis, 1983) which was taken to be the time step of the model.

The take-off criterion of the model is based on the comparison between the forces holding the particles on the bed (due to gravity and adhesion) and the lift force exerted by the shear flow. In Descamps (2004) model the adhesion, that is the interaction of particles and a solid surface, was considered instead of cohesion since few studies were found by the authors concerning experimental measurements of interparticle cohesion forces. Therefore:

$$\overline{F}_l + F_l' \geq F_g + \overline{F}_{ad} + F_{ad}' \Longrightarrow \text{ Particle take-off}\,, \tag{1.54}$$

where $\overline{F}_l$ and $\overline{F}_{ad}$ are the mean forces of lift and adhesion, respectively, and F_l' and F_{ad}' are their fluctuations. The fluctuations account for the stochastic nature of the process and they are selected randomly from the probability density functions (pdf) of the forces. Adhesive forces also were considered as a stochastic variable since it is influenced by a several of extremely complicated factors. Indeed, laboratory experiments indicate that a wide range of scatter in the measurements of adhesion force may occur for nearly-identical macroscopic conditions Shao (2008). The threshold friction velocity is obtained when the lift force is a maximum and the adhesion force is a minimum: $F_{l_{max}} = F_g + F_{ad_{min}}$. The values $F_{l_{max}}$ and $F_{ad_{min}}$ were determined from experimental results of Mollinger and Nieuwstadt (1996) and Zimon (1982), respectively. More details concerning the probability distributions of the functions and the take-off criterion are given by Descamps (2004).

After defining the take-off criterion, the number of take-off possibilities and the time step of the model, the bed was scanned along cross and streamwise directions. For each box, a size range of a representative diameter D was selected randomly (if all particles in this size range have taken-off, then another size range was selected)

and the take-off criterion was tested. Figure 1.11 shows the basic principle of the model.

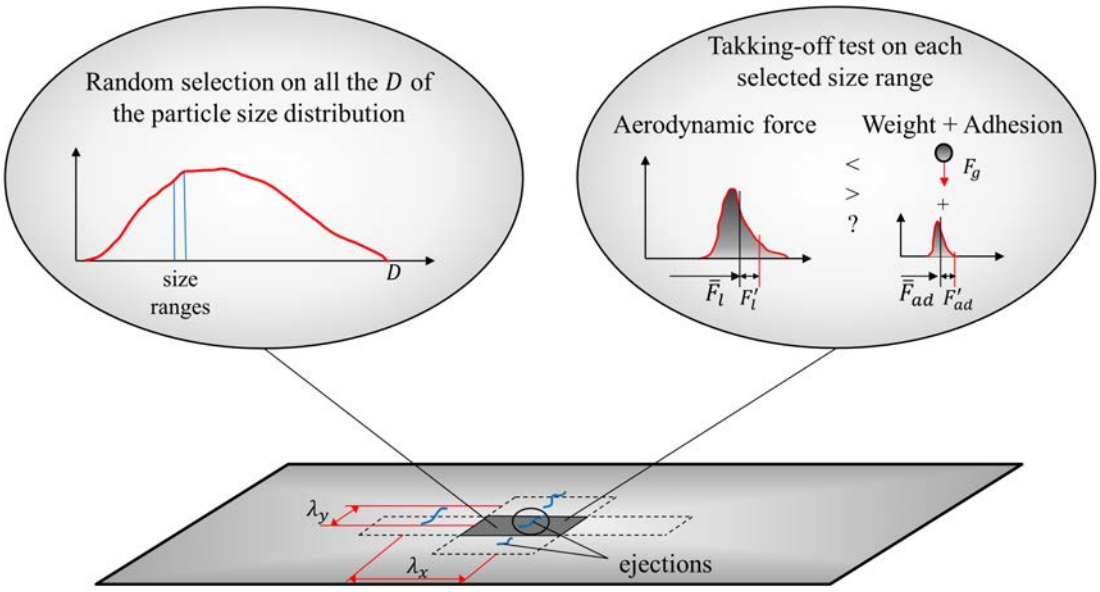

Figure 1.11: Principle of the model (Descamps, 2004)

As the surface is eroded, the entrainment of the erodible particles becomes more and more limited (pavement). Figure 1.12 shows schematically the modelling of the bed pavement by a progressive lift force reduction. For each size range, the value of the lift force is decreased when all the particles of a layer have taken-off. Therefore, the influence of the lift force on particles which are in a deeper position on the bed would gradually decrease. The erosion process cease when the maximum value of the probability density function of the lift force is lower than the minimum value of the sum of the probability density function of cohesion and weight forces.

In order to determine the increment ($\Delta F_l(D)$) that decrease the value of the lift force, Descamps (2004) defined the erosion depth ($E_{erosion}$), the depth from which the bed surface is completely overlaid by non-erodible particles. It was assumed that the particles have a spatial uniform distribution through the depth of the bed. Thereby, knowing the bed dimensions and the size distribution of the particles (input variables) it was possible to calculate, for each size range, the number of layers included into the height of the bed and the number of particles per layer. The number of layers likely to be affected by erosion $N_{erosion}$ for each size range was then determined by dividing $E_{erosion}$ by D. Therefore, the increment $\Delta F_l(D)$ was given by:

$$\Delta F_l(D) = \frac{\max(\text{pdf}(F_l)) - \min(\text{pdf}(F_g + F_{ad}))}{N_{erosion}(D)} \,. \tag{1.55}$$

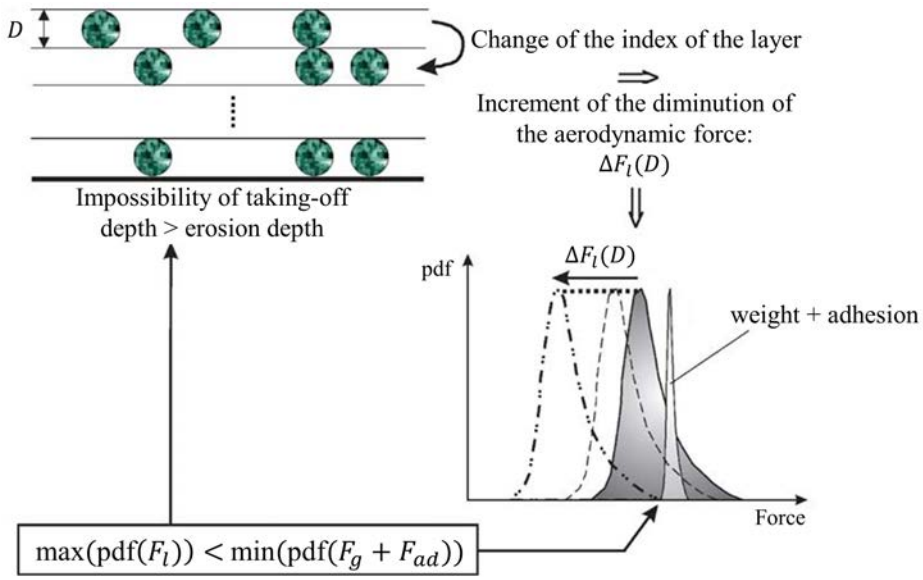

Figure 1.12: Integration of the effect of pavement in the model (Descamps, 2004)

In a first version, Descamps (2004) model did not consider the saltation transport of the particles. If the take-off criterion had been satisfied (Equation 1.54), the particle was accounted in the emitted mass flux. In order to account for the additional impact entrainments due to saltation, an adjustment in the model was done. A new take-off criterion was established considering also the impact force F_{imp}:

$$\overline{F}_l + F'_l + F_{imp} \geq F_g + \overline{F}_{ad} + F'_{ad} \Longrightarrow \text{ Particle take-off}\,. \tag{1.56}$$

For simplicity, Descamps (2004) considered that the probability of a saltating particle fails to rebound is very low and then there were no deposition. The average number of ejected particles N_{ej} due to the impact of a saltating particle was determined using the numerical results of Anderson and Haff (1991):

$$N_{ej} = 2,0667 V_{imp} - 0,4734 \qquad \text{and} \qquad N_{ej} \geq 0\,, \tag{1.57}$$

where V_{imp} is the impact velocity of the particle.

However, the work of Anderson and Haff (1991), that was used in Descamps (2004) model, considered only spherical particles of identical size. In order to account for different sizes of particles, N_{ej} was converted in an equivalent ejected mass M_{ej}. Then, after a random selection of a representative diameter, if an impact event had been identified and the correspondent mass of this range had been greater than M_{ej}, no extra emission was accounted and the particle was

definitely recorded in the emitted mass flux. Physically, this corresponds to a case in which a saltating particle impacts a coarser one that can not be ejected. However, if the mass had been lower than M_{ej}, the criterion above (Equation 1.56) would be tested, enabling an extra ejection. In this case, the saltating particle was reintegrated in the computational domain after a time step corresponding to its hop time, in a box situated at a downstream distance equal to its hop length. Then, the particle is followed until the random selection provide a corresponding mass greater than M_{ej}.

The work developed by Descamps (2004) was a first step on modelling the pavement phenomenon. As results, the model gives the time evolution of the emitted mass flux of particles and the diameter distribution of eroded particles. The results showed that it is essential to include the saltation modelling. Additional emissions related to splash represent a significant contribution to the emitted mass flux.

A limitation of the model lies in calculating the erosion depth, the parameter which characterises the pavement. As mentioned before, emissions cease with a cover rate of non-erodible particles lower than 100% (before a completely cover). Thus, other approach to model the pavement is needed. Since erosion is finalised when the friction velocity is no longer strong enough to cause emission, the partition of shear between the roughness elements and adjacent erodible surface is a relevant issue to characterise pavement phenomenon.

1.4.2 Approaches based on shear stress partitioning

There is a general consensus on the effect of non-erodible particles on wind erosion: the threshold friction velocity u_t^* increases and hence the surface erodibility and the emission mass flux decreases (Gillette and Stockton, 1989). As erosion occurs, the accumulation of non-erodible particles creates a shelter to the neighbouring erodible particles and the degree of protection depends on the geometry and the cover rate of these coarse elements. It is usual to describe the characteristics of the rough surface by the roughness density λ, defined as:

$$\lambda = \frac{nS_{frontal}}{S_{bed}} \,, \tag{1.58}$$

where n is the number of roughness elements, $S_{frontal}$ is the frontal area of the elements and S_{bed} is the area of the particle bed.

Marshall (1971) carried out wind tunnel experiments with several settings of surfaces with cylindrical and hemispheric roughness elements. The results showed that the shape and the spatial distribution of the elements have little influence in shear stress partition. The author found that the partition has a primarily dependence on the roughness density λ.

The increase in roughness density is associated with changes in the flow around roughness elements and three regimes can be identified, as shown in Figure 1.13: *isolated roughness flow*, *wake interference flow* and *skimming flow* (Lee and Soli-

man, 1977). When the roughness elements are sufficiently far apart, they act individually as obstacles to the wind without interaction with neighbouring elements, which characterises an *isolated roughness flow* regime. In a *wake interference flow* regime, the spacing between the roughness elements is small enough such that the wake associated with each element may not be completely developed and there is interaction with the neighbouring elements. Finally, in a *skimming flow* regime, roughness elements are so closely packed that wakes are unable to form in the gaps between them, leading to weak circulations between the elements.

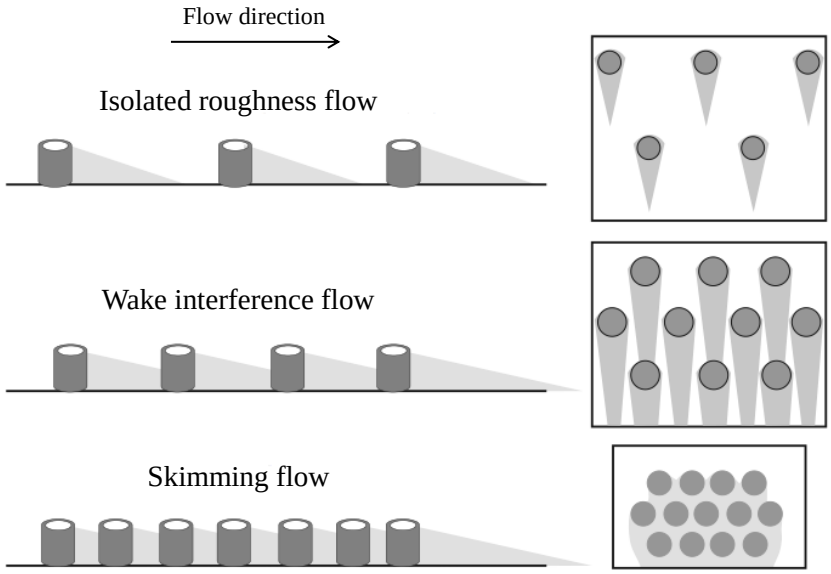

Figure 1.13: Development of wakes shed from roughness elements for the different flow regimes and their interaction with neighbouring elements (Nickling and McKenna Neuman, 2009)

Schlichting (1936) proposed that the total drag force imparted to a rough surface due to the fluid flow can be decomposed into a sum of the force acting on the roughness elements (F_R) and a force acting on the ground surface (F_S). The force F_R arises from the pressure difference on the roughness elements and F_S arises from the friction on the ground surface. Thus, the total shear stress acting on the surface τ can be written as:

$$\tau = \rho u^{*2} = \tau_R + \tau_S \,, \tag{1.59}$$

where u^* is the overall friction velocity, τ_R is the pressure drag on the roughness elements and τ_S is the friction drag on the ground surface.

The shear stress τ_S' acting on the exposed ground surface, which drives wind erosion, is related to τ_S by:

$$\tau_S' = \rho u_S^{*2} = \frac{\tau_S}{1 - \sigma\lambda} \,, \tag{1.60}$$

where u_S^* is the friction velocity on the ground surface (surface representing erodible particles) and σ is the ratio of roughness elements basal to frontal area ($\sigma\lambda = CR$).

A theoretical model was proposed by Raupach (1992), based on the idea that the wake and drag properties of an isolated roughness element can be characterised by an effective shelter area and volume. The shelter area describe the surface stress deficit behind the element and the shelter volume, the attenuation of drag on other obstacles in the element wake. It was assumed that the combined effective shelter can be calculated by randomly superimposing individual shelters. However, the validity of this hypotheses is limited to low values of roughness densities λ. As λ increases, element wake interactions become stronger and their collective effect cannot be described by superimposition. Raupach (1992) model is given by:

$$\frac{\tau_S'}{\tau} = \frac{1}{(1-\sigma\lambda)(1+\beta'\lambda)}\,, \tag{1.61}$$

where β' is the ratio of drag coefficient of an individual roughness element to the drag coefficient of the bare surface. The parameter β' accounts for roughness element shape effects and entirely controls the partition of drag.

Raupach et al. (1993) argued that the threshold of particle movement is determined by the maximum shear stress at any location on the surface (τ_S''), not by the spatially averaged stress. Thus, Raupach et al. (1993) assumed that τ_S'' for a particular rough surface is equal to τ_S' for a less dense rough surface, that is, $\tau_S''(\lambda) = \tau_S'(m\lambda)$, where m (≤ 1) is an empirical constant that accounts for the spatial heterogeneity of the shear stress distribution. This fact results in the equation for the maximum surface shear stress ratio:

$$\frac{\tau_S''}{\tau} = \frac{1}{(1-m\sigma\lambda)(1+m\beta'\lambda)}\,. \tag{1.62}$$

Based on the adjustment of the equation above to experimental data, Raupach et al. (1993) suggested $\beta' = 90$ and $m = 0.5$ if the erodible exposed surface is flat, and $m = 1$ if the erodible surface is stabilised (surface contoured by wind into a equilibrium bed topography, with a scour region in front of and a deposition region behind each roughness element).

The Raupach et al. (1993) model has been assessed by several works in order to test and refine the parameters β' and m (Wolfe and Nickling, 1996; Crawley and Nickling, 2003; Brown et al., 2008; Walter et al., 2012). A general conclusion is that the proposed formulation is valid, nonetheless, presents shortcomings. Musick et al. (1996) and Crawley and Nickling (2003) found that the parameter β' has some degree of dependency on the aspect ratio of the roughness elements. The range of values obtained for β' and m is relatively large, which makes difficult the identification of appropriate values for a specific surface with non-erodible

elements (Walter et al., 2012). The values for m vary widely and inconsistently and the physical meaning of m remains to be addressed (Crawley and Nickling, 2003).

Marticorena and Bergametti (1995) characterised the effect of roughness elements in terms of aerodynamical roughness length z_0. According to the authors, if the roughness elements are not too closely spaced, an internal boundary layer grows behind the roughness element. The modified wind profile in the internal boundary layer also follows the logarithmic law for $z < \delta$ (δ is the height of the internal boundary layer):

$$U(z) = \frac{u_S^*}{\kappa} \ln\left(\frac{z}{z_{0S}}\right) , \tag{1.63}$$

where z_{0S} is the aerodynamic roughness length of the underlying surface (the smooth roughness length), u_S^* is the friction velocity at the intervening surface (see Equation 1.60).

By intersecting the wind velocity profiles in the atmospheric boundary layer and in the internal boundary layer (Equations 1.8 and 1.63) at the top of the internal boundary layer ($z = \delta$), the ratio between u_S^* to the overall friction velocity can be expressed by:

$$\frac{u_S^*}{u^*} = 1 - \frac{\ln\left(\frac{z_0}{z_{0S}}\right)}{\ln\left(\frac{\delta}{z_{0S}}\right)} . \tag{1.64}$$

The length δ increases downstream from the roughness element and can be related to the fetch distance x by:

$$\frac{\delta}{z_{0S}} = a \left(\frac{x}{z_{0S}}\right)^{0.8} , \tag{1.65}$$

where a is an empirical constant. Since δ is dependent on x, the local shear stress increases until an equilibrium value is eventually reached. However, Marticorena and Bergametti (1995) found that the differences of u_S^*/u^* values computed using a unique value for x, equal to 10 cm, are of the order of 20%. These results indicated that the stress partition is not very sensitive to x but is mainly dependent on the values of the roughness lengths, and then it was assumed $x = 10$ cm.

Thus, in their model, drag partition is a function of z_0 and z_{0S}. But the specifications of these parameters for practical use are not easier than the parameters from Raupach et al. (1993) model (Shao, 2008). Furthermore, the simplifications made to estimate δ limit the range of roughness elements concentration and type that the model can represent adequately. The assumption in the Marticorena and Bergametti (1995) model of a constant value of 10 cm to the downwind distance

limits the application of the model to only small-scale wakes, as this parameter is not independently scaled to the object size but an absolute distance (King et al., 2005).

King et al. (2005) evaluated and compared the Marticorena and Bergametti (1995) and the Raupach et al. (1993) models with field and wind tunnel measurements. The Raupach et al. (1993) model requires more inputs than are required in Marticorena and Bergametti (1995) model, but its predictions were better owing to the incorporation of more variations in the roughness geometry and the flow modifications. Generally, it was found that both models provided very good agreement for the wind tunnel experiments, however their performance when tested in a field environment were less favourable.

The models presented above improved the comprehension of the shear stress partition. Despite their importance, there are shortcomings, most of all concerning the large variations found in model parameters and the limited range validity to certain types of rough surfaces. In this sense, Computational Fluid Dynamics (CFD) is an alternative that can provide information that is difficult to obtain from experimental studies, since it can be applied to simulate the flow over surfaces with any shape and arrangement of roughness elements. Thereby, numerical techniques offer possible foundation for development of new theories of shear stress partition (Li and Shao, 2003).

Li and Shao (2003) applied a CFD model to investigate the effects of the dimensions and distribution of roughness elements on drag partition. A large-eddy simulation model with a $k-\varepsilon$ subgrid closure was used to generate turbulent flows over roughness elements. In the first set of simulations, the effect of roughness element dimension was studied using a single cylinder. The roughness density λ was varied by changing cylinder heights and diameters. It was found that pressure drag is more sensitive to roughness element height than to its diameter. Thus, the authors suggest that the parameter β from Raupach (1992) model should be modified to account for the height of roughness elements.

The second set of simulations of Li and Shao (2003) analysed the sheltering effect of roughness elements on drag partition, considering two roughness elements (the roughness density was kept constant but the relative position between the two cylinders was varied). The authors found that the relative position between roughness elements does influence the calculation of drag partition. It was also studied whether the roughness element distribution affects drag partition testing arrays of non-uniform roughness elements with the same roughness density. According to their simulations, apparently the arrangement of roughness elements does affect drag partition, but the impact is rather small. The authors concluded that the effect arising from the distribution of roughness elements requires further theoretical investigation and additional numerical simulations should be performed.

Turpin et al. (2010) performed RANS numerical simulations with different configurations of rough surfaces. The turbulence effects were accounted for by using the $k-\omega$ Shear Stress Transport (SST) model. The whole set of simulations models an erosion event and the objective was to determine the friction velocity

experienced by the ground surface (representing the erodible fraction of the surface) as a function of the bed roughness element characteristics (representing the non-erodible particles). The work analysed the parameter R_{fric}, defined as:

$$R_{fric} = \frac{u_S^*}{u_0^*}\,, \tag{1.66}$$

where u_0^* is the mean friction velocity for a surface without roughness elements. This parameter reflects the evolution of the friction velocity applied to the exposed surface as the number and height of the roughness elements increase. Results showed relatively large differences in u_S^* for configurations with the same roughness density λ and different aspect ratios. The authors proposed a mathematical formulation to include the different influences of each parameter:

$$1 - R_{fric} = A.(CR)^M.\left(\frac{S_{frontal}}{S_{floor}}\right)^N\,, \tag{1.67}$$

where $S_{frontal}$ and S_{floor} are respectively the frontal and the basal areas of a cylindrical roughness element, and A, M and N are coefficients determined by the numerical simulations.

The numerical simulations performed by Turpin et al. (2010) were validated with previous experimental studies concerning roughness elements by comparing the measured and the modelled values of the friction velocity ratio $R_t = \frac{u_S^*}{u^*}$ (see Figure 1.14).

Furieri et al. (2013a) found that Equation (1.67) is also valid for surfaces containing roughness elements with non-uniform aspect ratios (the roughness elements diameters and heights were randomly chosen from a defined range of values).

Turpin et al. (2010) and Furieri et al. (2013a) demonstrated that their numerical simulations are in close agreement with experimental data. However, the configurations of rough surfaces has a limited range of validity once the maximum cover rate of their simulation was 12%. The particle size distribution found in nature and particularly in granular materials from storage yards of industrial sites can present higher values of cover rates. Additional numerical simulations should be done in order to adjust the values of the coefficients A, M and N for a larger range of cases.

1.5 Aeolian erosion of granular material stockpiles

Studies of wind erosion and the transport of granular materials on sloped surfaces have application in natural scenarios (such as sand dunes) and industrial

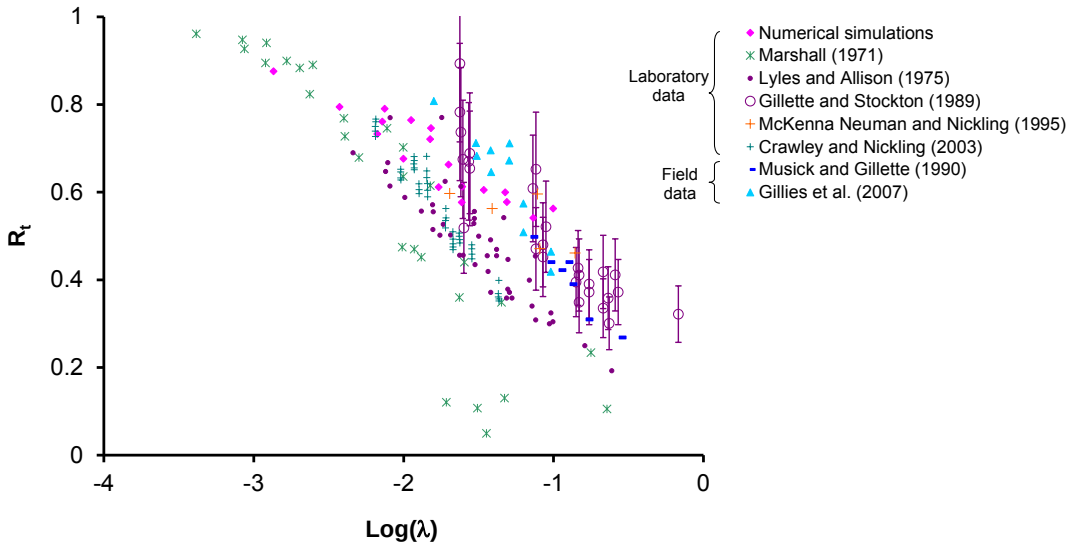

Figure 1.14: Comparison of the modelled values of the friction velocity ratio R_t (from numerical simulations) with experimental data (Marshall, 1971; Lyles and Allison, 1975; Gillette and Stockton, 1989; Musick and Gillette, 1990; Mckenna Neuman and Nickling, 1995; Crawley and Nickling, 2003; Gillies et al., 2007), data from Turpin et al. (2010)

scenarios (such as granular material stockpiles). The presence of an obstacle generates pressure gradients in flow field near the wall, which causes the flow path lines to diverge. The velocity profiles for these kinds of flow can no longer be described by the conventional approaches of boundary layer. As a consequence, the erosion processes are more complex for sloped surfaces than for horizontal surfaces. In addition, the forces acting on the particles change, which affects the threshold for motion (Section 1.3.1.1).

1.5.1 Fluid flow around stockpiles

Figure 1.15 shows the path lines around three different stockpiles from validated numerical simulations carried out by Badr (2007) (RANS numerical simulations with $k-\omega$ Shear Stress Transport (SST) model for turbulence closure). Although the flow pattern depends on piles shape and dimensions, similar flow structures can be highlighted. There is an incident flow region (at the windward wall foot of the piles) with high levels of pressure where the flow velocity is near zero (stagnation zone). If the windward surface has a steep inclination, the deceleration may create a small separation at pile's foot, leading to a reverse flow downwards (Shao, 2008). As the incident flow impinges on the windward wall, the flow progressively accelerates towards the stockpiles top and lateral walls, where maximum velocities are recorded. A separation occurs on the edges of the windward wall of the piles creating a recirculation zone behind the pile, where low pressure levels are perceived. This region is characterised by vortex structures in which the flow is

redirected to the downstream slope. The path lines in the recirculation zone are directly related to the geometry of the obstacle but in general are complex and three-dimensional. Figure 1.15 shows that two vortex structures are shed from the lateral sides, especially for the oblong stockpile.

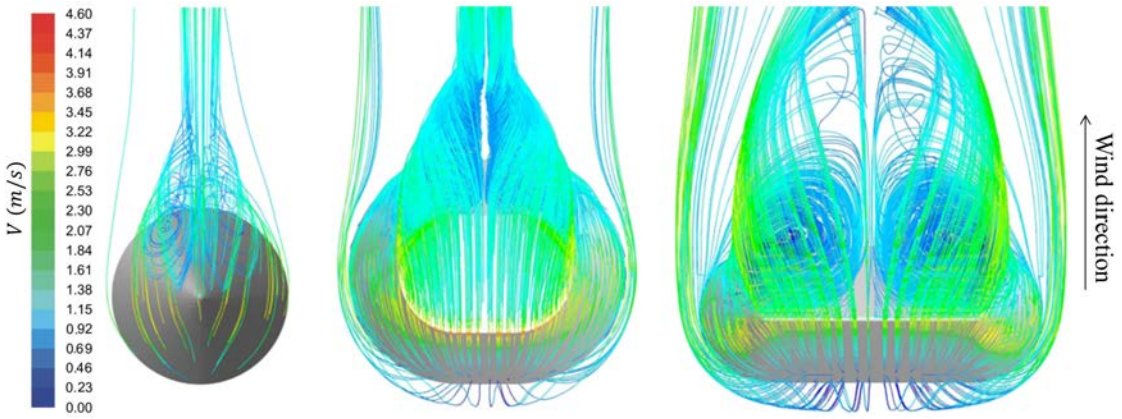

Figure 1.15: Top view of path lines coloured by velocity magnitude for different pile shapes: cone, oblong flat topped and oblong sharp crested, respectively (Badr, 2007)

A wake zone develops behind the piles, characterised by intense circulatory motion, low velocity and high turbulence intensity. Figure 1.16 shows the two-dimensional structure of the secondary flow downstream a dune (Walker and Nickling, 2002). After several dune heights downwind, the flow re-attaches the surface and a boundary layer begins to be developed. The flow patterns in the downstream area and the re-attachment distance depend on the velocity and the direction of the flow and in the obstacle geometry and size.

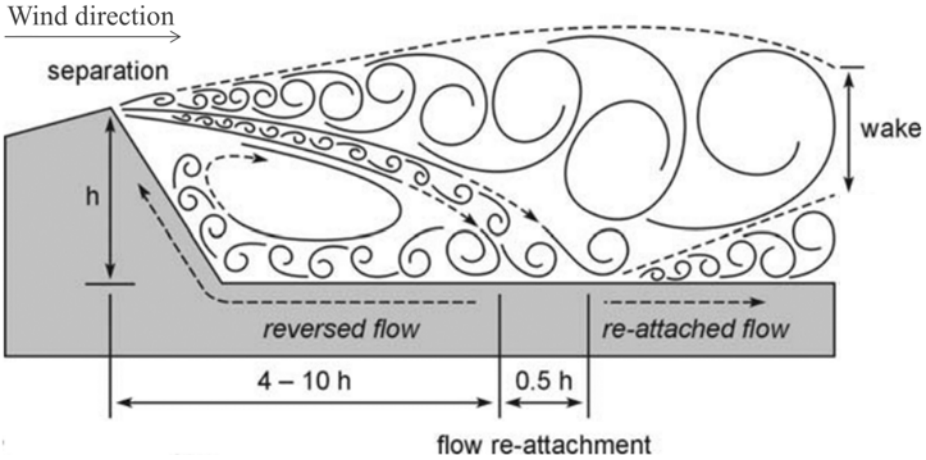

Figure 1.16: Structure of the flow downstream of dunes, from Walker and Nickling (2002)

1.5.2 Emission quantification from stockpiles of industrial sites

The analysis of the flow around a stockpile have shown that a granular material stockpile exposed to a turbulent flow has areas with different degrees of wind exposure. The United States Environmental Protection Agency (USEPA) proposed a methodology to estimate dust emissions from diffuse sources by mapping the areas of the pile with different erosion potential (USEPA, 2006).

The USEPA (2006) guidance is based on the determination of an emission factor, which attempts to relate the quantity of a pollutant discharged to the atmosphere with an activity associated with the release of that pollutant. In the case of particulate emissions due to wind erosion from stockpiles, the emission factor (EF) is calculated as follows, expressed in units of grams per square metre per year:

$$EF = K \sum_{i=1}^{T} P_i \,, \tag{1.68}$$

where K is the particle size multiplier, T is the number of disturbances per year (a disturbance is defined as an action that results in the exposure of fresh surface material, such as addition or removal of material from the pile surface), and P_i is the erosion potential corresponding to the observed fastest observed wind for the i^{th} period between disturbances, given in g/m^2:

$$\begin{cases} P_i = 58 \left(u^* - u^*_{t_s}\right)^2 + 25 \left(u^* - u^*_{t_s}\right) \,, \\ P_i = 0 \qquad \text{for } u^* \leq u^*_{t_s} \,. \end{cases} \tag{1.69}$$

Since incoming flow is disturbed by the presence of an elevated obstacle, the friction velocity has important variations along the surface. Then, if the pile significantly penetrates the surface wind layer (with a height-to-base ratio exceeding 0.2), USEPA (2006) recommends to determine the friction velocity u^* as:

$$u^* = 0.10 \left(\frac{u_s}{u_r}\right) u^+_{10} \,, \tag{1.70}$$

where u_s is the surface wind velocity (measured 25 cm above the pile surface), u_r is the approach wind velocity (measured at a height of 10 m) and u^+_{10} is the fastest wind for a period between disturbances (measured at a height of 10 m).

The distribution of the ratio u_s/u_r allows the representation of the different degrees of wind exposure over the pile. The pile area is divided into subareas of constant u^*, each constituting a separate source. Hence, the subdivided areas and the friction velocities for each subdivision are required for estimating dust

emissions.

Based on previous wind tunnel experiments, USEPA (2006) report provides the wind exposure in terms of distribution of normalised velocity values u_s/u_r for an isolated stockpile with two classical pile shapes (conical and oval with flattop) and for three incident flow angles. Figure 1.17 shows the distribution for an incident flow perpendicular to the piles.

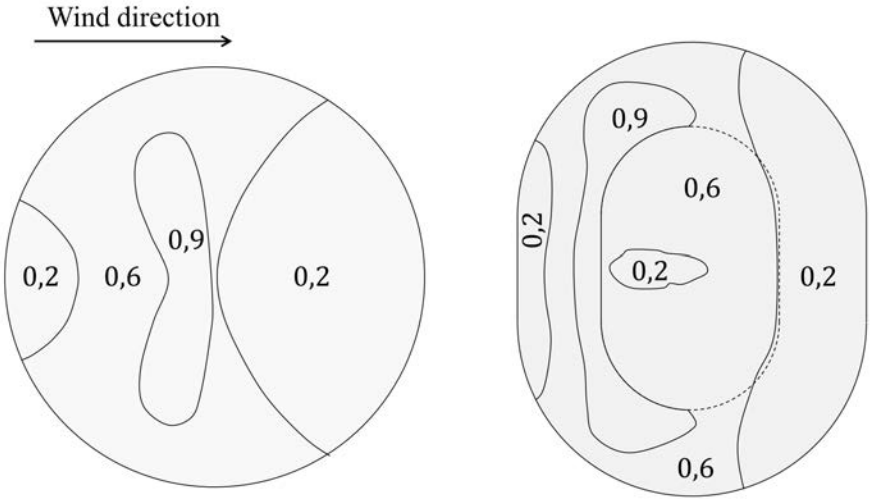

Figure 1.17: Contours of normalised surface wind velocities (u_s/u_r) for two configurations of stockpiles (USEPA, 2006)

The USEPA (2006) is the most widely used methodology to estimate emissions from diffuse sources. However, the provided u_s/u_r distribution do not cover the wide variety of piles shapes and compositions that can be found on industrial sites. To extend this approach to any configuration of interest more quickly and with less technical equipment, numerical simulations have been used to retrieve the distribution of the normalised velocity (Badr and Harion, 2007; Toraño et al., 2007; Turpin and Harion, 2009; Cong et al., 2012). The CFD numerical calculations can even improve emission estimates since a fine spatial resolution when computing velocity distribution over the piles can provide more detailed data.

In order to calculate the erosion potential, the value of the threshold friction velocity is needed. This value is mainly dependent on the surface material of the pile. USEPA (2006) provides values of threshold friction velocity for certain surface types determined by field measurements with a portable wind-tunnel. It was also recommended the estimation of $u^*_{t_s}$ from the dry aggregate structure of the soil by a hand sieving test that determines the mode of the surface aggregate size distribution. Nonetheless, the erosion potential does not explicitly take into account the particle size distribution as an input data of the model. Therefore, the methodology may not encompass all the important differences that could arrive between the extensive variety of materials found in industry. Piles containing

different materials may have the same erosion potential according to Equation 1.69 but distinct particulate matter emissions.

Furieri (2012) proposed a modification in the modelling of the erosion potential P in order to explicitly account for the amount of non-erodible particles among input data. The modification was based on data of the emitted mass obtained by wind-tunnel experiments with an isolated and perpendicular oriented oblong stockpile. The tests comprised four mass percentages of erodible particles ($\%EP = 50\%, 65\%, 80\%$ and 90%) and three values of free stream velocities (6, 7 and 8 m/s). It was found an expression relating the erosion potential to the percentage of erodible particles in the mixture:

$$P_{mod} = b_1(\%EP)^{b_2}(u^* - u^*_{t_s})^2 + c_1(\%EP)^{c_2}(u^* - u^*_{t_s})\,, \tag{1.71}$$

where the values found for the coefficients were: $b_1 = 0.0047$, $b_2 = 3.90$, $c_1 = -0.0007$ and $c_2 = 3.90$.

Equation 1.71 takes into account the influence of the proportion of non-erodible particles and it was found to be a good representation of the erosion potential for all tested velocities of the experiments (Furieri, 2012). However, the fitting to find the parameters of the models included only one experimental configuration (isolated stockpile with a bimodal granulometry and oriented perpendicularly to the wind). Therefore, in order to guarantee the validity of the formulation, it should be further assessed for other configurations.

In the present work, a different approach to include the influence of non-erodible particles on emission quantification will be proposed (Section 3.3), based on the physical process involved on pavement phenomenon.

Chapter 2

Aeolian erosion over particle beds

This chapter presents a model to quantify emissions from bed particles due to wind erosion with a wide range of particle sizes. The modelling of the pavement process was based on the results of the shear stress partition over a rough surface, obtained from numerical simulations. In addition, wind tunnel experiments were carried out in order to better comprehend the pavement phenomenon and estimate emissions from a bed of particles containing a bimodal size distribution. The experimental results were also used to validate each step of the modelling, including the global emitted mass and the final characteristics of the bed surface

2.1 A novel approach to estimate particles emission from a bed of granular material exposed to a turbulent flow

This section is presented as an article entitled "A novel approach to estimate particle emissions from a bed of granular material exposed to the Atmosphere". It is intended to be submitted to "Journal of aerosol science".

A novel approach to estimate particle emissions from a bed of granular material exposed to the Atmosphere

M.C. Caliman[a,b], B. Furieri[a,b], J.M. Santos[a], A. Ould El Moctar[c], J.-L. Harion[d], A. Valance[e], P. Dupont[f], N.C. Reis Jr[a]

[a] *Universidade Federal do Espírito Santo, DEA, 29060-970 Vitória, ES, Brazil*
[b] *Instituto Federal do Espírito Santo, 29056-255 Vitória, ES, Brazil*
[c] *Polytech. Nantes, Laboratoire de Thermocinétique, F-44306 Nantes, France*
[d] *Mines Douai, EI, F-59500 Douai, France*
[e] *Universit de Rennes 1, Institut de Physique, F-35042 Rennes, France*
[f] *INSA de Rennes, LGCGM, F-35043 Rennes, France*

Abstract

Dust emissions due to aeolian erosion of exposed granular materials are strongly influenced by grain size distribution. Non-erodible particles that are too heavy to be lifted into the air play a protective role in the aeolian erosion process attenuating emission, which is known as the pavement phenomenon. To date, there is no approach that reliably predicts the reduction in emissions caused by their presence on an aggregate surface. In this work, an analytical model was developed to quantify emissions from particle beds with a wide size distribution. As non-erodible particles accumulate, changes in surface characteristics create an increasing shelter for the erodible portion of the bed until the shear on the erodible surface reaches a minimum and emissions cease. The proposed emission model describes the relationship between this minimum value of wind shear and the eroded depth of the bed after the pavement, which in turn gives the emitted mass. In addition, wind tunnel experiments were carried out in order to broaden knowledge of the pavement phenomenon and validate the modelling. A bimodal granulometry of sand with erodible and non-erodible particles was used for the tested velocities. Three kinds of measurements were carried out: (i) successive weighing of the emitted mass, (ii) eroded depth of the bed at regular time intervals and (iii) final cover rates of the non-erodible particles using digital analysis of sand bed pictures after experiments. Good agreement between the modelling and experimental results was found. The emission model proposed herein is a simple algebraic expression that demands low computational effort. This ap-

proach may serve as a base for an emission model for application in granular materials stockpiles.

Keywords: wind erosion, non-erodible particles, pavement, fugitive emissions, emission model

1. Introduction

Emissions due to aeolian erosion of exposed granular materials are strongly influenced by the grain size distribution. Granular materials may present a wide particle size distribution containing coarse particles that are not lifted by wind flow. Several experimental studies have shown that the presence of these non-erodible particles affects dust emission, promoting a temporal decrease in emitted mass flux [1, 2, 3, 4, 5]. As the surface is eroded, the coarse particles accumulate and protect the bed surface from erosion, which is known as the pavement phenomenon. Therefore, it is important to consider temporal variability in surface conditions to develop wind erosion models [6]. Nonetheless, aeolian transport is often viewed as a steady-state process, and most available emission models are applied to particle beds with a homogeneous size distribution. Some models account for the wide range of particle sizes in the bed [7, 8, 9], however, modifications of soil size distribution with time are not usually considered. The work of Descamps et al. [10] was the first attempt to fill this gap. The authors developed a stochastic model that quantifies the temporal evolution of the emitted mass flux in a bed of granular material with a wide size distribution exposed to a turbulent flow. To model pavement, Descamps et al. [10] assumed that erosion is finalised when the bed is completely overlaid by non-erodible particles. However, experimental results showed that when erosion stops, potential erodible particles still remain on the surface [4, 5].

The present work aims to investigate the pavement phenomenon and propose an emission model, which includes a new approach to characterise the influence of non-erodible particles accumulation. The non-erodible particles protect the erodible surface by both covering the surface and creating downstream wake zones of reduced wind shear stress on the intervening bare surface [11, 12, 13]. As the concentration of larger particles in the bed increases, the mean shear on erodible surfaces decreases until it is no longer significant to cause emissions. Thus, pavement modelling in the proposed model is related to the wall shear stress evolution as wind erosion modifies

the surface. The partition of shear between non-erodible particles and adjacent erodible ones is investigated using numerical simulations of turbulent flow over a rough surface and a mathematical formulation to associate the geometrical characteristics of the non-erodible particles and the mean friction velocity on the erodible surface (Section 2.2). Based on this formulation, the final conditions of the bed, such as the eroded depth and the cover rate of non-erodible particles, were determined by assuming that after pavement, the friction velocity reaches a minimum value. Then, besides providing the emitted mass from a particle bed, the model gives the final state of the bed topography (Section 2.3). An experimental study in a wind tunnel, described in Section 3, was conducted to validate the modelling results (final characteristics of the bed surface and global emissions estimates).

2. Erosion model

2.1. Grain entrainment and saltation

Wind erosion of a particle bed is initiated by aerodynamic entrainment, whenever the velocity exceeds a critical value called the static threshold. The onset of grain motion is commonly described by the Shields number Θ, defined as the ratio between the shear force exerted by a fluid on a particle at the bed surface and the effective particle weight:

$$\Theta = \frac{\rho u^{*2}}{(\rho_P - \rho) g D} \,, \tag{1}$$

where u^* is the friction velocity, ρ is the fluid density, ρ_P is the particle density, g is gravity and D is the particle diameter.

Bagnold [14] investigated the static threshold Shields number Θ_S (corresponding to the static threshold friction velocity $u^*_{t_s}$) based on the balance of forces acting on a particle. The author found that Θ_S is nearly constant for large particles ($\Theta_S \approx 0.01$), which implies that $u^*_{t_s}$ increases with $\sqrt{D}$ in these cases. However, for small particles, Θ_S is not constant and increases rapidly as diameter decreases. As particle size decreases, interparticle cohesion forces can no longer be neglected and its effect plays a dominant role in controlling threshold motion conditions. Since the pioneering work of Bagnold [14], other studies have been devoted to investigating the threshold Shields number and erodibility conditions for the particles [15, 16, 17, 18]. In the present work, the erodibility of the particles was assessed by a take-off

criterion obtained by Shao and Lu [19], who presented a simple expression relating the threshold friction velocity $u_{t_s}^*$ and the particle diameter D:

$$u_{t_s}^* = 0.11\sqrt{\frac{\rho_P - \rho}{\rho} gD + \frac{\gamma}{\rho D}}\,, \tag{2}$$

where γ is a surface energy that characterises the cohesion.

Equation 2 implies that if interparticle cohesion is considered, $u_{t_s}^*$ is proportional to $\sqrt{c_1 D + c_2 D^{-1}}$ (instead of $\sqrt{D}$). For large particles, the term $c_1 D$ dominates over $c_2 D^{-1}$, which is consistent with $\Theta_S \approx 0.01$. This criterion is in good agreement with a large number of wind tunnel measurements [20]. Shao and Lu [19] recommended values of γ ranging between 1.65×10^{-4} and 5.00×10^{-4} kg/s^2. In this work, $\gamma = 2.86 \times 10^{-4}$ kg/s^2 was used, as obtained by Kok and Renno [21] experimentally fitting Equation 2 to the threshold required to lift erodible particles.

The take-off criteria (illustrated in Figure 1) allows the estimation of the range of particle sizes liable to take-off. For a given friction velocity u^*, there will be a range of critical diameters in which particles are emitted. Outside of this range, particles remain on the surface due to gravitational forces for larger particles and high cohesion forces for smaller particles.

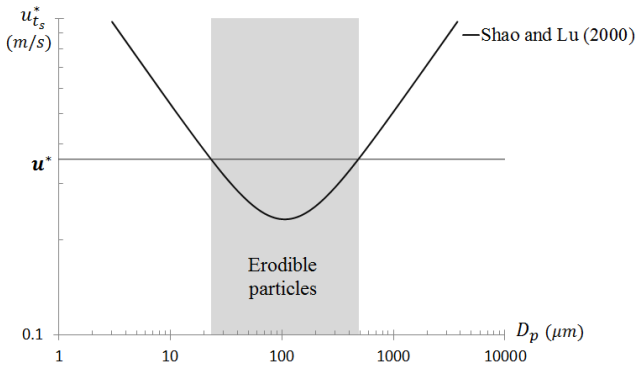

Figure 1: Take-off criterion

In the early stage of erosion, aerodynamic forces are mainly responsible for the entrainment of particles. Transport is initiated by aerodynamic entrainment of a small number of particles if the static threshold Θ_S is reached. These particles may hop along the surface, and the impact of saltating grains

on the bed surface can eject other particles. After saltation has initiated, subsequent lifting of surface particles occurs predominantly due to impact. Then, transport can be sustained even below the static threshold. The minimum velocity at which the combined action of wind forces and saltation impacts are capable of retaining particles in movement is called the dynamic threshold (Θ_D). The dynamic threshold is lower than the static threshold and is also fairly constant ($\Theta_D \approx 0.008$) for large grains [22, 23, 17]. For smaller particles (typically $\lesssim 100\mu m$), there is an increase in Θ_D due to the importance of cohesion forces.

The expression of the threshold friction velocity versus the particle diameter presented herein (Equation 2) was developed for beds composed of particles with monodispersed size distribution, without roughness elements as non-erodible particles. The effects of the presence of roughness elements are taken into account by the shear stress distribution between the roughness elements and the ground surface.

2.2. Shear stress partition

The shear stress partition has been investigated by several researchers by means of theoretical [24, 7] and experimental [25, 26] approaches. Despite the importance of these works, they present shortcomings, most of all concerning large variations found in model parameters and the limited range validity for certain types of rough surfaces. Computational Fluid Dynamics (CFD) is a valuable alternative that can be applied to simulate the flow over surfaces with different shapes and arrangements of roughness elements. Different configurations may be too costly and time consuming to be predicted by experimental techniques.

Schlichting [27] proposed that the total drag τ imparted to a rough surface can be written as:

$$\tau = \rho u^{*2} = \tau_R + \tau_S \,, \tag{3}$$

where τ_R is the pressure drag on the roughness elements and τ_S is the friction drag on the ground surface.

The shear stress τ'_S acting on the exposed surface (erodible), which drives wind erosion, is related to τ_S by:

$$\tau'_S = \rho u^{*2}_S = \frac{\tau_S}{1 - CR} \,, \tag{4}$$

where u_S^* is the mean friction velocity on the erodible fraction of a rough surface and CR is the cover rate of the surface by the roughness elements.

Turpin et al. [28] performed numerical simulations with different configurations of rough surfaces to depict the pavement process by determining the friction velocity experienced by the erodible fraction of particles as a function of the changes in bed topography, i.e., the increase in number or the height of the roughness elements. The work analysed the parameter R_{fric} (Equation 5), which reflects the evolution of the friction velocity applied to the exposed surface as erosion occurs:

$$R_{fric} = \frac{u_S^*}{u_0^*} \,, \tag{5}$$

where u_0^* is the mean friction velocity on a surface without roughness elements. Then, Turpin et al. [28] developed a mathematical relationship to include the cover rate and particles geometrical parameters on R_{fric}:

$$1 - R_{fric} = A(CR)^M \left(\frac{S_{frontal}}{S_{floor}} \right)^N \,, \tag{6}$$

where $S_{frontal}$ and S_{floor} are respectively the frontal and the basal areas of a cylindrical roughness element, and A, M and N are coefficients determined by the numerical simulations.

Furieri et al. [29] found that Equation 6 is also valid for surfaces containing particles with different aspect ratios (non-uniform distribution of roughness elements). However, this formulation was tested for cover rates lower than 12%. Nonetheless, the particle size distribution found in nature, and particularly in granular materials from storage yards of industrial sites, can present higher cover rate values. Therefore, in the present study, additional numerical simulations were carried out in order to adjust the values of the coefficients A, M and N for a larger range of cases. The studied configurations correspond to a bed of granular material, in which the non-erodible particles are represented by non-uniform cylindrical roughness elements randomly distributed, emerging at various levels from the surface (see Figure 2). The transport of particles is not taken into account in the numerical simulations.

The parameters that define each test are: the range of roughness elements diameter D_r and height h_r (proportionally to D_r) and the number of

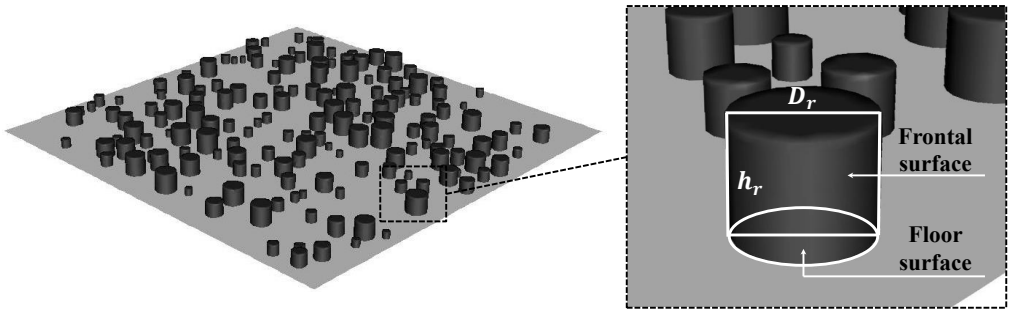

Figure 2: Random positioning of the non-uniform roughness elements

roughness elements n_r ($n_r = 0$ corresponds to a surface without roughness elements, i.e., $u_S^* = u_0^*$). The ratio $S_{frontal}/S_{floor}$ and the cover rate CR are determined for each simulated case according to:

$$\frac{S_{frontal}}{S_{floor}} = \frac{4}{\pi}\frac{\overline{h}_r}{\overline{D}_r}\,, \tag{7}$$

$$CR = \frac{\frac{\pi}{4}\sum_{r}^{n_r} {D_r}^2}{S_{bed}}\,, \tag{8}$$

where $\overline{D}_r$ and $\overline{h}_r$ are, respectively, the mean diameter and the mean emergent height of the roughness elements, and S_{bed} is the area of the bed. Table 1 presents the configurations of the simulated beds.

The commercial software FLUENT was used to solve the three-dimensional Reynolds averaged equations of mass and momentum. The turbulence effects were accounted for by using the $k-\omega$ Shear Stress Transport (SST) model. The computation domain is represented by a parallelepiped (30×30 mm base and 100 mm height). Periodic conditions were applied to inlet and outlet boundaries, which means that the outlet was used to set the inlet profiles in a cyclic way until a fully developed flow was established. The simulations are initialised with a uniform velocity distribution, and the mass flow is fixed for a corresponding mean longitudinal velocity value equal to 8 m/s. The upper and lateral boundaries were defined as symmetry (normal gradients of all variables are set to zero) and the lower limits (roughness elements and ground walls) as smooth walls with no-slip conditions.

Table 1: Configurations of particle bed covered by cylindrical roughness elements tested in the numerical simulations. u_S^* is the mean value of the friction velocity on the erodible surface, calculated using the numerical results of the shear stress distribution. R_{fric} is calculated using Equation 5

Test	D_r (mm)	$\frac{h_r}{D_r}$ (%)	n_r	CR	$\frac{S_{frontal}}{S_{floor}}$	u_S^*	R_{fric}
1	$1.0-3.0$	$20-100$	48	15.04	0.80	0.2044	0.58
2	$1.0-3.0$	$20-100$	62	20.21	0.72	0.1990	0.57
3	$1.0-3.0$	$20-100$	91	25.02	0.76	0.1829	0.52
4	$1.0-3.0$	$20-100$	102	27.04	0.77	0.1738	0.50
5	$1.0-3.0$	$20-100$	116	30.01	0.73	0.1762	0.50
6	$1.0-3.0$	$20-100$	121	32.04	0.79	0.1588	0.45
7	$1.0-3.0$	$20-100$	156	35.12	0.77	0.1583	0.45
8	$1.0-3.0$	$20-100$	158	37.07	0.77	0.1490	0.43
9	$1.0-3.0$	$20-100$	181	40.12	0.74	0.1530	0.44
10	$1.0-3.0$	$60-100$	62	20.51	1.00	0.1750	0.50
11	$1.0-3.0$	$60-100$	113	30.35	1.00	0.1630	0.47
12	$1.0-3.0$	$60-100$	190	40.21	1.01	0.1398	0.40
13	$1.0-3.0$	$80-120$	63	20.67	1.31	0.1607	0.46
14	$1.0-3.0$	$80-120$	114	30.40	1.28	0.1472	0.42
15	$1.0-3.0$	$80-120$	190	40.02	1.27	0.1250	0.36
16	$0.5-1.5$	$80-100$	168	15.19	1.14	0.1980	0.57
17	$0.5-1.5$	$80-100$	238	20.12	1.14	0.1840	0.53
18	$0.5-1.5$	$80-100$	309	25.10	1.14	0.1721	0.49
19	$0.5-1.5$	$80-100$	410	30.19	1.14	0.1619	0.46
20	$0.5-1.5$	$80-100$	507	34.06	1.14	0.1510	0.43
21	$0.5-1.5$	$140-160$	168	15.11	1.90	0.1610	0.46
22	$0.5-1.5$	$140-160$	238	20.04	1.90	0.1601	0.46
23	$0.5-1.5$	$140-160$	309	25.03	1.90	0.1398	0.40
24	$0.5-1.5$	$140-160$	410	30.13	1.90	0.1332	0.38
25	$0.5-1.5$	$140-160$	507	34.12	1.91	0.1281	0.37

The calculation domain was divided into two parts to allow a good mesh refinement near the wall in the spanwise and streamwise directions, with hexahedral and pentahedral elements, and a coarser mesh with quadrilat-

eral elements elsewhere for better computational efficiency. This is necessary since strong velocity gradients and important fluid interactions occur near the wall. The computational set up (modelling choices including meshing, turbulence closure and domain configurations) was based on previously validated numerical calculations (cf. Turpin et al. [28] and Furieri et al. [29]).

Figure 3 shows the friction velocity contours on the erodible surface, determined from the shear stress distribution, for two different simulations: Tests 15 and 16. Test 15 presents higher values of the ratio $S_{frontal}/S_{floor}$ and CR than Test 16. Therefore, in Test 15, the wakes formed behind the elements are expanded and interact with the neighbouring particles, leading to a drop in the friction velocity on most of the underlying surface (see Figure 3(a)) and a lower mean value of the friction velocity on the erodible surface (u_S^*), as shown in Table 1.

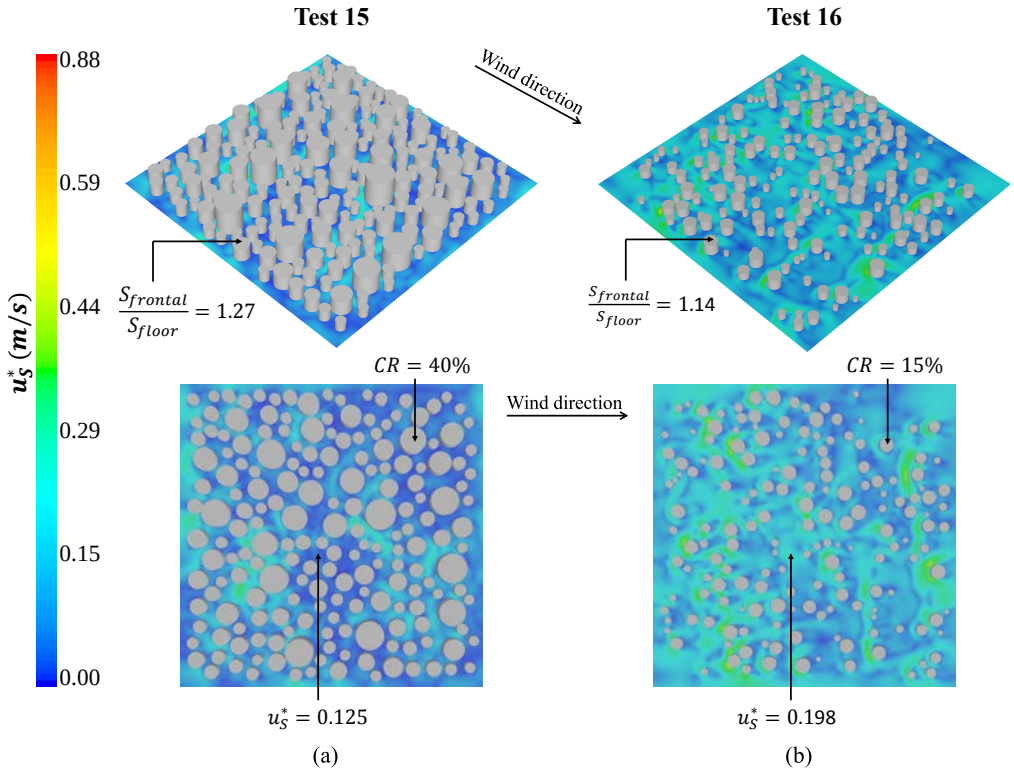

Figure 3: Friction velocity contours on the erodible surface for Tests (a) 15 and (b) 16

The coefficients A, M and N in Equation 6 were recalculated based on the numerical results: $A = 0.188$, $M = 0.313$ and $N = 0.216$. The relative errors between the numerical values of u_S^* and those calculated by Equations 5 and 6 with the new coefficients do not exceed 5%. The proposed formulation was found to be in good agreement with the numerical results ($R^2 = 0.97$).

2.3. Roughness evolution and emission prediction

The main purpose of the erosion model is to determine particle mass emission based on the eroded depth of a particle bed for a given velocity, taking advantage of the formulation in Equation 6. The particles were assumed to be cylindrical, with height equal to the diameter of the base. The input variables of the model are wind velocity (U_∞), bed dimensions and the characteristics of the granular material. Given the particle size distribution, the mass fraction of particles α_i for each size range of particles with representative diameter D_i is:

$$\alpha_i = \frac{M_i}{M_{tot}} = \frac{V_i}{V_{tot}} \,, \tag{9}$$

where M_i and V_i are, respectively, the mass and the volume of particles from the range i, M_{tot} is the total mass of the particles and V_{tot} is the total volume occupied by the particles of the bed, calculated as:

$$V_{tot} = \sum_i V_i = \sum_i n_i V_{D_i} \,, \tag{10}$$

where n_i is the number of particles encompassed in the range of D_i and V_{D_i} is the volume of one particle with diameter D_i (for cylindrical particles $V_{D_i} = \pi D_i^3/4$).

The total volume of particles is related to the volume of the (V_{bed}) through the volume fraction φ:

$$\varphi = \frac{V_{tot}}{V_{bed}} \,, \tag{11}$$

which can be written as a sum of partial volume fractions φ_i of each diameter D_i:

$$\varphi = \sum_i \varphi_i \,, \tag{12}$$

where:

$$\varphi_i = \frac{V_i}{V_{bed}} = \alpha_i \varphi \, . \tag{13}$$

A spatial uniform distribution of particles was assumed along the height of the bed. For each representative diameter D_i of a given size range, the number of layers in the bed height was calculated by dividing the height of the bed (H_{bed}) by D_i (height of the particle). Therefore, the number of particles per layer $n_{i/l}$ for each diameter D_i is:

$$n_{i/l} = n_i \frac{D_i}{H_{bed}} = \frac{\varphi_i S_{bed} D_i}{V_{D_i}} \, . \tag{14}$$

Once the number of particles per layer for each representative diameter is known, it is possible to establish a correspondence between the cover rate of non-erodible particles and the eroded depth. The initial cover rate of non-erodible particles (CR_i) is equivalent to the partial volume fraction φ_{NE} of the non-erodible diameters. Thus, CR_i can be determined from:

$$CR_i = \alpha_{NE} \varphi \, , \tag{15}$$

where α_{NE} is the mass fraction of the non-erodible particles.

Figure 4 shows the evolution of CR as a function of H for a unimodal size distribution of non-erodible particles. In this case, the relation between CR and H is:

$$CR = aH + CR_i \, , \tag{16}$$

where $a = CR_i / D_{NE}$ and D_{NE} is the diameter of the non-erodible particles. Equation 16 is valid for the velocities in which the erodibility of the particles does not change and for a monodisperse size distribution of non-erodible particles. If the size distribution of non-erodible particles is polydispersed, the surface covered by non-erodible particles for a given bed depth is calculated by successive summation on all non-erodible particle sizes, and the value of a is found through curve fitting to these data.

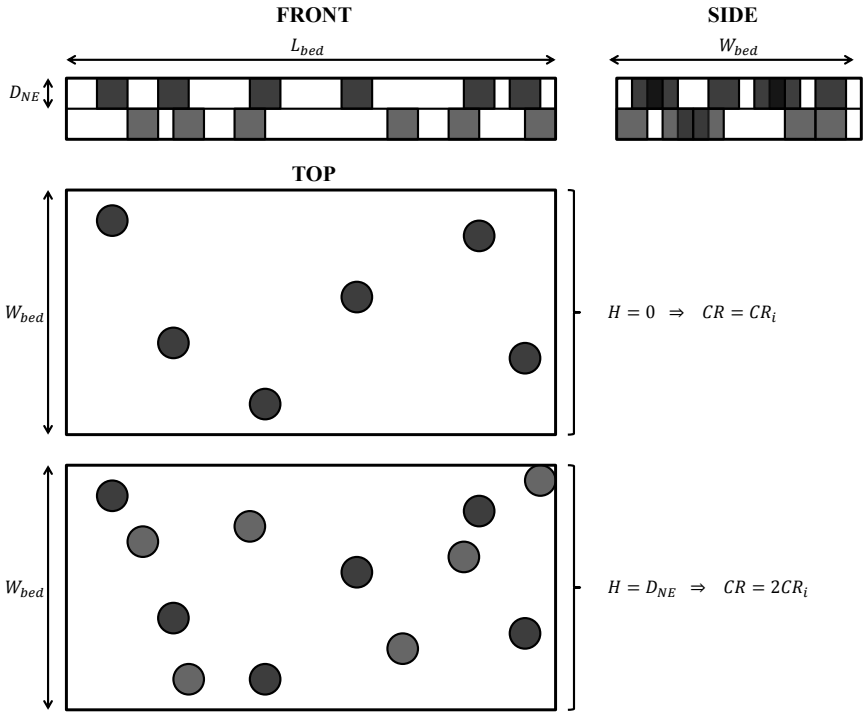

Figure 4: Evolution of the surface proportion occupied by non-erodible particles (CR) as a function of the depth (H)

Subsequently, in order to relate airflow velocity and eroded depth, Equation 6 was explored. The progressive emergence of non-erodible roughness elements during erosion was simulated by the successive numerical computations. The emergent height of the exposed non-erodible particles ($\overline{h}_r$) is required for the calculation of $S_{frontal}$, which was assumed to be equivalent to the eroded depth of the bed H. Therefore, using Equation 16, Equation 6 can be rewritten as:

$$1 - R_{fric} = A(aH + CR_i)^M \left(\frac{4H}{\pi D_{NE}}\right)^N . \tag{17}$$

Equation 17 provides a relation between the eroded depth H and R_{fric}. As non-erodible particles accumulate, friction velocity on the erodible fraction of the surface u_S^* decreases until a minimum value in which no take-offs

occur; the pavement phenomenon occurs and erosion is terminated. Since emissions due to the impact of particles from saltation are accounted for, u^*_{MIN} is given by the dynamic threshold of the erodible particles, that is, u^*_{MIN} is the minimum value of $u^*_{t_d}(D_E)$ among all diameters of erodible particles D_E. Nonetheless, the minimum value possible for u^*_{MIN} is approximately $u^*_{t_d}(100\mu m) \approx 0.14 m/s$ once that for smaller diameters, cohesion becomes important and Θ_D increases. Therefore, $u^*_{MIN} = \max(u^*_{t_d}(D_E), 0.14)$.

At the point where no erosion occurs, the parameter R_{fric} reaches a minimum value, that is velocity dependent (given by $R_{MIN} = u^*_{MIN}/u^*_0(U_\infty)$), and the eroded depth reaches a maximum H_f, which gives Equation 18:

$$1 - R_{MIN} = A(aH_f + CR_i)^M \left(\frac{4H_f}{\pi D_{NE}}\right)^N . \tag{18}$$

In conclusion, given the particle size distribution of the bed and the air flow velocity, it is possible to calculate the final eroded depth of the bed after the pavement phenomenon H_f (Equation 18). As a result, the emitted mass (E_f) can be determined from the emitted volume using a simple algebraic expression, as shown in Equation 19:

$$E_f = (1 - \alpha_{NE})\rho_{bed} H_f S_{bed} , \tag{19}$$

where $\rho_{bed} = \varphi\rho_P$.

A synthesis of the model is shown in Figure 5.

3. Experimental study

Wind tunnel experiments were conducted in the present work to investigate the temporal evolution of the pavement process and measure the emitted mass in order to validate the proposed model. Therefore, (i) successive weighing of particle emissions and (ii) measurements of the eroded depth of the bed at regular time intervals were performed and (iii) photographs of the sand bed were taken after the experiments.

The experiments were carried out in a 6.6 m long wind tunnel with a square cross-section (see Figure 6) coupled to a centrifugal fan controlled by a frequency speed variator. Downstream from the fan, there is a long steel wind tunnel section. At the beginning of this section, a series of spires was installed

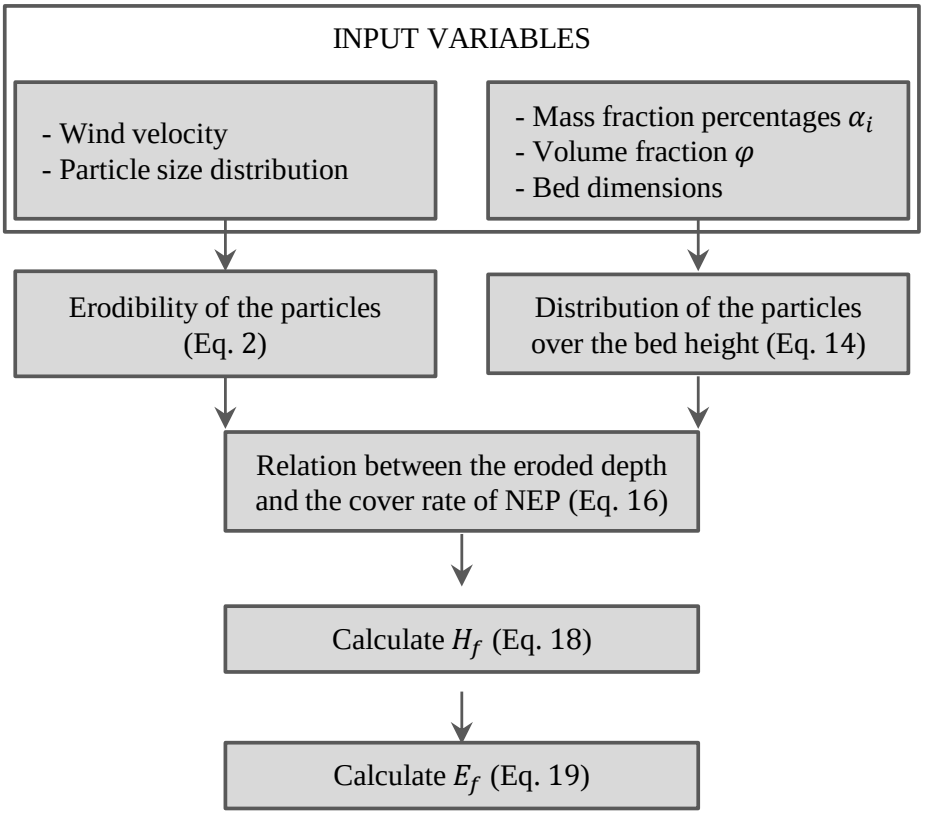

Figure 5: Chart of the model

to hasten the development of the boundary layer, followed by the test section, in which the glass walls allow measurements and photography. After the wind tunnel test section, there is a trap box where the sand can be collected and weighed. More details of the wind tunnel and its characterisation can be found in Ho et al. [30].

Two types of grains with $\rho_P = 2650\ kg/m^3$ were used in the experiments: fine sand and coarse sand, with mean diameters of 200 and $1000\mu m$, respectively. The fine sand and the coarse sand are erodible and non-erodible for the three tested velocities: 6.7, 8.5 and 9.6 m/s. The experiments comprise wind-tunnel tests containing a bimodal granulometry with two different mass fractions of non-erodible particles (α_{NE}): 10 and 20%. Fine sand was white and the coarse sand was black to allow for the visualisation of non-erodible

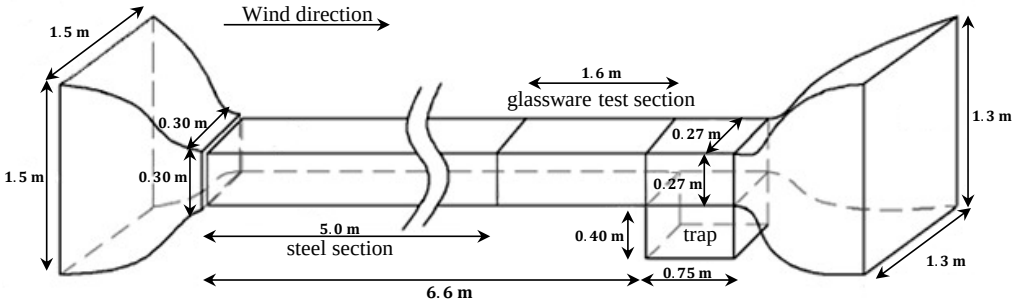

(a)

(b)

(c)

(d)

Figure 6: (a) Scheme of experimental facilities, composed of: (b) Centrifugal fan, (c) Wind tunnel, (d) Test section and sand trap

particle accumulation. It was therefore possible to calculate the proportion of the surface occupied by non-erodible particles after the pavement phenomenon by means of digital analysis.

The wind tunnel was covered by the bimodal sand bed with $\rho_{bed} \approx 1600$ kg/m^3 ($\varphi = 0.6$), and the fan was switched on for a period of 10 minutes. Nonetheless, the flow was periodically blocked (after $1, 2, 3, 4, 5$ and 7 minutes) for sampling and weighing of emitted particles in the sand trap and at the exit of the wind tunnel. By weighing this sand, global emissions and the emission rate were estimated. It is important to recall that the transport is in an unsteady state and thus the streamwise sand transport changes with distance and time.

A high quality camera was installed over the wind-tunnel top wall (transparent one). Then, the eroded depth of the bed was determined at regular time intervals using a Laser sheet. The experimental setup using the laser

is illustrated in Figure 7(a). The aim was to determine the eroded surface depressions in accordance with the displacements of the laser trace. A laser sheet was pointed along the central plane direction of the sand bed. The camera registered the evolution of the eroded surface by photographing the bed every 15 seconds until the end of the 10 minutes. The camera position remained unchanged during the entire experiment. Therefore, it was possible to scale the displacement of the laser with the number of pixels in the pictures through calibration with the displacement of an object with known size (see Figure 7(b)). The final laser images (Figure 7(c)) were post-processed using the commercial software Matlab.

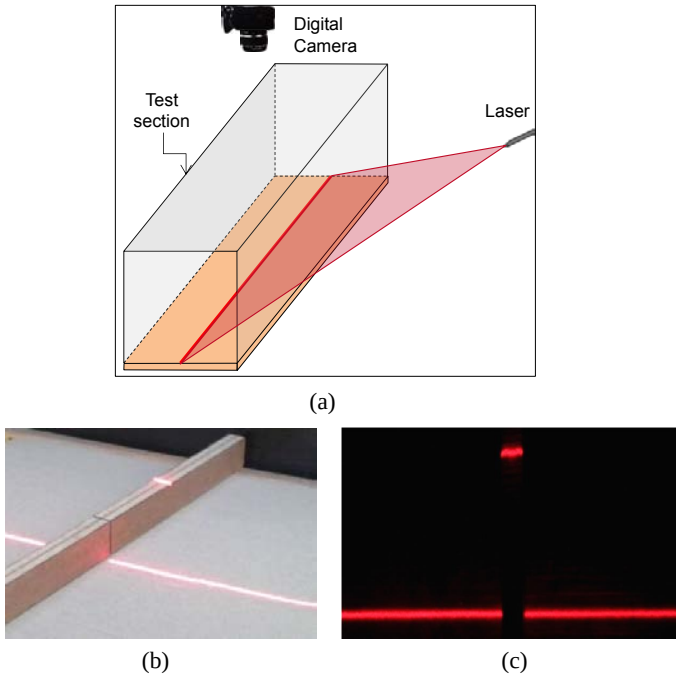

Figure 7: (a) Laser experimental setup, (b) Calibration of distances and (c) Final picture

The emission rate, defined as the emitted mass per unit width per unit time, can be deduced from the evolution of the eroded depth as:

$$\dot{e}(t) = (1 - \alpha_{NE})\rho_{bed} \int_0^{L_{bed}} \frac{\partial H(x,t)}{\partial t} dx = (1 - \alpha_{NE}) L_{bed} \rho_{bed} \frac{d\overline{H}}{dt} , \qquad (20)$$

where L_{bed} is the length of the particle bed.

The emission rate is estimated by the weighing measurements of sand as:

$$\dot{e}(t) = \frac{\Delta M}{W_{bed}.\Delta t} \,, \tag{21}$$

where ΔM is the emitted mass during the time interval Δt.

Finally, the pavement phenomenon was also explored by means of digital analysis of the final pictures from the sand bed using a thresholding method and the commercial software Matlab. It was possible to visualise the accumulation of coarse black particles and to calculate the final cover rate.

4. Experimental results

4.1. Temporal evolution of the pavement process

Figure 8 presents the influence of α_{NE} and U_∞ on the emission rate obtained using Equation 21. During the first minutes, $\dot{e}(t)$ remains nearly constant (until $t = t_0$) but decreases afterwards due to the pavement phenomenon. The constant flux during the first minutes can be explained using an analogy to steady state saltation, in which an equilibrium occurs between wind flow and transport. For the case with $U_\infty = 9.6\ m/s$ and $\alpha_{NE} = 20\%$, this constant flux was not observed due to the greater efficiency of the pavement for higher velocities and the larger amount of non-erodible particles in the particle size distribution. Indeed, for $\alpha_{NE} = 10\%$, the pavement was not evident for the lower velocity 6.7 m/s. However, for $\alpha_{NE} = 20\%$ the phenomenon was clearly seen for all tested velocities.

The temporal mass flow rate decay (after the constant flux) was fitted as an exponential function as:

$$\dot{e} = \begin{cases} \dot{e_0}, & \text{if } t < t_0 \,, \\ \dot{e_0} e^{-(t-t_0)/k}, & \text{if } t > t_0 \,, \end{cases} \tag{22}$$

where the coefficients $\dot{e_0}$ and k were determined by means of the least square method and are presented in Table 2.

It can be noticed in Figure 8 and Table 2 that the parameter k decreases with the increase of the velocity and α_{NE}. The smaller is k, the faster is the temporal decrease of the emitted mass flux. The coefficient k can be seen as

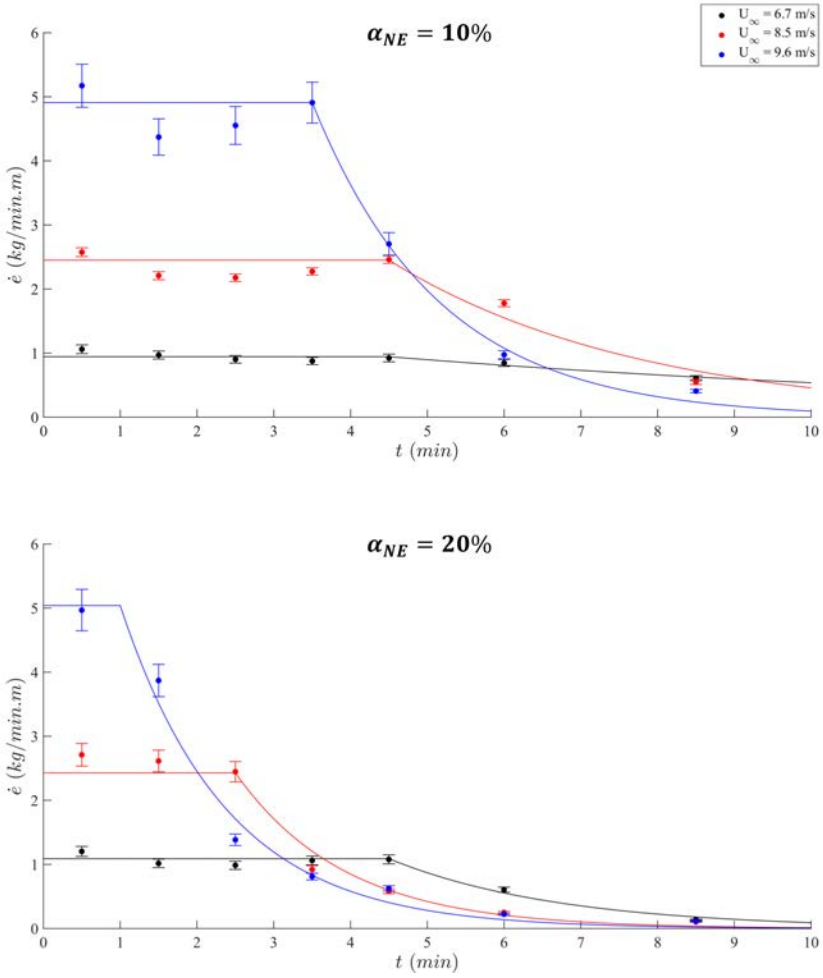

Figure 8: Temporal evolution of the emitted mass flux for non-erodible mass fractions of 10 and 20%

a characteristic time of decay, which will be shorter if the cover rate or the velocity is increased.

Figure 9 presents the temporal evolution of the eroded depths of the sand bed obtained by laser measurements for two different cases. Notice that the erosion process is observed in the last part of the bed (between 5.50 $m < x < 5.82\ m$). Figure 9(a) shows a sharp drop in the eroded depth (H) at 4 minutes and the pavement after 5 minutes. Figure 9(b) shows

Table 2: Parameters $\dot{e_0}$ and k found fitting experimental results of the temporal decrease in the emitted mass flux to an exponential function given by $\dot{e} = \dot{e_0} e^{-(t-t_0)/k}$

α_{NE}	10%			20%		
$V\ (m/s)$	6.7	8.5	9.6	6.7	8.5	9.6
t_0	4.5	4.5	3.5	4.5	2.5	1.0
$\dot{e_0}$	0.94	2.45	4.90	1.09	2.43	5.04
k	9.77	3.28	1.67	2.22	1.43	1.39

similar behaviour but at different times. The same behaviour was observed in all tested cases, more or less sharply depending on the velocity and on α_{NE}. These results enable a comprehension of how pavement occurs and are consistent with the results shown in Figure 8. During the first minutes of the experiment, there were emissions along the whole tunnel. The eroded depth in the test section did not have significant changes since depositions also occurred. As the pavement phenomenon develops, initially at the beginning of the tunnel, emissions from the earlier portions decrease, tending to zero. At these moments, there would be no more deposition in the test section. Therefore, there is a sudden drop in the eroded depth, which corresponds to the stage when the pavement occurs at the part of the sand bed located in the test section (close to the end of the tunnel). As a consequence of the spatial differences on the temporal evolution of the eroded depth, it is difficult to estimate the emission rate using Equation 20, considering that there are laser measurements of a small part of the bed (320 mm, in the test section). Nonetheless, assuming that the final eroded depth is spatially constant, the emitted mass E_f can be estimated from laser measurements. Table 3 shows the experimental results of H_f and the results of E_f obtained from H_f measurements and by weighing. The different procedures provide close values of E_f, demonstrating good measurement accuracy.

4.2. Final state of the particles bed after the pavement phenomenon

Figure 10 presents pictures of the sand bed before and after the pavement for the simulated case with $U_\infty = 8.5\ m/s$ and $\alpha_{NE} = 20\%$. Digital analysis of these photographs provided data of final cover rates. The results are presented in Table 4.

Previous authors such as Descamps et al. [10] have assumed that erosion ceases when the bed reaches a final cover rate independently of velocity and α_{NE}. However, the results presented in Table 4 show that CR_f varies

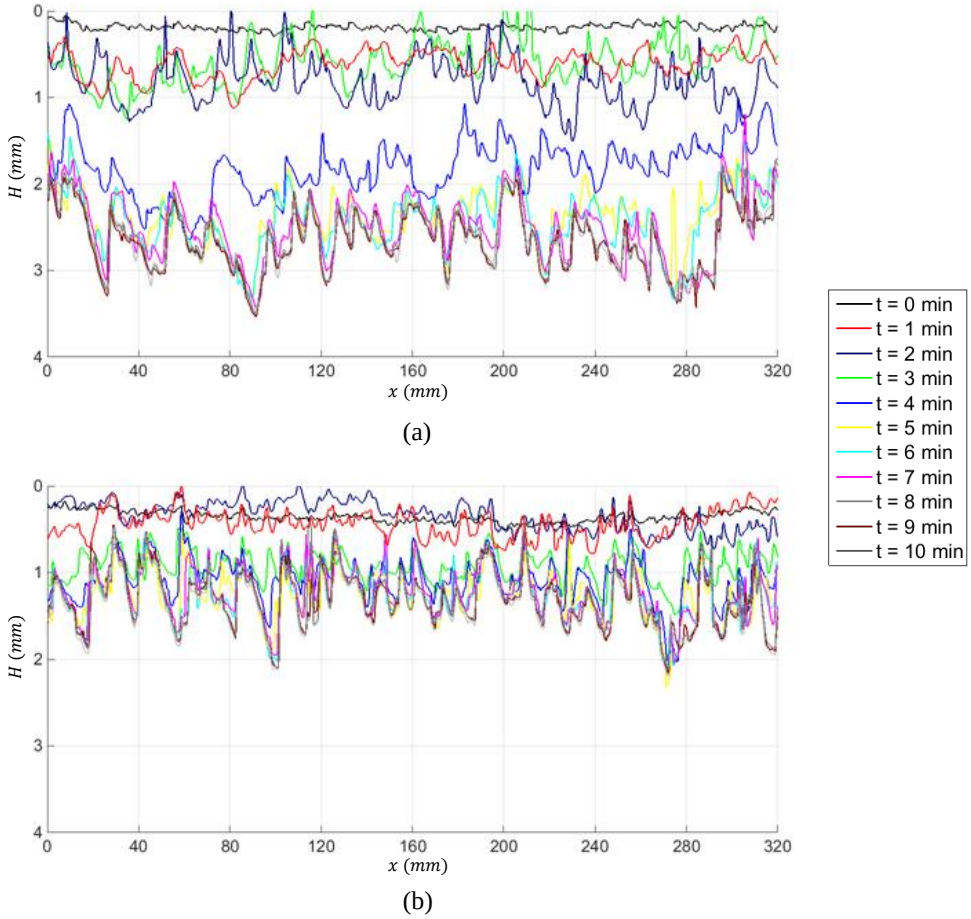

Figure 9: Temporal evolution of the eroded depths for two different cases: (a) $U_\infty = 9.6$ m/s with $\alpha_{NE} = 10\%$ and (b) $U_\infty = 8.5$ m/s with $\alpha_{NE} = 20\%$

.

with α_{NE}. In addition, the final cover rates and eroded depths of the sand bed increase with velocity, as greater velocities cause more emissions and consequently greater accumulation of non-erodible particles.

For $\alpha_{NE} = 10\%$, the values of CR_f were lower than those found for $\alpha_{NE} = 20\%$. Nonetheless, the eroded depths are greater for $\alpha_{NE} = 10\%$. These results support the fact that the protective role of the non-erodible particles is not only given by the cover rate of the sand bed but also by the

Table 3: Final eroded depths of the sand bed determined by laser methodology and estimated emitted mass obtained by H_f measurements and by weighing

$\alpha_{NE}(\%)$	$U_\infty(m/s)$	$H_f(mm)$	$E_f(g)$ (from H_f)	$E_f(g)$ (weighing)
10	6.7	1.03	2401.3	2393.3
	8.5	1.75	4074.8	4140.9
	9.6	2.5	5821.2	6095.2
20	6.7	0.88	1821.4	1719.0
	8.5	1.19	2461.0	2505.7
	9.6	1.34	2773.5	3088.7

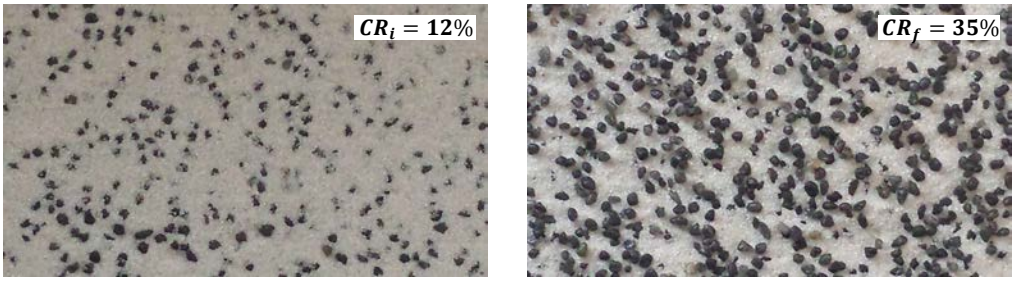

(a) (b)

Figure 10: Pictures of the sand bed (a) before and (b) after the pavement for $U_\infty = 8.5$ m/s with $\alpha_{NE} = 20\%$

height of the non-erodible elements (see Equation 6).

Table 4: Initial and final cover rates determined by digital analysis of photographs of the experiment and final eroded depths of the sand bed as determined by laser methodology

$\alpha_{NE}(\%)$	$CR_i(\%)$	$U_\infty(m/s)$	$CR_f(\%)$	$H_f(mm)$
10	6.4	6.7	17	1.03
		8.5	23	1.75
		9.6	30	2.50
20	11.8	6.7	29	0.88
		8.5	35	1.19
		9.6	38	1.34

Figure 11 shows the ratio between CR_f and CR_i for each tested case. It can be seen that despite the lower values of CR_f for $\alpha_{NE} = 10\%$, the increase in cover rate was proportionally more steep. Moreover, the airflow velocity

has more influence on the cover rate variation for the case with $\alpha_{NE} = 10\%$.

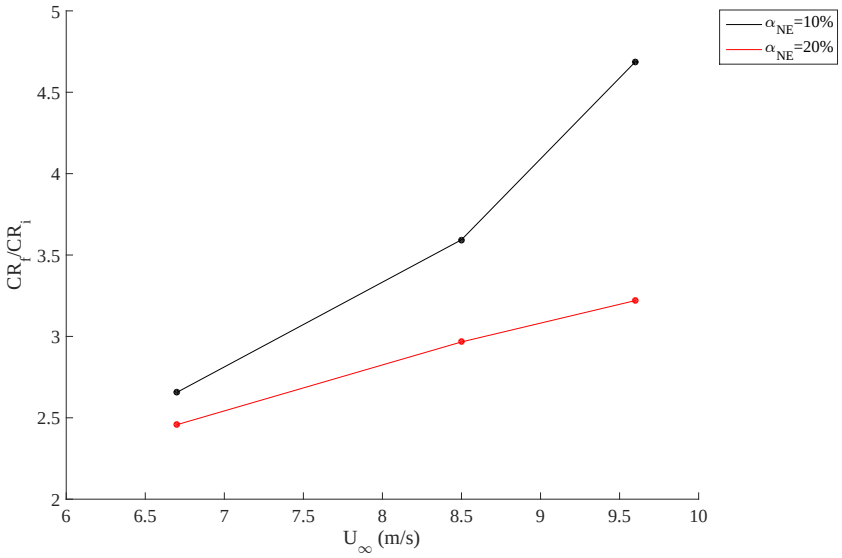

Figure 11: Variation of the cover rate for each tested configuration

5. Comparisons between model predictions and experiments

As explained in Section 2.3, the emitted mass is estimated by following three steps. (i) First, knowing the initial particle size distribution, the cover rate CR is written as a function of the eroded depth H (Equation 16). Figure 12 presents CR/CR_i as a function of H obtained using Equation 16 (solid line) and the experimental data, which is the final state of the bed (H_f and CR_f/CR_i) for each tested case (points). The formulation given by Equation 16 is well supported by the experiments. (ii) Then, Equation 16 enables the calculation of the final eroded depth after the pavement phenomenon for a given velocity using Equation 18 (in the experimental configuration, $u^*_{MIN} = u^*_{t_d}(200\mu m) \approx 0.18\ m/s$). It is important to state that both equations produce differences between the modelled and experimental results. As a consequence, the propagated error of the final eroded depth leads to a variation in the emission estimation. (iii) Finally, emission is calculated using Equation 19.

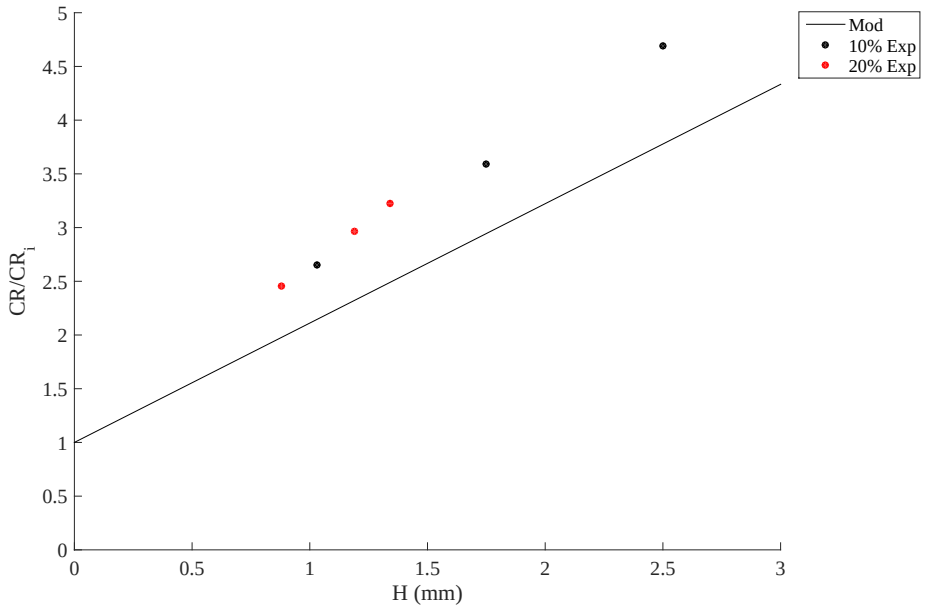

Figure 12: Cover rate of non-erodible particles as a function of eroded depth obtained by modelling (Equation 16) and the values of H_f and CR_f/CR_i obtained experimentally (Table 4)

Table 5 compares the estimated results of the final eroded depth and the emitted mass with experimental data, including percentage errors. There is good agreement between the modelled and the experimental results for both measurements. The uncertainty of emission measurements, retrieved by previous repeatability tests with similar wind tunnel experiments, was found to be in the range of ±6.5%. Thus, the modelled results slightly underestimate the experimental data.

The proposed model is a continuation of the work described in Descamps et al. [10]. A limitation of the previous model is the assumption that erosion is finalised when the bed is completely overlaid by non-erodible particles. As explained in Section 4.2, it has already been verified that erosion is terminated with a lower cover rate of the surface. Another limitation of the previous Descamps et al. [10] model is related to the fact that the influence of saltation on transport is not accounted for. These two points have been adjusted in [4], but with a purely stochastic method that produces very large calculation times. On the other hand, the previous model has the advantage

Table 5: Comparison of experimental and model results

α_{NE}	U_∞ (m/s)	H_f (mm)			Emitted mass (g)		
		Exp.	Mod.	Error	Exp.	Mod.	Error
10%	6.7	1.03	0.98	4.9%	2393.3	2345.1	2.0%
	8.5	1.75	1.73	1.1%	4140.9	3802.9	8.2%
	9.6	2.50	2.23	10.8%	6095.2	5231.8	14.2%
20%	6.7	0.88	0.50	43.2%	1719.0	1049.5	38.9%
	8.5	1.19	0.99	16.8%	2505.7	2092.5	16.5%
	9.6	1.34	1.26	6.0%	3088.7	2637.3	14.6%

of providing detailed information concerning the temporal decrease of the emitted mass flux, although in practical cases such as fugitive sources on industrial sites, the most important information is the total emitted mass. Furthermore, the absolute value of the emitted mass is largely underestimated by the Descamps et al. [10] model. The present study focused on modelling the final state of the bed after the pavement phenomenon and provides estimates of the global emissions, which are in good agreement with the experimental results. Moreover, it has the advantage of being represented by a simple mathematical expression.

6. Conclusion

This work investigated the pavement phenomenon and how it affects particle emissions from a bed of granular material exposed to a turbulent flow using experimental and analytical approaches.

The temporal evolution of the emitted mass flux revealed that during the first minutes, flux remained nearly constant, indicating that an equilibrium was established between wind flow and transport. The equilibrium state lasted longer for the lower velocities and for the beds with a lower proportion of non-erodible particles. After a few minutes, the flux began to decrease due to the pavement phenomenon. This decay was faster for higher velocities. In addition, greater amounts of non-erodible particles in the mixture led to a greater decay rate. These findings are consistent with previous studies in the literature [4, 5].

A mathematical model for emitted mass estimates that includes the influence of the presence of non-erodible particles and saltation was proposed. The influence of saltation was included in the modelling using the dynamic

threshold. The proportion of non-erodible particles on a bed surface after the pavement phenomenon was quantified. Although previous authors (e.g., Descamps [4], Furieri et al. [5]) have observed this phenomenon, it had not yet been quantified. Good agreement was found between the experimental and model results for the global emissions and bed eroded depth. Although the theory on which the proposed model is based is quite complex, the model is represented by a simple algebraic expression and demands low computational effort. Further work is still needed to improve the model for application to stockpiles of granular materials.

Acknowledgements

The authors acknowledge support from Capes/Cofecub, Fapes and CNPq.

References

[1] L. Lyles, R. L. Schrandt, N. F. Schmeidler, How aerodynamic roughness elements control sand movement, TRANSACTIONS of the ASAE 17 (1) (1976) 134–139.

[2] L. Li, L. Martz, Aerodynamic dislodgement of multiple-size sand grains over time, Sedimentology 42 (4) (1995) 683–694.

[3] L. Liu, P. Shi, X. Zou, S. Gao, H. Erdon, P. Yan, X. Li, Z. Dong, J. Wang, Short-term dynamics of wind erosion of three newly cultivated grassland soils in Northern China, Geoderma 115 (12) (2003) 55 – 64.

[4] I. Descamps, Erosion éolienne d'un lit de particules large spectre granulométrique. Wind erosion of a bed of particles with a wide size distribution, Phd thesis, Ecole des Mines de Douai, Université de Valenciennes et du Hainaut-Cambrésis, 2004.

[5] B. Furieri, S. Russeil, J. M. Santos, J.-L. Harion, Effects of non-erodible particles on aeolian erosion: Wind-tunnel simulations of a sand oblong storage pile, Atmospheric Environment 79 (0) (2013) 672 – 680.

[6] W. Nickling, C. McKenna Neuman, Aeolian sediment transport, in: A. Parsons, A. Abrahams (Eds.), Geomorphology of Desert Environments, Springer, 517–555, 2009.

[7] B. Marticorena, G. Bergametti, Modeling the atmospheric dust cycle: 1. Design of a soil-derived dust emission scheme, Journal of Geophysical Research: Atmospheres 100 (D8) (1995) 16415–16430.

[8] S. C. Alfaro, L. Gomes, J. L. Rajot, A. Gaudichet, Modeling mineral aerosol production by wind erosion: Part 1. Physical bases., Journal of aerosol science 31 (2000) 426–427.

[9] J. Kok, N. Renno, A comprehensive numerical model of steady state saltation (COMSALT), Journal of Geophysical Research: Atmospheres 114 (D17), ISSN 2156-2202.

[10] I. Descamps, J.-L. Harion, B. Baudoin, Taking-off model of particles with a wide size distribution, Chemical Engineering and Processing: Process Intensification 44 (2) (2005) 159–166.

[11] D. Gillette, P. Stockton, The effect of nonerodible particles on wind erosion of erodible surfaces, Journal of Geophysical Research: Atmospheres 94 (D10) (1989) 12885–12893.

[12] J. Iversen, W. Wang, K. Rasmussen, H. Mikkelsen, R. Leach, Roughness element effect on local and universal saltation transport, in: O. Barndorff-Nielsen, B. Willetts (Eds.), Aeolian Grain Transport, vol. 2 of *Acta Mechanica Supplementum*, Springer Vienna, 65–75, 1991.

[13] M. Raupach, D. Gillette, J. Leys, The effect of roughness elements on wind erosion threshold, Journal of Geophysical Research: Atmospheres 98 (D2) (1993) 3023–3029.

[14] R. Bagnold, The physics of blown sand and desert dunes, vol. 265, Methuen, London, reprint edn., 1941.

[15] J. Iversen, B. White, Saltation threshold on Earth, Mars and Venus, Sedimentology 29 (1) (1982) 111–119.

[16] J.-M. Foucaut, M. Stanislas, Take-off threshold velocity of solid particles lying under a turbulent boundary layer, Experiments in Fluids 20 (5) (1996) 377–382.

[17] O. Durán, P. Claudin, B. Andreotti, On aeolian transport: Grain-scale interactions, dynamical mechanisms and scaling laws, Aeolian Research 3 (3) (2011) 243 – 270.

[18] S. Duan, N. Cheng, L. Xie, A new statistical model for threshold friction velocity of sand particle motion, CATENA 104 (0) (2013) 32 – 38.

[19] Y. Shao, H. Lu, A simple expression for wind erosion threshold friction velocity, Journal of Geophysical Research: Atmospheres 105 (D17) (2000) 22437–22443.

[20] J. Kok, E. Parteli, T. Michaels, D. Karam, The physics of wind-blown sand and dust, Reports on Progress in Physics 75 (10) (2012) 106901.

[21] J. Kok, N. Renno, Enhancement of the emission of mineral dust aerosols by electric forces, Geophysical research letters 33 (19).

[22] W. S. Chepil, Dynamics of wind erosion: II. Initiation of soil movement, Soil Science 60 (1945) 397–411.

[23] J. D. Iversen, K. R. Rasmussen, The effect of surface slope on saltation threshold, Sedimentology 41 (4) (1994) 721–728.

[24] M. Raupach, Drag and drag partition on rough surfaces, Boundary-Layer Meteorology 60 (4) (1992) 375–395.

[25] J. Marshall, Drag measurements in roughness arrays of varying density and distribution, Agricultural Meteorology 8 (0) (1971) 269–292.

[26] D. Crawley, W. Nickling, Drag Partition for Regularly-Arrayed Rough Surfaces, Boundary-Layer Meteorology 107 (2) (2003) 445–468.

[27] H. Schlichting, Experimentelle Untersuchungen zum Rauhigkeitsproblem, Ingenieur-Archiv 7 (1) (1936) 1–34.

[28] C. Turpin, T. Badr, J.-L. Harion, Numerical modelling of aeolian erosion over rough surfaces, Earth Surface Processes and Landforms 35 (12) (2010) 1418–1429.

[29] B. Furieri, J.-L. Harion, M. Milliez, S. Russeil, J. M. Santos, Numerical modelling of aeolian erosion over a surface with non-uniformly distributed roughness elements, Earth Surface Processes and Landforms 39 (2) (2013) 156–166.

[30] T. Ho, A. Valance, P. Dupont, A. Ould El Moctar, Aeolian sand transport: Length and height distributions of saltation trajectories, Aeolian Research 12 (2014) 65–74.

Chapter 3

Aeolian erosion over oblong stockpiles

The focus of this section is on particles emission quantification due to wind erosion of stockpiles. Sections 3.1 and 3.2 investigate the impact of the presence of multiple piles and buildings on wind erosion, respectively. In Section 3.3, the improvements on the emission model to extend the application for granular materials stockpiles are presented.

3.1 Experimental and numerical study of aeolian erosion of isolated and successive piles

This section is presented as an article entitled "Experimental and numerical study of aeolian erosion of isolated and successive piles" intended to be submitted to the "Journal of Wind Engineering & Industrial Aerodynamics". The paper analyses the impact of successive parallel stockpiles arrangements on the flow behaviour and consequently on global emissions due to aeolian erosion. Wind tunnel experiments and numerical simulations were carried out for several configurations evaluating the effects of: (i) main wind flow orientation, (ii) wind flow velocity, (iii) gap between piles in tandem and staggered arrangements and (iv) amount of non-erodible particles.

An experimental and numerical study of the aeolian erosion of isolated and successive piles

M.C. Caliman[a,b], B. Furieri[a,b], J.M. Santos[a], A. Ould El Moctar[c], J.-L. Harion[d], A. Valance[e], P. Dupont[f], N.C. Reis Jr[a]

[a] *Universidade Federal do Espírito Santo, DEA, 29060-970 Vitória, ES, Brazil*
[b] *Instituto Federal do Espírito Santo, 29056-255 Vitória, ES, Brazil*
[c] *Polytech. Nantes, Laboratoire de Thermocinétique, F-44306 Nantes, France*
[d] *Mines Douai, EI, F-59500 Douai, France*
[e] *Universit de Rennes 1, Institut de Physique, F-35042 Rennes, France*
[f] *INSA de Rennes, LGCGM, F-35043 Rennes, France*

Abstract

Open storage yards at industrial sites usually comprise several piles of granular materials, representing a particulate matter source that can significantly deteriorate air quality. The aeolian erosion of such stockpiles is affected by changes in airflow patterns due to the pile shape and the presence of nearby piles or buildings. The aim of this study was to analyse the impact of the wind erosion of successive parallel stockpiles on flow behaviour and particle emissions. A wind tunnel experiment was conducted in six configurations: one isolated pile and two successive piles separated by gaps of $0.9h$ and $1.8h$ (h is the pile height) oriented to 60° and 90° with respect to the main wind flow direction. The particles in the piles had a bimodal granulometry consisting of sand that was erodible (white) and non-erodible (black) in the investigated velocity range. The contrasting colours enabled the visualisation of the non-erodible sand accumulation. The mean field of the wall shear stress distribution and flow pathlines predicted by numerical simulation were associated with the experimental erosion patterns. In addition to the erosion patterns, the mass emitted was experimentally quantified as the difference between the initial and final stockpile weights. It was found that the downstream pile had a large impact on the aeolian erosion, which would lead to an increase in total emissions. The downstream stockpile was highly eroded as a result of the impact of the particles emitted from the upstream pile. The emissions of the two consecutive stockpiles were greater than twice the emissions from an isolated stockpile for both orientations. Additionally,

Preprint submitted to Journal of Wind Engineering and Industrial Aerodynamics, 25th April 2017

emissions were lower for configurations in which the piles were perpendicular to the primary incoming wind direction.

Keywords: wind erosion, pavement, fugitive emissions, flow around stockpiles, wind tunnel, emission measurements

1. Introduction

Diffuse emission from the aeolian erosion of granular materials from stockpiles or exposed granular beds may be difficult to quantify due to the large extension and shapes of the sources and the factors that affect the process such as atmospheric conditions (e.g., wind velocity and direction, precipitation, humidity and temperature), particle granulometry distribution, modification of the wind flow due to the presence of obstacles and topography (e.g., flat or inclined surfaces). Granular materials typically have a wide particle size distribution, including larger grains that may not be lifted by wind. As erosion occurs, the concentration of the coarser particles on the pile surface increases. It has been verified that the accumulation of these grains plays a protective role in particle emissions, whether on a flat or an inclined surface [1, 2]. Non-erodible particles create wake zones, reducing the drag on pile zones that would otherwise be erodible. A temporal decrease thereby occurs for the emitted mass flux, and the total amount of particles emitted due to wind erosion is strongly reduced, which is known as the pavement phenomenon.

The most widely used methodology to estimate fugitive dust emissions has been developed by the USEPA (United States Environmental Protection Agency) [3], based on data from wind tunnel experiments for two geometries of isolated stockpiles and three wind flow directions, and does not consider the pavement phenomenon. The rapid decrease in aeolian emissions linked to a wide size distribution is mentioned in [3], but it is not explicitly incorporated in the proposed method. The particle size distribution is also not explicitly incorporated into the method so that if the model was applied to two granular materials with very different particle size distributions but the same maximum particle diameter, it would result in similar emission values. Experimental results show that wind erosion emissions can be widely different with the same maximum particle diameter but a greater proportion of larger particles. Furthermore, the various configurations of different piles shapes that can be found at industrial sites are not covered by the elements

provided by the USEPA in [3]. Industrial facilities usually contain more than one storage pile, which greatly affects erosion patterns since piles act as obstacles to the free path of atmospheric flow, modifying the flow field dynamics.

Several researchers have used a Computation Fluid Dynamics (CFD) approach to broaden the models application to other realistic situations [4, 5, 6]. Badr and Harion [7] and Toraño et al. [8] numerically predicted the wind flow over isolated piles in different scenarios with various geometries and wind orientations and used the USEPA formulation for the emission factor to quantify particle emissions using the friction velocity previously calculated by CFD. Turpin and Harion [9] investigated the flow structures over coal stockpiles in an actual power plant configuration. The authors performed numerical simulations in a configuration that included three coal stockpiles and different buildings in the surrounding area, and found that upstream buildings significantly increased emissions from the piles. Nevertheless, if the stockpile was located upstream of the buildings in the configurations tested by Turpin and Harion [9], then the erosion processes was slightly attenuated by a flow stagnation zone upstream of the buildings. The authors concluded that all wind perturbations including surrounding buildings and stockpiles have an impact, and must be accounted for in dust emissions estimation. Diego et al. [10] and Cong et al. [11] employed similar techniques to estimate dust emissions by integrating CFD data into the USEPA methodology. The former work studied the wind flow around an arrangement of two parallel flat-crested stockpiles separated by a gap of $0.44h$ (where h is the height of the piles) and highlighted the different contribution from each pile to the total eroded dust. The latter work evaluated dust emissions in an open yard with a complex geometry (16 stockpiles arranged in 4 columns) varying the pile shape (flat-topped oval and conical), the gap between the piles ($0.6h$ and $1.2h$) and the orientation of the wind direction (from 0 to 90°). In both studies, a sheltering effect created by the neighbouring piles was noticed, which resulted in lower dust emissions. It is found that the front pile created a downstream shelter, then the wind speed over the back pile was reduced. However, Cong et al. [11] verified that the total dust emissions are greater when the gaps between piles are larger. The authors implied that a gap larger than the shelter area completely exposes the downstream piles to wind erosion, similar to an isolated pile. In addition, it has been suggested that more studies with arbitrary space variation between the piles are necessary to better understand the role of the stockpile layout in limiting wind erosion in an actual yard. Furieri

et al. [12] compared emissions from an isolated and two successive oblong stockpiles separated by $0.9h$ and $1.8h$ gaps oriented by 60° to the main wind flow direction. Numerical results showed that an isolated stockpile emitted less dust than each pile in the successive pile configuration. Therefore, a protective role of the upstream pile was not observed. Ferreira and Fino [13] performed wind tunnel experiments to study the erosion of an isolated sinusoidal pile and the interference effect resulting from two closely spaced piles (gaps of 0 and h). The authors found that the aeolian erosion of the downstream pile was considerably larger due to flow disturbances induced by the first pile. Therefore, the literature is contradictory, and the wind erosion of two parallel piles still requires additional investigation.

This study aimed to investigate the impact of several configurations of parallel piles on wind erosion and the effect on emissions of the proportion of non-erodible particles. The parameters analysed were (i) wind velocity, (ii) the orientation of the piles to the main flow direction and (iii) the gap distance between the piles. A wind tunnel experiment was performed to estimate and compare emissions from an isolated sand pile and from two successive piles. The particles that constituted the piles had bimodal granulometry encompassing erodible and non-erodible particles in two different proportions. The accumulation of non-erodible particles enabled an analysis of the erosion patterns of the piles. Numerical simulations with identical configurations were carried out to obtain the wall shear stress distribution on the pile surface and the flow pathlines, which support our understanding of the physical phenomena.

2. Experimental study

The experiment was conducted in the wind tunnel facilities at the Département Energétique Industrielle (Douai, France). Figure 1 shows the experimental set-up and the principal dimensions of the wind tunnel. Multiple roughness obstacles were placed in rows close to the tunnel entrance to enable the formation of a turbulent boundary layer. The validation of the experimental profiles upstream the test section is based on the comparison between measured profiles of velocity and turbulent kinetic energy (carried out in the same wind tunnel by Turpin [14]) and the profiles of fully developed turbulent boundary layer from the literature [15]. In the vicinity of the wall, the velocity profile follows the linear law and then, moving away from the wall, follows the logarithmic law. The wind-tunnel generates a fully developed

turbulent boundary layer at the level of the measurement zone with a thickness greater than the stockpile height ($\delta = 16\ cm > h = 7.7\ cm$). More details of the wind-tunnel characteristics are given by Furieri et al. [16] and Turpin [14]. The Reynolds number of the fluid flow inside the wind-tunnel is approximately between 36000 and 48000 based on the free stream velocity (from 6 to 8 m/s) and stockpile height.

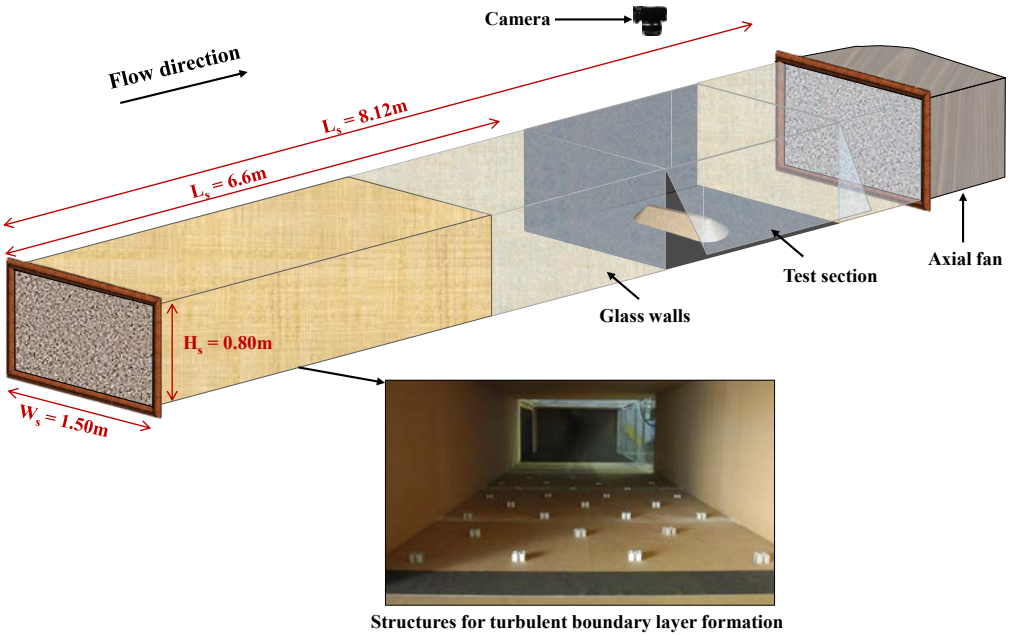

Figure 1: Wind tunnel scheme

A bimodal granulometry of sand with density equal to 2650 kg/m^3 was used to represent erodible and non-erodible particles: fine white sand and coarse black sand with ranges of diameters from 56.0 to 194.2 μm and from 700.0 to 1300.0 μm, respectively. The sand colours allowed the visualisation of high shear stress zones, which were marked by the accumulation of non-erodible particles.

The threshold friction velocities $u^*_{t\,min}$ and $u^*_{t\,max}$ at which the largest erodible particles (194.2 μm) and the smallest non-erodible particles (700.0 μm), respectively, are lifted from a horizontal surface were calculated using the take-off criterion obtained by Shao and Lu [17]:

$$u_{t_s}^* = 0.11\sqrt{\frac{\rho_P - \rho}{\rho} gD + \frac{\gamma}{\rho D}}\,, \tag{1}$$

where $u_{t_s}^*$ is the threshold friction velocity, ρ is the fluid density, ρ_P is the particle density, g is the gravity, D is the particle diameter and γ is a surface energy that characterises the cohesion. Shao and Lu [17] recommended values of γ ranging between 1.65×10^{-4} and 5.00×10^{-4} kg/s^2. In the present work, $\gamma = 2.86 \times 10^{-4}$ kg/s^2 was adopted. This value was calculated by fitting Equation 1 to the experimental threshold required to lift loose particles as proposed by Kok and Renno [18].

Figure 2 shows the take off-criterion, the fine and coarse sand size ranges used for the experiments and the friction velocities $u_{t\,min}^* = 0.23$ and $u_{t\,max}^* = 0.42$. The corresponding freestream flow velocities U_{min} and U_{max}, determined based on u_{min}^* and u_{max}^*, were calculated using the expression proposed by Kurose and Komori [19]:

$$u^* = u_{smooth}^*(1 + 0.00431h^+)\,, \tag{2}$$

where h^+ is the dimensionless mean diameter of the non-erodible particles ($h^+ = h_{NEP}u_s^*/\nu$, where h_{NEP} is the mean diameter of the non-erodible particles, and ν is the kinematic viscosity), and u_{smooth}^* is the friction velocity in a smooth wall, which is calculated by the relation proposed by Mollinger and Nieuwstadt [20]:

$$u_{smooth}^* = 0.036U_\infty + 0.033\,. \tag{3}$$

Therefore, Equations 2 and 3 yielded $U_{min} = 5.5$ m/s and $U_{max} = 9.5$ m/s. Three different velocities were experimentally tested: 6, 7 and 8 m/s. These velocities were between U_{min} and U_{max}, the minimum and maximum velocities at which the finer and the coarse particles remained erodible and non-erodible, respectively, for a horizontal surface. However, the threshold friction velocity $u_{t_s}^*(\theta)$ on a surface with a slope $\tan\theta$ is different from that found in a flat bed due to the distinct relative contributions of the forces acting on the particle. If the slope is positive (flow upwards), gravity is a resistive force, and thus, the friction velocity must be stronger to lift the

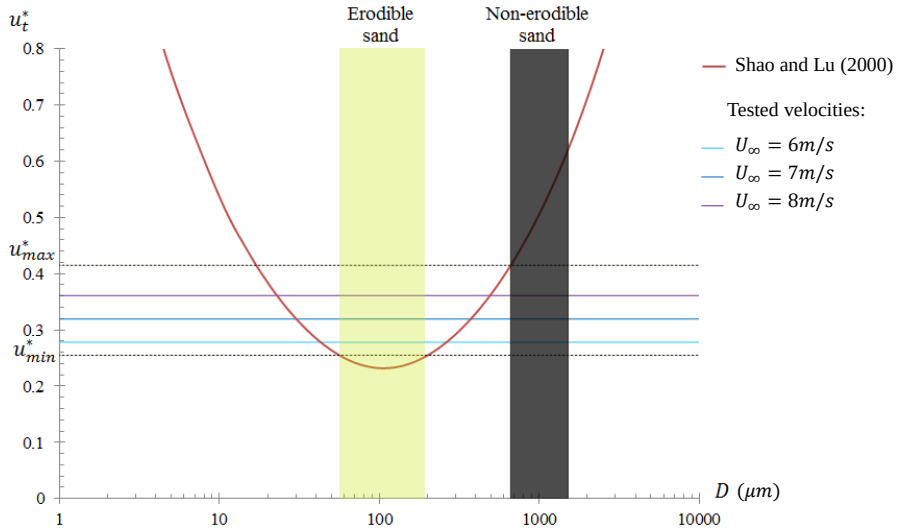

Figure 2: Take-off criterion for a horizontal surface

grains. In contrast, if the slope is negative (flow downwards), the friction velocity required to lift the particles is lower than the threshold friction velocity for the beds.

The sand stockpile models were formed inside the wind-tunnel using a device similar to an industrial hopper, shown in Figure 3(a). Furieri et al. [2] have performed several tests to ensure that the pile shape and dimensions given by this device were reproducible. The dimensions of the sand stockpile had a scale ratio of approximately 1:200 to an actual stockpile, and they are shown in Figures 3(b) and 3(c): 7.7 cm (height), 23.6 cm (length), 57.9 cm (width), and 34.5° of angle of repose. It must be mentioned that the experiments did not accurately simulate full-scale conditions because the pile dimensions were smaller than the saturation length, the length that transport requires for saturation (i.e., to reach the saturated flux), which is approximately 1 to 2 m [21]. Therefore, the experimental sand piles did not behave in a similar way to piles of scale several metres from the erosion point of view: the first would be primarily eroded by aerodynamic entrainment, while the second would be subject to impact entrainment.

Configurations of one isolated stockpile and two successive stockpiles were used in the wind tunnel experiments. For the two pile configuration, the edge-to-edge separations tested were $0.9h$ and $1.8h$, where h is the height

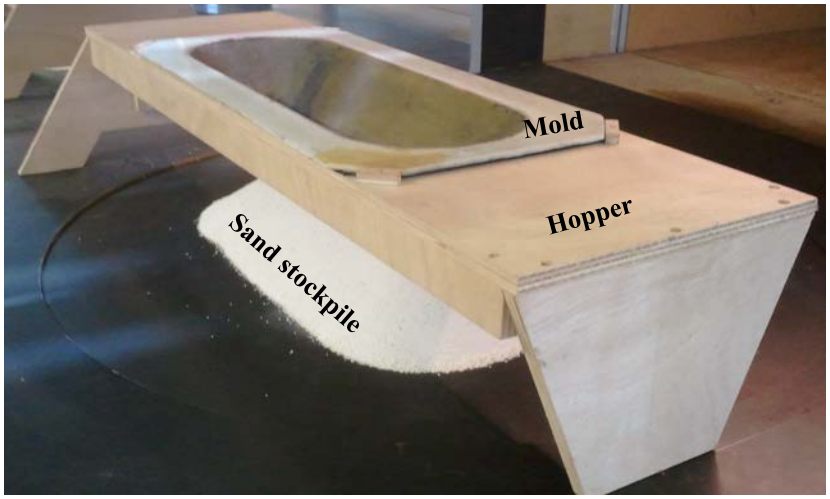

(a)

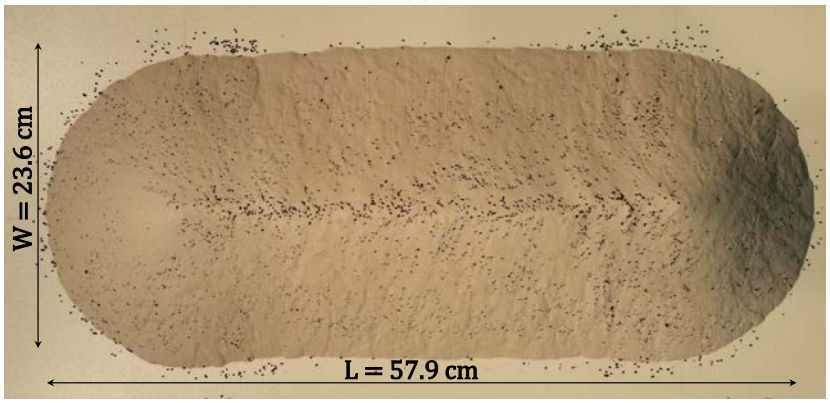

(b)

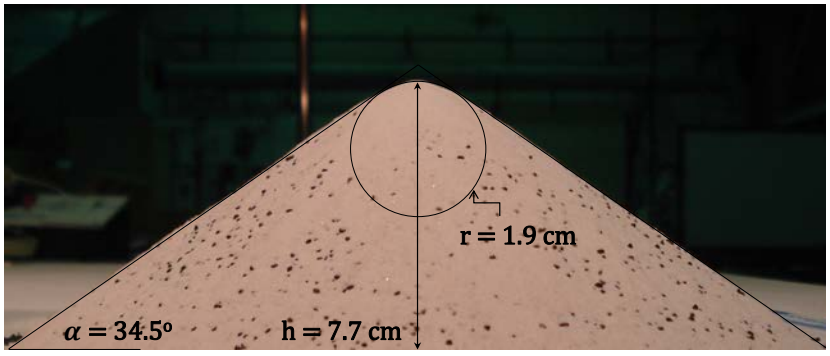

(c)

Figure 3: (a) Device used for the construction of the sand stockpile model and the mean dimensions of the sand stockpile in (b) Top and (c) Side views

of the pile. The effect of the stockpile orientation to the main wind flow direction was analysed for 60° and 90°. The piles were built with a mixture of the erodible and non-erodible sand with two different mass fractions of non-erodible particles (α_{NE}): 10 and 20%. The six pile configurations used in the 36 tests are shown in Table 1.

Table 1: Tested configurations. The pile dimensions are: 7.7 cm of height, 23.6 cm of length and 57.9 cm of width

Configuration	Velocity (m/s)	Gap	α_{NE}
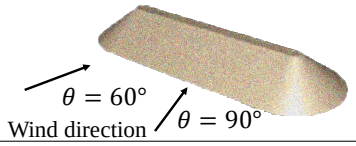	6, 7, 8	-	10%, 20%
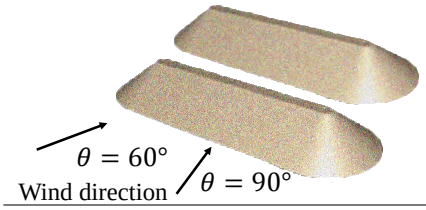	6, 7, 8	$0.9h$, $1.8h$	10%, 20%

After determining the initial stockpile mass and setting it on the wind tunnel floor, the free stream velocity was set by a frequency controller, and the fan was turned on. The duration of the flow was 15 minutes in all cases. No additional emissions occurred after this period, and a progressive pavement process that finally suppressed erosion at the eroded areas was observed. A camera installed over the wind-tunnel ceiling (transparent glass wall) registered the erosion evolution by analysing the contrasting colours (black and white sand). The photographs were taken at the beginning of the experiment and every 30 seconds for 5 minutes. The last picture was taken after 15 minutes. These pictures allowed for a qualitative assessment of the temporal evolution of different wind erosion exposure zones on the pile.

For the two parallel pile configuration, each pile was weighed separately after the experiment. The mass of particles emitted was calculated as the difference between the initial and final stockpile weights.

The repeatability of the experimental measurements was tested using the configuration with $\alpha_{NE} = 20\%$, orientation 90°, $1.8h$ gap and $U_\infty = 7\ m/s$. The emitted mass for the three different tests of repetitions had a reasonable

coefficient of variation equal to 4.5% (the coefficient of variation is defined as the ratio of the standard deviation to the mean and is given by 23.3 and 524.3 grams, respectively).

3. Numerical simulations set up

Numerical simulations were performed to solve the flow structure over several pile configurations representing the wind tunnel experiment (see Table 1). The three-dimensional Reynolds Averaged Navier-Stokes equations of mass and momentum were solved using the commercial software Fluent 15.0 [22], providing the mean fields of the flow properties. The $k-\omega$ Shear Stress Transport (SST) model was used to incorporate turbulence effects. This turbulence model was chosen based on a study performed by Badr and Harion [23], who simulated analogous configurations under similar flow conditions and compared the results using different closure models. Figure 4 presents the computational domain dimensions and boundary conditions. The inlet boundary conditions for the velocity, the turbulent kinetic energy and the specific dissipation rate were retrieved from a converged field obtained by previous numerical simulations of a channel flow with the same dimensions, for which a periodic streamwise flow was set. The inlet profiles of wind velocity and turbulence intensity of the numerical simulations were validated using the experimental data carried out by Turpin [14] in the same wind tunnel described in Section 2. A fully developed flow was assumed for the outflow conditions, that is, all flow variables except pressure were assumed to have a zero normal gradient. The SIMPLEC algorithm was used for pressure-velocity coupling [24]. Symmetry conditions were applied to the upper domain boundary (normal gradients of all variables were set to zero). Finally, no-slip conditions were imposed for the lateral boundaries, the ground and the pile surface.

The geometries and meshing were generated with Gambit software (Geometry and Mesh Building Intelligent Toolkit) [25]. The mesh was built by an extrusion of triangular face cells from the pile and ground walls towards the upper wall of the computational domain creating triangular-based prism cells (see Figure 5). The grid is irregular following the shape and orientation of the geometries. A mesh refinement near the walls ($y+ < 5$) was required due to the expected intense gradients close to these areas and due to turbulence modelling requirements. Mesh sensitivity tests were previously carried out for similar configurations [23]. Turbulence model choice was based on pre-

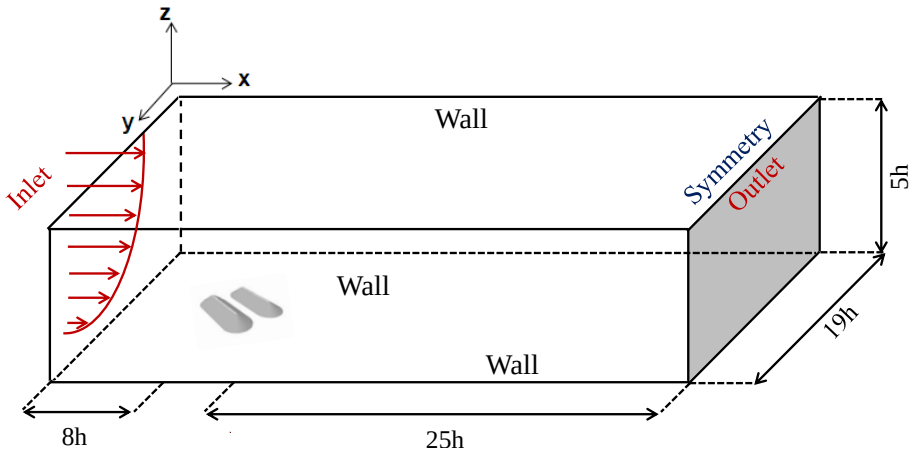

Figure 4: Computational domain

viously validated numerical calculations performed by Badr and Harion [23] and Turpin [14]. For the different configurations, the computational grids ranged from 3800000 to 5300000 cells. The simulations with two successive piles arrangement required the larger number of cells in order to allow sufficient refinement between the piles.

4. Results

The results are presented in three sections. In the first section, the erosion patterns are interpreted in the light of the numerical data of the basal shear stress map. Then, a general overview of the pavement process for a tested case is presented. Finally, the mass loss measurements for the different configurations are discussed in the third section.

4.1. Comparison between basal shear stress maps and erosion patterns

As previously mentioned, the erosion patterns were identified by the agglomeration of non-erodible (black) particles in the final experimental images, after the pavement phenomenon. The surface distribution of the black particles enabled the identification of pile zones in which the shear stress was great enough to erode fine particles (i.e., white particles) and offers support to the investigation of the effect of a second stockpile on the erosion pattern. This section mainly focuses on the experiment in which the wind erosion was

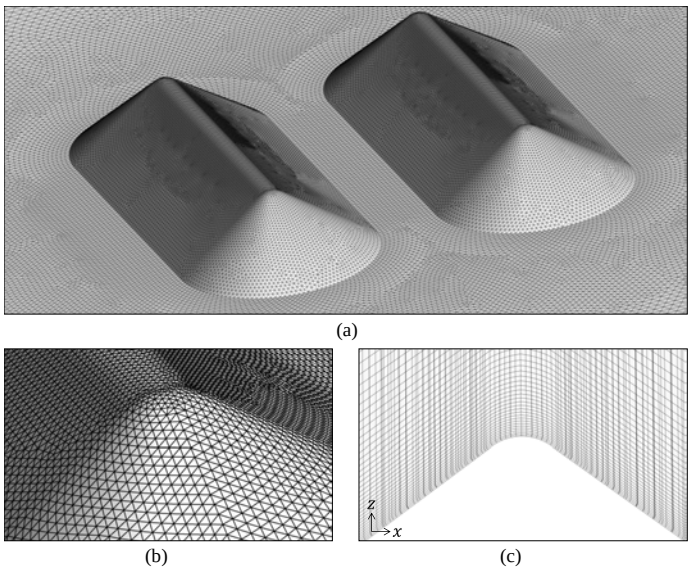

Figure 5: (a) Perspective view of the mesh over the two piles, (b) Zoom of the mesh near the crest, and (c) Transversal cut of the domain over the pile

stronger ($U_\infty = 8\ m/s$ and $\alpha_{NE} = 20\%$) to highlight the erosion patterns in different areas of the piles surface.

The numerical results are presented in dimensionless form as local shear stress values were divided by a reference shear stress value (τ_{ref}) obtained for an undisturbed zone where the flow was not affected by the stockpile. Although the shear stress increased with an increase of the wind flow velocity, the flow pattern characteristics given by τ/τ_{ref} remained quite similar for each velocity tested. Similarly, the mean fluid flow pathlines around the piles were coloured based on the ratio of the velocity to a reference free stream velocity (U_∞).

The isolated stockpile will subsequently be referred to as pile p_1, and the upstream and downstream piles in the successive arrangements will be referred to as piles p_2 and p_2', respectively. Distinctive wind erosion regions are highlighted according to the degree of wind exposure. To facilitate the analysis, 4 zones were highlighted on the isolated stockpile and are designated as A_1, B_1, C_1 and D_1, and 4 zones were highlighted on each pile for the successive configurations and are designated as A_2, B_2, C_2 and D_2 in pile p_2 and A_2', B_2', C_2' and D_2' in pile p_2'.

4.1.1. Stockpiles oriented perpendicularly to the main wind flow direction

Figures 6 and 7 show the photographs taken after the pavement phenomenon, the mean wall shear stress distribution and pathlines, respectively, for an isolated stockpile and two stockpiles oriented 90° to the main flow direction (separated by gaps of $0.9h$ and $1.8h$).

Figure 6(a) shows that no erosion occurred in the stagnation zone A_1. Indeed, this zone was characterised by intense deceleration and wall shear stress levels near zero (see Figures 6(b) and 6(c)). The incident flow was progressively accelerated towards the crest and the lateral sides of the pile forming region B_1, where the highest levels of shear occurred due to a strong velocity gradient (Figures 6(b) and 6(c)). Therefore, these areas were the most vulnerable to wind erosion, which explains the accumulation of non-erodible black particles seen in Figure 6(a).

Figure 6(c) shows the flow separation from the pile surface on the crest and the lateral sides, as a result of a strong adverse pressure gradient. The separation led to a wake region downstream of the pile (zone C_1), with low wall shear stress levels and weak erosion (see Figures 6(a) and 6(b)). Figure 6(c) reveals two counter-rotating vortices on the lateral sides that interact with the separation from the crest. The complex three-dimensional structures formed in this recirculating region created a small zone with higher shear (zone D_1), in which a slight accumulation of black sand was noticeable (see Figures 6(a) and 6(b)).

Similarly, Figures 7(b) and 7(c) show a deceleration upstream pile p_2 (region A_2, with low levels of shear) and a flow acceleration towards the slope and sides (region B_2, with high levels of shear). Nevertheless, especially for the gap of $0.9h$, the dimensionless values of shear stress for the piles oriented 90° (region B_2) were higher than for the pile with no interference (region B_1), with maximum values of 8.6 and 6.9, respectively. These findings are consistent with the erosion patterns observed in Figure 7(a).

An asymmetrical pattern was detected in the experimental and numerical results, despite the symmetrical geometry. The literature reported similar behaviour of the flow around geometrical symmetric obstacles [26, 27, 28, 29] as a consequence of the bi-stable intermittent nature of the flow in which the wake switches randomly at irregular intervals from the sides of the pile between the two stable states. The numerical simulation of bi-stability is a difficult task, due to its very long timescale. The average timescale of the RANS numerical simulations may not be sufficiently large to comprise the

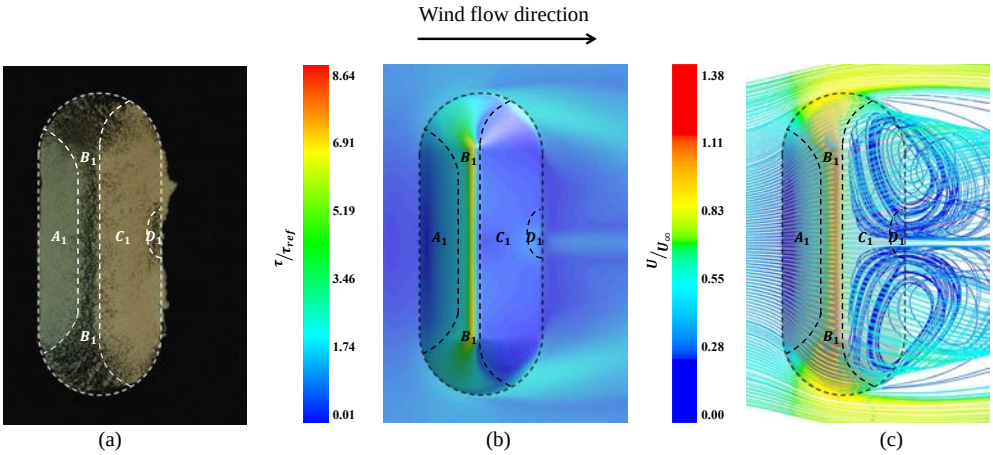

Figure 6: Experimental and numerical results for an isolated stockpile (pile p_1) exposed to a perpendicular wind flow: (a) Top view of the eroded sand stockpile after the pavement phenomenon, (b) Mean wall shear stress on the pile surface and on the ground and (c) Mean flow pathlines over the pile. Four wind erosion regions are highlighted according to the degree of wind exposure: zones A_1, B_1, C_1 and D_1.

switch of the wake timescale.

Figure 7(a) revealed an accumulation of sand on the ground between the piles for the closely spaced configuration ($0.9h$ gap). In addition, the interference of pile p_2' in the leeward wall of pile p_2 was more important in this case. When comparing the $0.9h$ gap to the $1.8h$ gap, the zone of ineffective erosion C_2 was smaller, and the black zone of high erosion D_2 was larger. For the $1.8h$ gap, the wake region of pile p_2 resembled the wake region of pile p_1 and the extent of areas C_2 were comparable, except for the narrow region of high friction that was impacted by the vortex (zone D_2) that was transposed to the lateral side due to the bi-stability.

A more severe erosive impact was observed for the second stockpile on the windward wall of pile p_2'. Figure 7(a) shows that a very high concentration of black particles in this area, which indicates a zone vulnerable to erosion, particularly with the $0.9h$ gap. In pile p_2', zone B_2' is the region with the highest shear stress values because of the impact of the vortex structure shown in Figure 7(c). On the other hand, zone A_2' has low shear levels of and the pathlines velocities were lower (see Figures 7(b) and 7(c)). Unexpectedly, the erosion patterns demonstrated that this zone was characterised

by high erosion (see Figure 7(a)). Two possible mechanisms could explain this unexpected observation: the intermittent behaviour of the vortices due to bi-stability and the impact of the emitted particles from pile p_2.

In the wake zone behind pile p'_2, the regions C'_2 and D'_2 were also highlighted. The similarity between these zones can be noticed for the $0.9h$ and $1.8h$ gaps; however, in both cases, D'_2 is larger than the corresponding zone in pile p_1 (zone D_1), which emphasises the impact on the downstream pile.

4.1.2. Stockpiles oriented $60°$ *to the main wind flow direction*

Figures 8 and 9 show the photographs after the pavement phenomenon, the mean fields of the wall shear stress distribution and the flow pathlines for, respectively, an isolated stockpile and two stockpiles oriented $60°$ to the main flow and separated by $0.9h$ and $1.8h$ gaps.

The wind exposure patterns were similar on piles p_1 and p_2 for the configurations oriented $60°$ to the main flow direction. Progressive flow acceleration up the slope and towards the lateral sides was observed on the windward wall of these piles (see Figures 8(c) and 9(c)). Zones A_1 and A_2 had low levels of shear and ineffective erosion whereas the opposite occurred in zones B_1 and B_2 (see Figures 8(a), 8(b), 9(a) and 9(b)). The highest friction levels in zones B_1 and B_2 were found on the lateral sides of the pile facing the wind. In addition, the shear peak values were higher for the $60°$ orientation than for the $90°$ orientation.

Figures 8(c) and 9(c) show that a single main helical vortex was formed downstream of the stockpiles p_1 and p_2. The flow separation near the crest of these piles led to a wake regions on the leeward wall (zone C_1 and C_2, respectively), with low wall shear stress levels and weak erosion (see Figures 8(a), 8(b), 9(a) and 9(b)). The impact of this vortex can be clearly observed in zones D_1 and D_2, a region with higher friction and significant agglomeration of black particles, although it had a weaker effect on pile p_1. Moreover, the vortex had a greater effect on the closely spaced piles. Indeed, it impinged on the windward p'_2 pile wall increasing the friction on the upper part of region B'_2.

The unexpected situation in zone A'_2 with a low shear stress level and a high erosion rate was also seen for the $60°$ orientation. This situation can be again attributed to the impact of the emitted particles from pile p_2. Further evidence supporting the effect of the saltating particles from pile p_2 on the erosion of pile p'_2 can be seen in Figure 10, which shows the final photographs and the dimensional contours of the shear stress for the

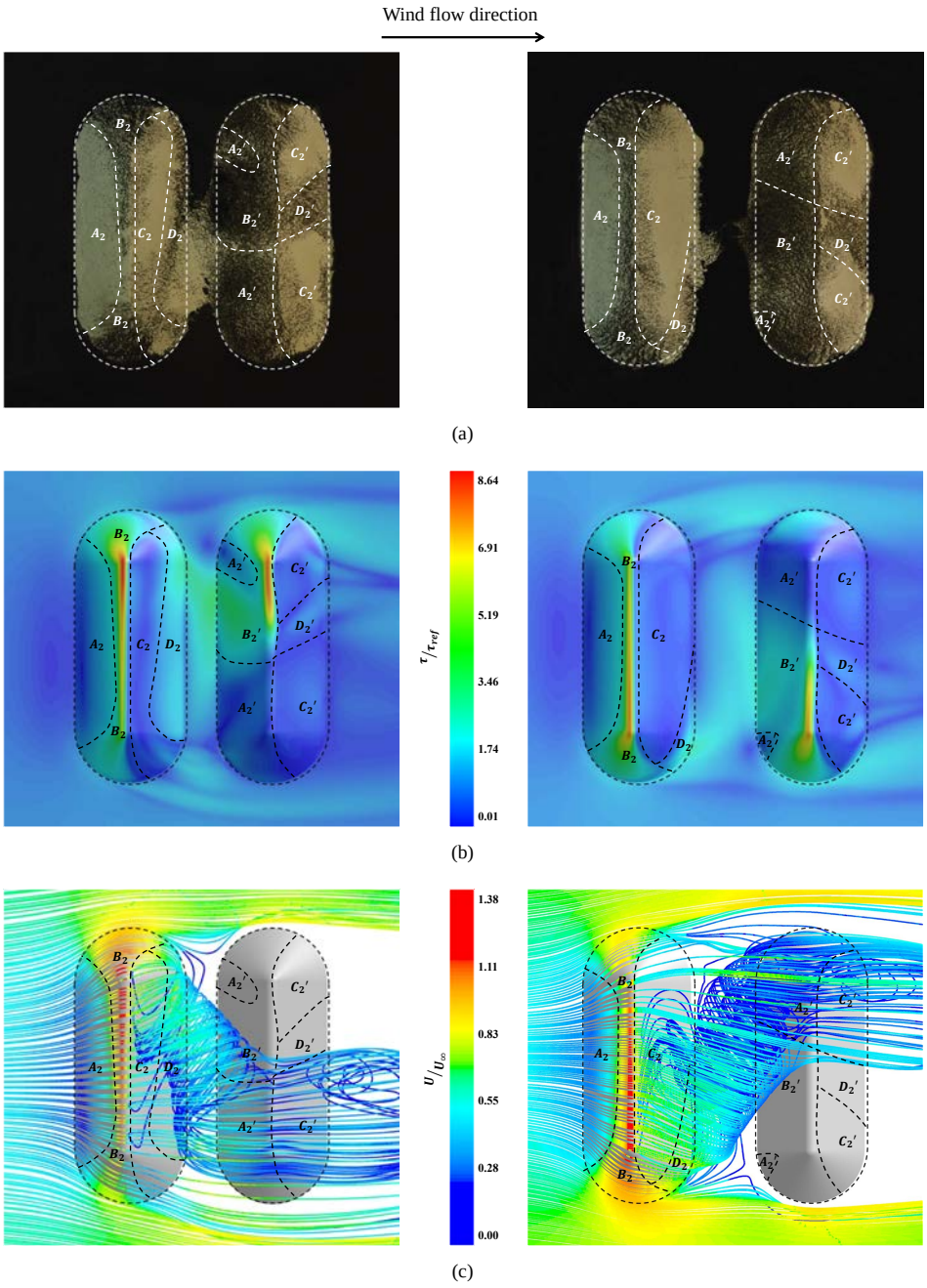

Figure 7: Experimental and numerical results for two parallel stockpiles oriented 90° separated by $0.9h$ and $1.8h$ gaps: (a) Top view of the eroded sand stockpiles after the pavement phenomenon, (b) Mean wall shear stress on the pile surfaces and on the ground and (c) Mean flow pathlines over the piles. Four wind erosion regions are highlighted on each pile, according to the degree of wind exposure: zones A_2, B_2, C_2 and D_2 in the upstream pile (pile p_2) and zones A_2', B_2', C_2' and D_2' in the downstream pile (pile p_2').

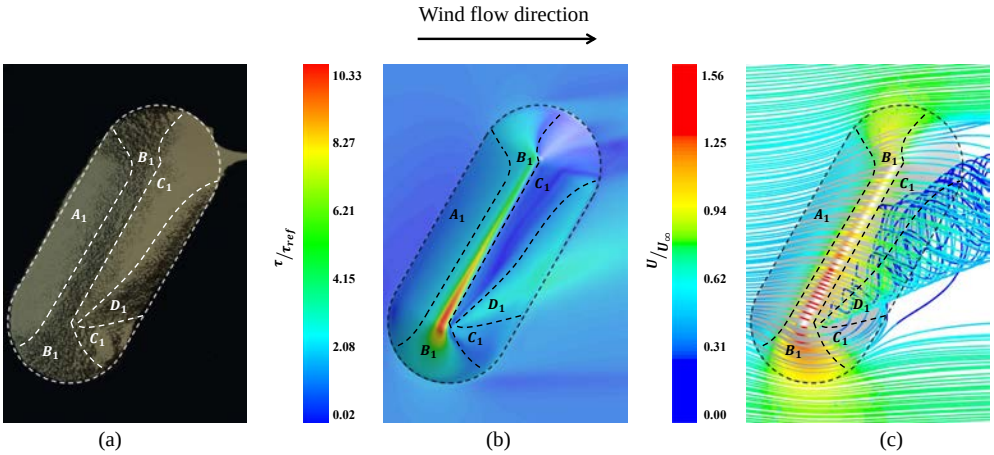

Figure 8: Experimental and numerical results for an isolated stockpile (pile p_1) oriented 60° to the main flow: (a) Top view of the eroded sand stockpile after the pavement phenomenon, (b) Mean wall shear stress on the pile surface and on the ground and (c) Mean flow pathlines over the pile. Four wind erosion regions are highlighted according to the degree of wind exposure: zones A_1, B_1, C_1 and D_1.

velocities 6 and 8 m/s with the $1.8h$ gap and $\alpha_{NE} = 20\%$. In this figure the results are presented in the dimensional form in order to compare the absolute values of the shear stress for both velocities. The highlighted area in zone B_2 (red line) was highly eroded for $U_\infty = 8$ m/s due to the high levels of shear and the windward wall of pile p_2' was also highly eroded, as shown in Figure 10(a). Accordingly, as erosion is weaker for $U_\infty = 6$ m/s, the red region in zone B_2 and its corresponding directly frontal region in pile p_2' remained uneroded (see Figure 10(b)). Similarly, the upper part of region A_2' (highlighted with blue line) was highly eroded, suggesting emissions due to the impact of saltating particles from region D_2 of pile p_2.

A significant concentration of coarse black particles in the windward wall of pile p_2', as shown in Figure 9(a), reinforces the strong impact of a second parallel stockpile on erosion, especially for the smaller gap ($0.9h$).

The patterns on the leeward walls of pile p_2' behaved in a similar manner as the leeward walls of piles p_2 although with much less erosion intensity. In Figure 9(a), zone D_2 is larger than zone D_2', especially for the $1.8h$ gap.

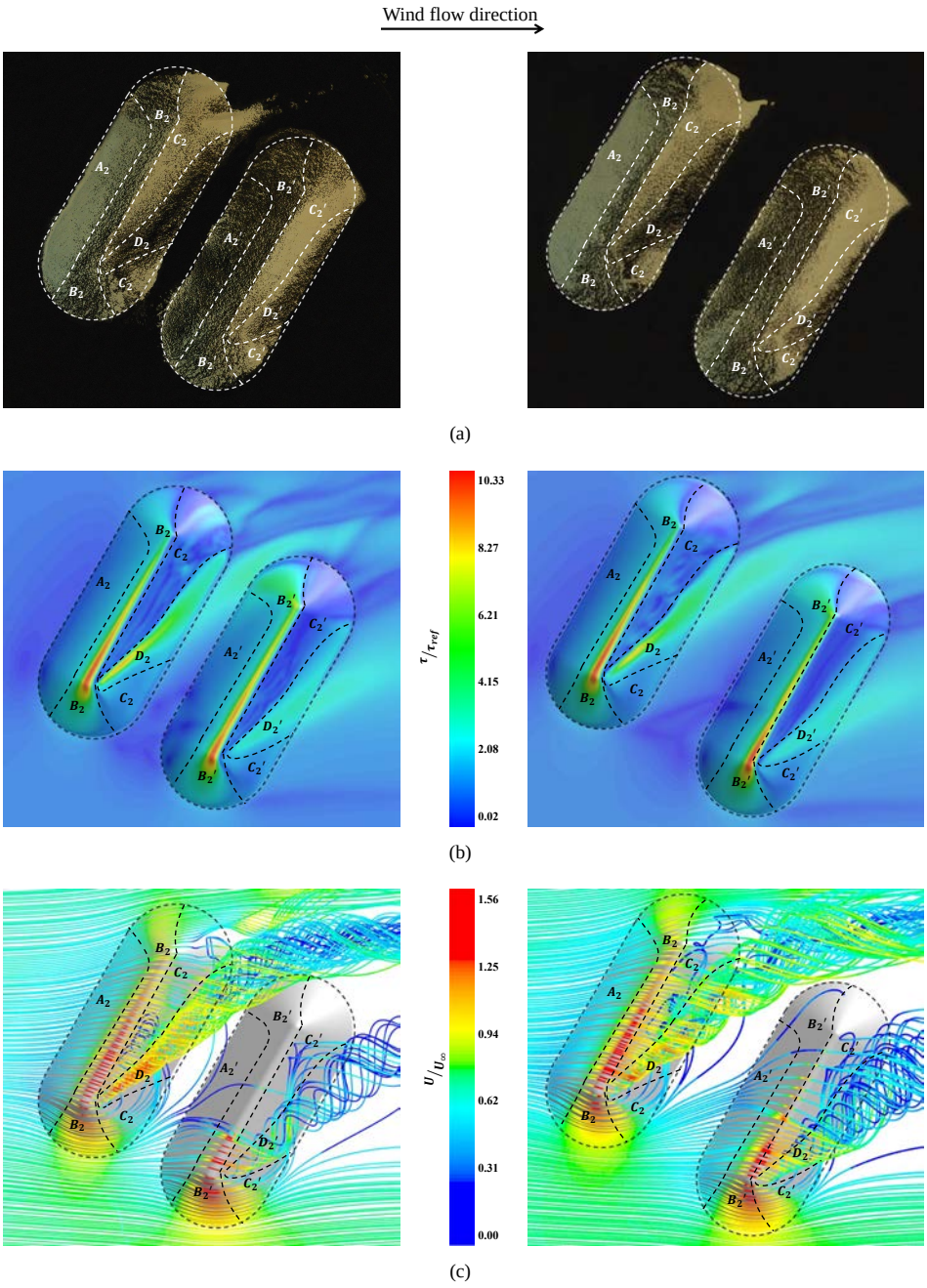

Figure 9: Experimental and numerical results for two stockpiles oriented 60° and separated by gaps $0.9h$ and $1.8h$: (a) Top view of the eroded sand stockpiles after the pavement phenomenon, (b) Mean wall shear stress on the pile surface and on the ground and (c) Mean flow pathlines over the piles. Four wind erosion regions are highlighted on each pile, according to the degree of wind exposure: zones A_2, B_2, C_2 and D_2 in the upstream pile (pile p_2) and zones A_2', B_2', C_2' and D_2' in the downstream pile (pile p_2').

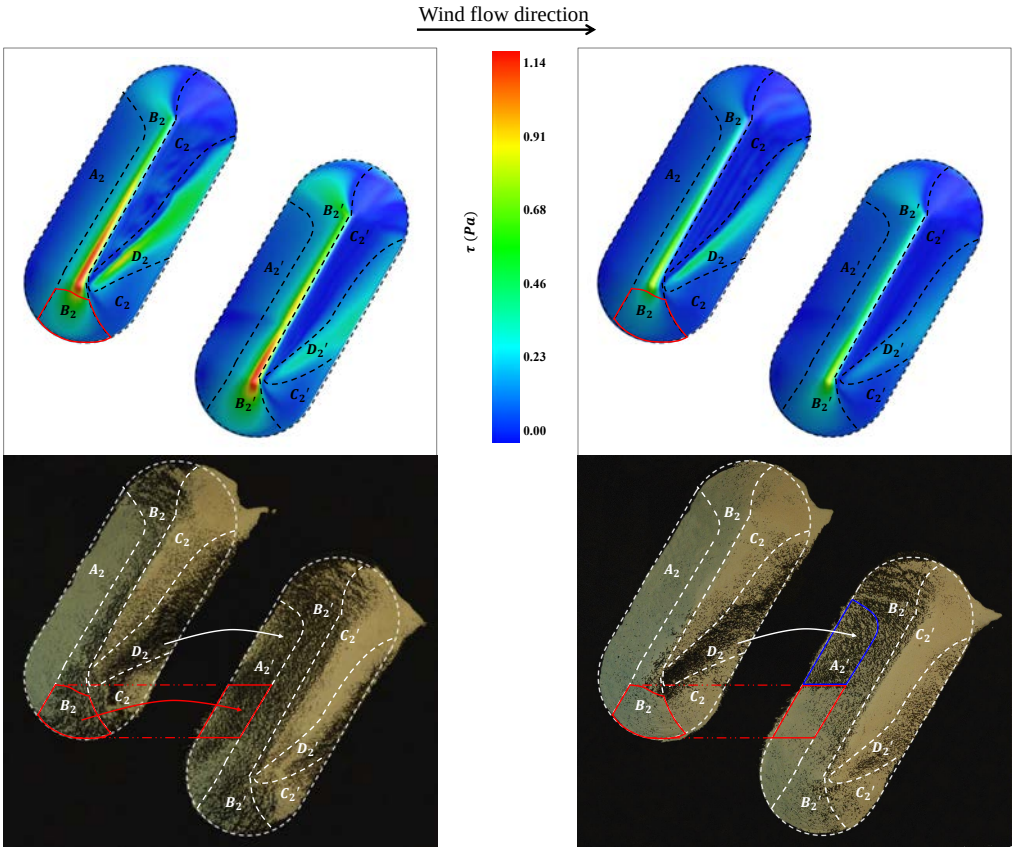

Figure 10: Impact of the emitted particles from the upstream pile p_2 in two stockpiles oriented 60° with $\alpha_{NE} = 20\%$ and separated by the $1.8h$ gap for (a) $U_\infty = 8\ m/s$ and (b) $U_\infty = 6\ m/s$

4.2. Visual analysis of the erosion patterns

igure 11 illustrates the experimental temporal evolution of wind erosion for both granulometries (with $\alpha_{NE} = 10$ and 20%) and for the lowest and highest wind velocities ($U_\infty = 6$ and 8 m/s). Considering that similar pavement phenomenon behaviour was observed for all arrangements, a configuration with an orientation 60° and a $0.9h$ gap was chosen to represent a typical case.

As mentioned in Section 2, the pavement phenomenon was observed after 15 minutes of wind exposure for all configurations, which means that the final erosion patterns are well represented in the fifth column of photographs shown in Figure 11. The extent of the final eroded areas varied little with the increase of α_{NE}, although the final concentration of non-erodible particles in these areas was higher for $\alpha_{NE} = 20\%$ than for $\alpha_{NE} = 10\%$, especially for $U_\infty = 8$ m/s. On the other hand, a significant increase of the eroded areas occurred as flow velocity increased. For instance, modifications of the windward surface of the upstream pile are almost imperceptible for $U_\infty = 6$ m/s whilst the same region was highly eroded for $U_\infty = 8$ m/s.

The temporal evolution of the pavement shown in the Figure 11 indicates that the phenomenon occurred faster in tests with a larger amount of non-erodible particles and higher velocities. Indeed, for $\alpha_{NE} = 20\%$ and $U_\infty = 8$ m/s, after 30 seconds a larger quantity of black particles accumulated than with $\alpha_{NE} = 10\%$ and $U_\infty = 6$ m/s, and after 1 minute and 30 seconds, the observed pattern was found to be very close to the final pattern. This behaviour was related to a temporal decrease in the emitted mass flux. The highest pavement rate for $\alpha_{NE} = 20\%$ supports previous findings in the literature [2].

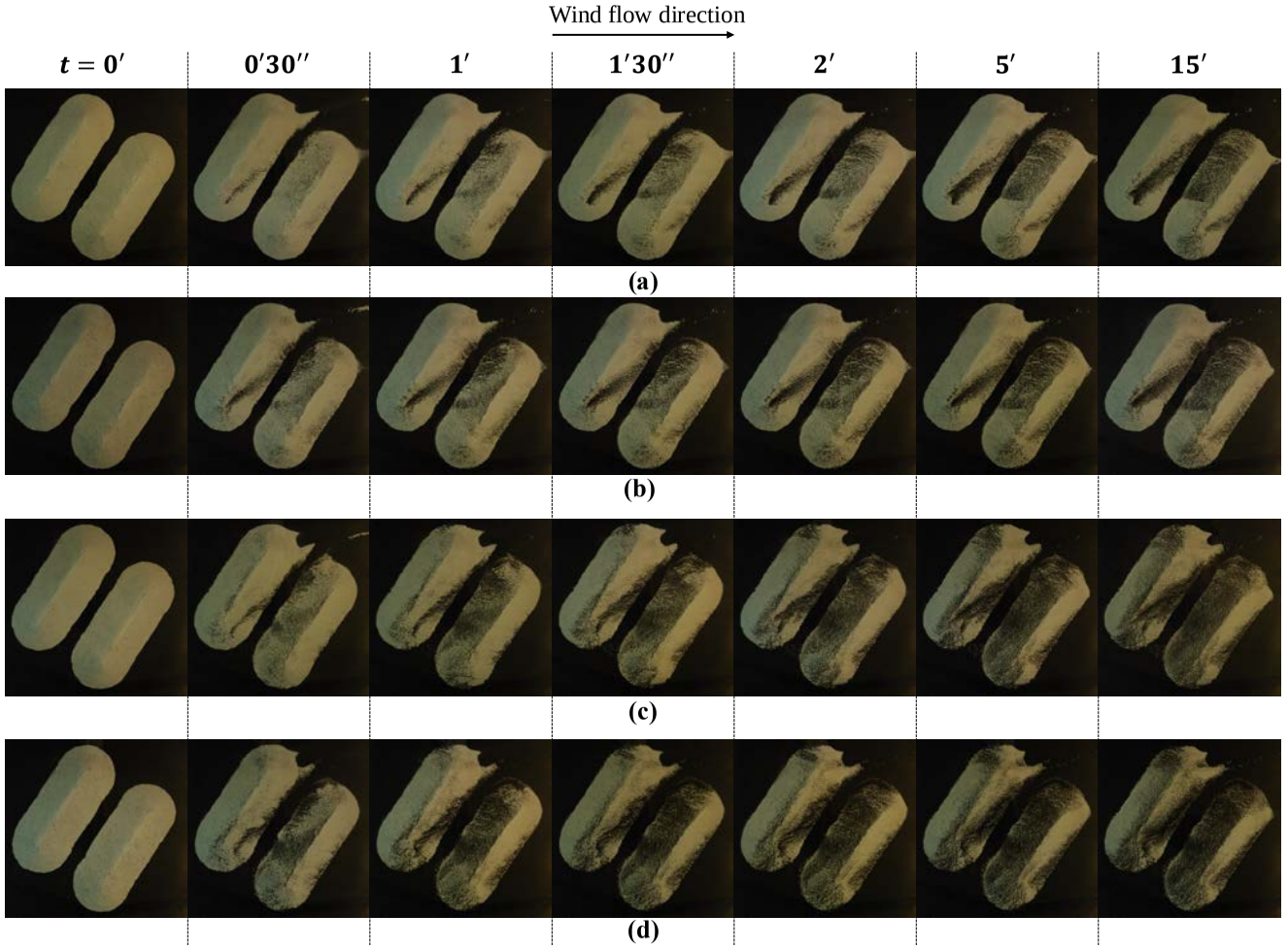

Figure 11: Temporal evolution of the pavement phenomenon for two stockpiles oriented 60° to the main flow separated by a $0.9h$ gap: $U_\infty = 6\ m/s$ with (a) $\alpha_{NE} = 10\%$ and (b) $\alpha_{NE} = 20\%$, $U_\infty = 8\ m/s$ with (c) $\alpha_{NE} = 10\%$ and (d) $\alpha_{NE} = 20\%$

4.3. Emission estimates

Table 2 shows the emitted mass measurements from an isolated stockpile (p_1) and from each stockpile in the successive arrangement (p_2 and p_2'). The first result worth noting is the remarkable amount of sand emitted from the downstream pile p_2'. In all test cases, the emissions were higher for the pile p_2', compared to either pile p_2 or p_1, which is consistent with the experimental erosion patterns discussed in Section 4.1. The reason for this result is the emissions from the upward wall of pile p_2' due to the impact of saltating particles from pile p_2 (see Figure 10).

Pile p_2' had higher emissions in the 60° arrangement if the stockpiles were separated by a $0.9h$ gap because of higher shear stress values, a greater effect of the main vortex shed from pile p_2 and interactions between the piles (more energetic saltation particles). These facts do not apply to pile p_2 (wall shear stress distribution on pile p_2 is quite similar for both gaps for the orientation of 60°), and the critical importance of the gap on the emitted mass for this pile was not observed. Nevertheless, the shear levels of pile p_2 were higher than those of pile p_1, and the amount of emitted mass was also higher.

On the other hand, with the piles oriented 90° to the main flow, pile p_2' and pile p_2 had higher emissions for stockpiles separated by a gap distance of $1.8h$. However, this result is ambiguous because, as mentioned in Section 4.1.1, an accumulation of sand in the floor between the piles was noticed for the $0.9h$ gap. This mass was not counted in the balance as emitted because it was hard to distinguish from which pile it arose (it was even hard to separate the sand from the piles). For the same reason, a rigourous comparison of the emitted mass from piles p_2 (with $0.9h$ gap) and p_1 is difficult; however, we noticed that the values were close. Nevertheless, emissions from pile p_2 were slightly lower for stockpiles separated by a gap distance of $1.8h$ than from an isolated stockpile. Therefore, the emissions of each pile in the configuration with two piles depend on the orientation of the flow. It was only the upstream pile of a pair in the 90 orientation that experienced less erosion that an isolated pile.

Figure 12 shows the total emitted mass amount from successive stockpiles compared to twice the amount from an isolated stockpile (which could mimic a situation in an open industrial yard in which the piles are far enough away from each other to not interfere) for all tested configurations. The total amount from the two successive stockpiles was greater for both orientations, and in some cases, the emitted mass could be more than three times higher, compared to two times the value from an isolated pile.

Table 2: Emitted mass measurements for an isolated stockpile and for two successive piles with gaps of $0.9h$ and $1.8h$ (h is the stockpile height)

Configuration		Emitted mass pile p_1 (g)		Emitted mass successive piles (g)				
α_{NE} (%)	U_∞ (m/s)	90°	60°	Gap	90°		60°	
					pile p_2	pile p_2'	pile p_2	pile p_2'
10	6	83.2	212.9	$0.9h$	27.8	477.1	376.3	581.6
				$1.8h$	22.2	609.0	350.3	418.7
	7	261.6	451.8	$0.9h$	160.4	647.9	464.6	816.7
				$1.8h$	191.5	801.0	521.7	677.1
	8	399.2	626.6	$0.9h$	438.4	811.8	690.5	1029.8
				$1.8h$	393.1	922.9	714.3	989.9
20	6	46.3	88.2	$0.9h$	3.2	252.0	186.4	358.2
				$1.8h$	18.7	285.4	137.5	218.1
	7	140.3	190.1	$0.9h$	135.4	345.2	197.1	451.7
				$1.8h$	103.6	420.7	238.7	365.7
	8	247.8	356.4	$0.9h$	250.7	448.3	421.9	604.1
				$1.8h$	192.9	569.1	389.0	483.7

Furthermore, Figure 12 highlights that erosion was greater in configurations with a main wind flow direction oriented 60° than in those oriented 90° to the piles, especially if the piles are separated by a gap distance of $0.9h$. In addition, for the same value of the free stream velocity, emissions with $\alpha_{NE} = 20\%$ were approximately half that of emissions with $\alpha_{NE} = 10\%$. Therefore, the proportion of non-erodible particles has a considerable effect on particle emissions.

5. Conclusion

The purpose of this study was to investigate the aeolian erosion of stockpiles with a bimodal granulometry formed by erodible and non-erodible sand using wind tunnel experiments. Numerical simulations were performed to supply wind flow data (i.e., shear stress distribution and pathlines) in order to support an understanding of the phenomenon.

Temporal evolution of the pavement phenomenon was analysed using top view photographs of the piles, studying the progress of wind erosion exposure zones. It has been verified that the phenomenon occurred faster for larger amounts of non-erodible particles and higher velocities.

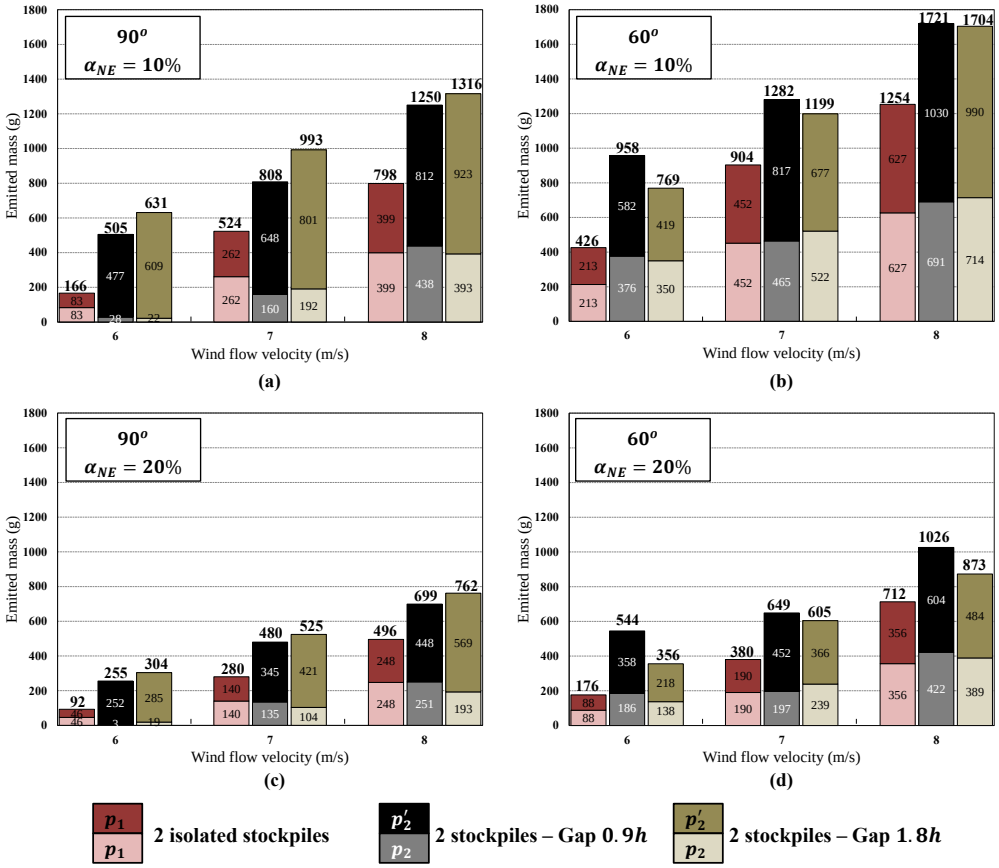

Figure 12: Experimental quantification of the total amount of emitted mass from the successive stockpiles separated by the gaps of $0.9h$ and $1.8h$ compared to twice the amount from an isolated stockpile, for the configurations: $\alpha_{NE} = 10\%$ oriented (a)90° and (b)60°, and $\alpha_{NE} = 20\%$ oriented (c)90° and (d)60°

Wind flow modifications and their effects on wind erosion were numerically and experimentally assessed for two pile orientations to the main wind flow direction (60° and 90°) and three different arrangements: an isolated stockpile and two successive stockpiles separated by $0.9h$ and $1.8h$ gaps. For the perpendicular arrangement it was observed highly eroded zones in which the incident flow accelerated on the crest and lateral sides and zones of weaker erosion downstream of the piles, after the flow separation. For the orientation of 60°, the erosion was stronger due to higher shear stress values of and the

effects of the main vortex on the leeward wall of the piles. A strong impact on the downstream pile was observed for both orientations. The downward wall of these piles had a highly eroded region, even though the shear stress values were low (zone A_2') due to the impact of the eroded particles from the upstream pile. Therefore, it is important to consider this behaviour in future numerical modelling studies. With the exception of zone A_2', good agreement was found between the numerical distribution of the wall shear stress and the agglomeration of non-erodible particles on the stockpile surface. The results indicate that, in addition to the wind velocity, the orientation of the pile to the prevailing wind direction also plays an important role to limit aeolian erosion in actual storage yards. It is recommended that the stockpiles are oriented perpendicular to the wind direction.

The experimental quantification of the mass emitted revealed that the emissions from two consecutive stockpiles are greater than twice the emissions from an isolated stockpile for both orientations. The presence of a successive pile had a strong effect and increased erosion. In other words, the total emitted mass would be underestimated if it was taken as twice the emissions calculated for an isolated stockpile. In addition, the piles oriented 60° emitted larger amounts of mass than piles oriented 90° in all configurations, especially for the $0.9h$ gap. Therefore, the results may suggest that a larger single pile has less impact than two parallel piles. However, experiments with gaps larger than $1.8h$ should be conducted.

The emission models of wind are based on the local wall friction velocity which are well transposable at the real scales. However, it is important to note that for studies involving atmospheric particle transport to describe the physics of particulate matter or sediment transport, scaling parameters considering particles characteristics should be taken into account.

Acknowledgements

The authors acknowledge the support from Capes/Cofecub, Fapes and CNPq.

References

[1] L. Li, L. Martz, Aerodynamic dislodgement of multiple-size sand grains over time, Sedimentology 42 (4) (1995) 683–694.

[2] B. Furieri, S. Russeil, J. M. Santos, J.-L. Harion, Effects of non-erodible particles on aeolian erosion: Wind-tunnel simulations of a sand oblong storage pile, Atmospheric Environment 79 (2013) 672 – 680.

[3] USEPA, Miscellaneous Sources, Industrial Wind Erosion, AP-42, 2006.

[4] C. Turpin, J.-L. Harion, Numerical modeling of flow structures over various flat-topped stockpiles height: Implications on dust emissions, Atmospheric Environment 43 (35) (2009) 5579 – 5587.

[5] C. P. Yeh, C. H. Tsai, R. J. Yang, An investigation into the sheltering performance of porous windbreaks under various wind directions, Journal of Wind Engineering and Industrial Aerodynamics 98 (10) (2010) 520–532.

[6] L. Novak, B. Bizjan, J. Pranikar, B. Horvat, A. Orbani, B. irok, Numerical Modeling of Dust Lifting from a Complex-Geometry Industrial Stockpile, Strojniki vestnik - Journal of Mechanical Engineering 61 (11) (2015) 621–631.

[7] T. Badr, J.-L. Harion, Effect of aggregate storage piles configuration on dust emissions, Atmospheric Environment 41 (2) (2007) 360 – 368.

[8] J. Toraño, R. Rodriguez, I. Diego, J. Rivas, A. Pelegry, Influence of the pile shape on wind erosion CFD emission simulation, Applied Mathematical Modelling 31 (11) (2007) 2487 – 2502.

[9] C. Turpin, J.-L. Harion, Effect of the topography of an industrial site on dust emissions from open storage yards, Environmental Fluid Mechanics 10 (6) (2010) 677–690.

[10] I. Diego, A. Pelegry, S. Torno, J. Toraño, M. Menendez, Simultaneous CFD evaluation of wind flow and dust emission in open storage piles, Applied Mathematical Modelling 33 (7) (2009) 3197 – 3207.

[11] X. Cong, S. Yang, S. Cao, Z. Chen, M. Dai, S. Peng, Effect of aggregate stockpile configuration and layout on dust emissions in an open yard, Applied Mathematical Modelling 36 (11) (2012) 5482 – 5491.

[12] B. Furieri, J.-L. Harion, J. M. Santos, M. Milliez, Comparative analysis of dust emissions: isolated stockpile vs two nearby stockpiles, Air Pollution XX, WitPress 157 (2012) 285–294.

[13] A. Ferreira, M. Fino, A wind tunnel study of wind erosion and profile reshaping of transverse sand piles in tandem, Geomorphology 139140 (0) (2012) 230 – 241.

[14] C. Turpin, Amélioration des modèles de quantification des émissions particulaires diffuses liées l'érosion éolienne de tas de stockage de matires granulaires sur sites industriels, Phd thesis, Ecole des Mines de Douai, Université de Valenciennes et du Hainaut-Cambrésis, 2010.

[15] H. Schlichting, Boundary Layer Theory, McGraw-Hill Book Compagny, 1968.

[16] B. Furieri, S. Russeil, J.-L. Harion, C. Turpin, J. M. Santos, Experimental surface flow visualization and numerical investigation of flow structure around an oblong stockpile, Environmental Fluid Mechanics 12 (6) (2012) 533–553.

[17] Y. Shao, H. Lu, A simple expression for wind erosion threshold friction velocity, Journal of Geophysical Research: Atmospheres 105 (D17) (2000) 22437–22443.

[18] J. Kok, N. Renno, Enhancement of the emission of mineral dust aerosols by electric forces, Geophysical research letters 33 (19).

[19] R. Kurose, S. Komori, Turbulence structure over a particle roughness, International journal of multiphase flow 27 (4) (2001) 673–683.

[20] A. Mollinger, F. Nieuwstadt, Measurement of the lift force on a particle fixed to the wall in the sublayer of a fully developed turbulent boundary layer, Journal of Fluid Mechanics 316 (1996) 285–306.

[21] B. Andreotti, P. Claudin, O. Pouliquen, Measurements of the aeolian sand transport saturation length, Geomorphology 123 (3) (2010) 343–348.

[22] Fluent, ANSYS Fluent User's Guide, 2013.

[23] T. Badr, J.-L. Harion, Numerical modelling of flow over stockpiles: Implications on dust emissions, Atmospheric Environment 39 (30) (2005) 5576 – 5584.

[24] J. Van Doormaal, G. Raithby, Enhancements of the SIMPLE method for predicting incompressible fluid flows, Numerical heat transfer 7 (2) (1984) 147–163.

[25] Fluent, ANSYS Gambit User's guide, 2001.

[26] M. M. Zdravkovich, Review of flow interference between two circular cylinders in various arrangements, Journal of Fluids Engineering 99 (4) (1977) 618–633.

[27] M. K. Kim, D. K. Kim, S. H. Yoon, D. H. Lee, Measurements of the flow fields around two square cylinders in a tandem arrangement, Journal of Mechanical Science and Technology 22 (2) (2008) 397–407.

[28] M. Grandemange, M. Gohlke, O. Cadot, Turbulent wake past a three-dimensional blunt body. Part 1. Global modes and bi-stability., Journal of Fluid Mechanics 722 (2013) 51–84.

[29] H. Gopalan, R. Jaiman, Numerical study of the flow interference between tandem cylinders employing non-linear hybrid URANS-LES methods, Journal of Wind Engineering and Industrial Aerodynamics 142 (2015) 111–129.

3.2 Influence of an isolated building on wind erosion of a stockpile

This section focuses on the results of the wind tunnel experiment described in Section 3.1 with different arrangements of a single cubic obstacle upstream a sand stockpile. The objective is to investigate the impact on wind erosion due to the presence of a building by comparing the obtained results with those for the isolated stockpile configuration and observing the differences in the erosion patterns and in emission estimates.

The particles constituting the piles present a bimodal granulometry of sand with 80% of fine sand and 20% of coarse sand (white and black sand, respectively, as shown in Section 3.1). Three parameters were varied during the experiments: (i) distance between the building and the pile, with gaps of 0.5 and 1.5 times the cubic model height ($H_b = 10\ cm$), (ii) orientation of the cube to the main flow, with angles of 90° (face-on) and 45° (edge-on) relative to the pile, and (iii) free stream velocities, with $U_\infty = 7$, 8 and 9 m/s. The height of the pile is equal 7.7 cm, that is, it is 77% of the building's height.

The experimental protocol of the tests was similar to the protocol followed in the experiments described in Section 3.1. The duration of the flow was 15 minutes, after which no more emissions were noticeable, that is, the pavement of the pile surface was observed. Photographs were taken every 30 seconds up to 5 minutes and a last picture was taken after 15 minutes. Finally, the emitted mass was calculated as the difference between the initial and final stockpile weights.

Numerical simulations with similar configurations as the experiments were performed to provide the wall shear stress distribution on the pile surface and the flow pathlines, which can be associated to the erosion patterns observed in the experiments. The computational setup and modelling choices are described in Section 3.1.

3.2.1 Air flow patterns and stockpiles erosion pattern

This section presents the airflow patterns over the pile, highlighting the areas of non-erodible particles agglomeration which are visualised in the tunnel experiments and the wall shear stress contours given by the numerical simulations. The numerical results are presented in the dimensionless form (τ/τ_{ref} and U/U_∞) as the airflow characteristics are equivalent for each tested velocity whilst the velocity chosen to be the representative case of the experimental results is $U_\infty = 7\ m/s$, in which the erosion patterns were easier to identify.

Figure 3.1 shows the photographs after the pavement phenomenon, the wall shear stress distribution and the pathlines for a stockpile downstream a cubic building which is oriented 90° to the wind direction. The large adverse pressure gradient upstream the cube promotes a deceleration of the fluid leading to a boundary layer separation and vortices shedding. As a consequence of the reverse flow

behind the cube, there is an accumulation of sand in region R (see Figure 3.1(a)), a zone characterised by low levels of shear, as shown in Figure 3.1(b). Figure 3.1(c) shows the complex recirculation zone downstream the cube, which clearly affects erosion on the windward wall of the pile. Therefore, in contrast with the configuration of an isolated stockpile, region A is strongly eroded for both tested gaps (specially for $0.5H_b$), which is consistent with the high levels of wall shear stress in this area. Also, an eroded zone B is noticeable for the gap $0.5H_b$ due to the stronger influence of the central vortex structure shown in Figure 3.1(c).

Figure 3.2 shows the photographs after the pavement phenomenon, the wall shear stress distribution and the pathlines for a stockpile downstream a cubic building oriented 45° to the wind direction. A bistable flow can be noticed for this case, in which an asymmetrical pattern is detected in spite of the symmetrical geometry, similarly to that reported in Section 3.1. The interaction between the pile and the cube also promotes an accumulation of sand in the zone R where shear stress is low. In addition, for this building orientation, the windward wall of the pile is even more impacted by the presence of the building as the most part of this surface is covered by black particles. The leeward side is also more affected, compared to the building orientation of 90°. Zone B is more eroded for this orientation and it is evident for both tested gaps.

3.2.2 Emission estimates

Table 3.1 shows the emitted mass measurements from the wind tunnel experiments with an isolated stockpile and a stockpile downstream a cubic building. The results reveal that emissions considerably increase due to the presence of the building, that is, the isolated stockpile emits less than the pile downstream a cubic obstacle for all tested configurations. Furthermore, if the building is oriented 45° to the main flow direction, the impact is even stronger. For instance, for 7 m/s it is more than twice the emitted mass from an isolated pile. For larger velocities, these differences are smaller, but there is still a considerable increase, reaching 82% and 40% for the gap $1.5H_b$ and velocities of 8 and 9 m/s, respectively. The smaller increase of the emitted mass with increasing wind velocity can be explained by the dynamics of the pavement process that is more efficient for higher velocities, in which the vulnerable areas are covered more rapidly by the non-erodible particles.

The emission results indicate that the increase of the gap distance between the building and the pile from $0.5H_b$ to $1.5H_b$ does not generate expressive changes in the emitted mass measurements, presenting maximum differences for $U_\infty = 7$ m/s, in which emissions decrease 15% for the building oriented 90° and increase 13% for the building oriented 45°. For the case with the obstacle oriented 45° to the wind direction, the emission from the pile separated by the gap distance $1.5H_b$ were slightly higher than with the gap distance $0.5H_b$ for all tested velocities. On the other hand, for the case with the obstacle oriented 90° to the wind direction, the emission from the pile separated by the gap distance $0.5H_b$ were higher than the emissions with gap distance equals $1.5H_b$ for the velocities of 7 and 9 m/s and

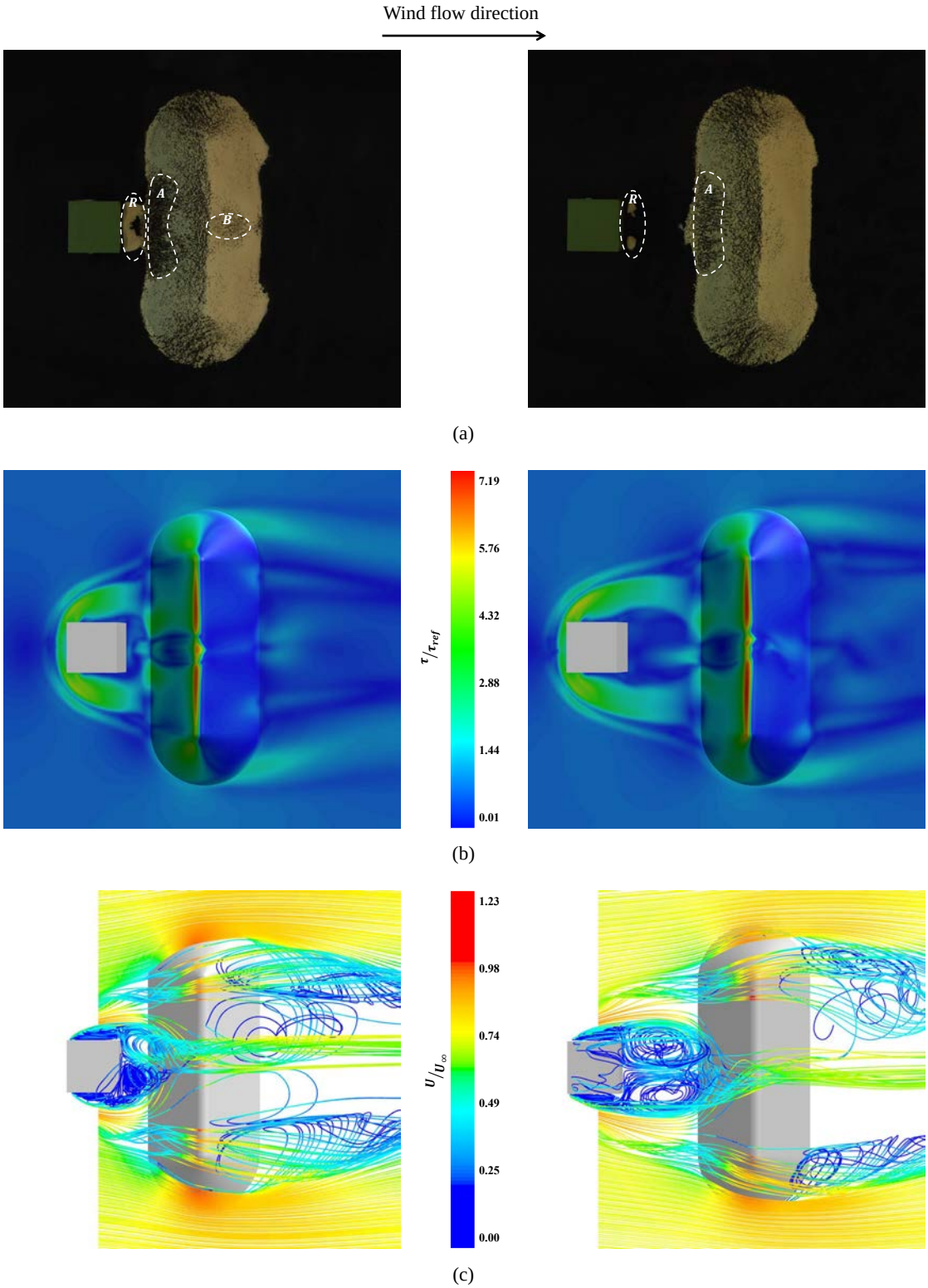

Figure 3.1: Experimental and numerical results for a stockpile downstream a cubic building with the face perpendicular to the flow, separated by gaps $0.5H_b$ and $1.5H_b$: (a) Photograph of the top view of the eroded sand stockpile after pavement, (b) Wall shear stress distribution on the pile surface and on the ground and (c) Pathlines of the flow over the pile

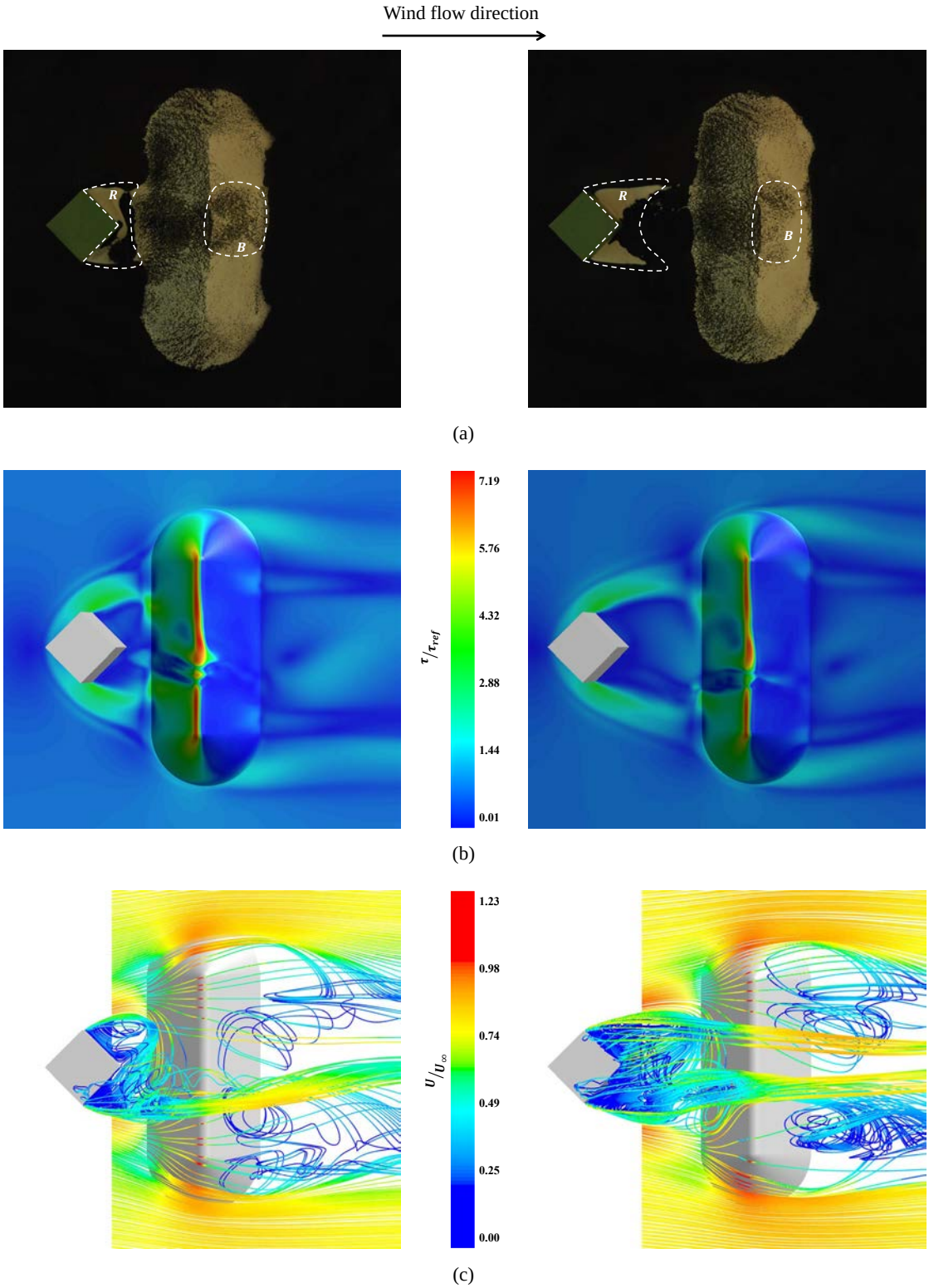

Figure 3.2: Experimental and numerical results for a stockpile downstream a cubic building oriented 45° to the main flow, separated by gaps $0.5H_b$ and $1.5H_b$: (a) Photograph of the top view of the eroded sand stockpile after pavement, (b) Wall shear stress distribution on the pile surface and on the ground and (c) Pathlines of the flow over the pile

slightly lower for the velocity of 8 m/s. However, the stockpile in the case of the smaller gap seems to present a higher accumulation of black particles (see Figure 3.1(a)). As mentioned in Section 3.2.1, there is an accumulation of sand on the ground between the cube and the pile for the gap $0.5H_b$. Therefore, the emitted mass in this case can be higher than the estimated amount presented in Table 3.1 if the accumulated sand in the middle is considered.

Table 3.1: Emitted mass measurements from an isolated stockpile and from a stockpile downstream a cubic building with gaps $0.5H_b$ and $1.5H_b$ ($H_b = 10$ cm is the building height)

U_∞ (m/s)	Isolated pile	Gap	90°	45°
7	140.3	$0.5H_b$	247.6	282.7
		$1.5H_b$	209.3	319.5
8	247.8	$0.5H_b$	325.5	413.0
		$1.5H_b$	336.2	452.5
9	387.4	$0.5H_b$	470.8	518.5
		$1.5H_b$	455.4	542.4

3.3 Extending the emission model to stockpiles

In this section, the emission model developed for beds in Section 2.1 is extended to the description of wind-blown granular stockpiles. The main differences in the modelling for stockpiles, compared to particle beds, are that the friction velocity is not constant on the pile surface and the threshold for particle motion is not uniform over the pile.

The friction velocity is not constant on the pile surface once the stockpile behaves as an obstacle and modifies the wind flow patterns. Therefore, the shear distribution over the pile is required as input data for the emission model for stockpiles. Although the model can be applied to any configuration in which the flow structure is known, in order to facilitate the discussion, the methodology presented herein mainly focuses on the case of an isolated stockpile oriented perpendicularly to the main wind flow direction.

As discussed in Section 3.1, the flow impinges the windward wall of the pile and is progressively accelerated towards the crest and the lateral sides of the pile, where the highest values of friction velocity are found (Figure 3.3). Afterwards, the flow separates from the pile surface in the crest and in the lateral sides, leading to a wake region downstream the pile, with the lowest values of friction velocity. Figure 3.4 shows the velocity field in a longitudinal plane (plane $y = 0$, in the centre of the pile) and reveals the recirculation zone behind the pile that redirects the flow towards the leeward and upwards. It is also noticeable a small reverse flow on the lower part of the windward side.

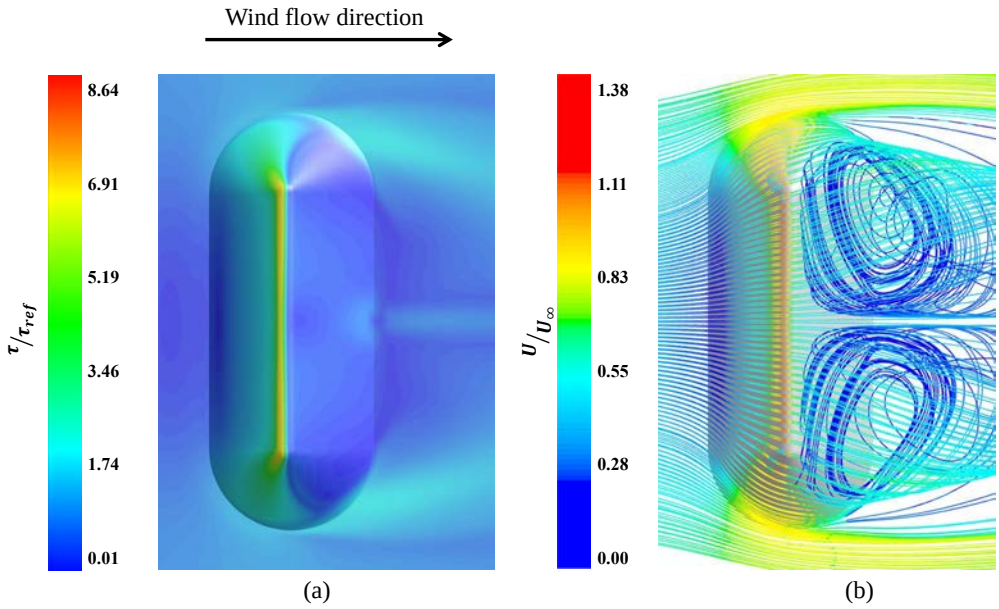

Figure 3.3: Numerical results for an isolated stockpile exposed to a perpendicular wind flow: (a) Wall shear stress distribution on the pile surface and on the ground, and (b) Pathlines over the pile

It is important to distinguish areas with different flow patterns and threshold conditions for emission, which are not uniform over the pile surface once the slope creates distinct contributions of the forces acting on the particles, as explained in Section 1.3.1.1. The local threshold friction velocity on the pile depends on the local slope and the direction of the local basal shear stress. It can be simply expressed as a function of the angles θ of the local basal shear stress with respect to the ground: $u^*_{t_s}(\theta) = f(\theta)u^*_{t_s}(0)$, where $u^*_{t_s}(0)$ is the threshold for a flat and horizontal bed (see Equation 1.39). If θ is positive (upward flow) the threshold is higher than the horizontal case ($f(\theta) > 1$), but if θ is negative (downward flow) the threshold is lower ($f(\theta) < 1$).

The angle θ is calculated with the numerical results for each cell of the pile using the vertical component of the shear stress, τ_z, as follows:

$$\theta = \arcsin\left(\frac{\tau_z}{\tau}\right) . \tag{3.1}$$

The minimum and the maximum values for θ are $-34.5°$ and $34.5°$, respectively, which corresponds to the measured angle of repose of the sand piles tested in the experiments. Figure 3.5 shows the distribution of θ over the pile surface (calculated using Equation 3.1) and the influence of θ on the threshold criterion of Shao and Lu (2000). It can be noticed that the angles on the pile are predominantly positive, which is consistent with the flow features shown in Figures 3.3. The small blue area

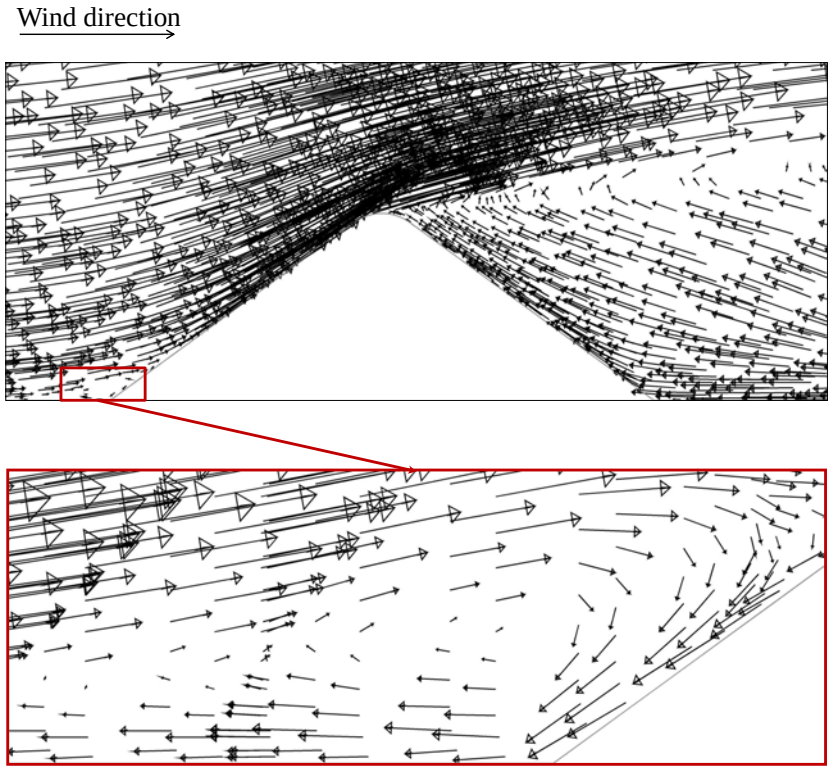

Figure 3.4: Velocity field in a transversal cut of the domain in the centre of the pile

observed in the upward wall of the pile corresponds to the reverse flow observed in Figure 3.4.

The idea of the pile emission model is to subdivide the surface of the pile. Firstly, it is subdivided in isosurfaces of constant θ, where the threshold criteria is constant. Once the threshold is defined for each part of the pile, the areas with the same degree of exposure to the wind are grouped. Thus, each one of these areas is separated in isosurfaces with constant friction velocity.

Figure 3.6 shows the isosurfaces of θ (with intervals of 5°) with its corresponding thresholds relatively to a flat surface and the distribution of the friction velocity in each one of these areas, for a flow velocity of 8 m/s.

In the model, the isosurfaces of θ and u^* are separated with intervals of 2° and 0.01 m/s, respectively, after several tests with different intervals. More refined values of θ and u^* were evaluated but the differences in the emitted mass does not exceed 1%. Thus, these values were chosen in order to reduce the computational cost.

Once the pile surface is subdivided in isosurfaces S_{θ,u^*} with a threshold criterion given by θ and a degree of exposure to the wind given by u^*, each one of these small areas is considered as a particle bed. Then, the model proposed in the Section 2.1 can be applied. It is assumed a homogeneous distribution of the particles over the pile surface, that is, an identical particle size distribution was considered for each

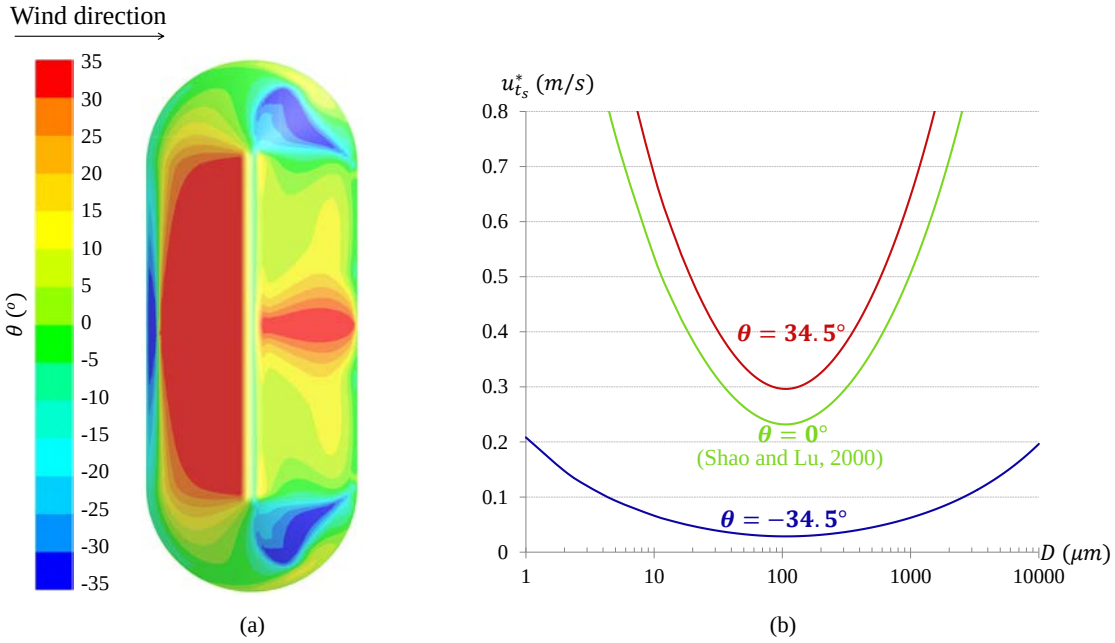

Figure 3.5: (a) Isosurfaces of constant θ and (b) the influence of θ on the threshold criterion

isosurface S_{θ,u^*}. If the particles are disposed in a pile shape, there is a natural tendency of the larger particles to roll down the slope due to gravity. Figure 3.7 shows that some of the larger particles (black sand) lie on the ground, near the pile. Furthermore, there is a larger accumulation of black sand on the round crest. Therefore, the distribution of the mixture has slight changes along the pile surface due to its shape. However, these changes will not be considered in the proposed model.

Then, all the steps to calculate the emitted mass discussed in Section 2.1 are followed: (i) given the mass fraction of particles and the flow velocity, the correspondence between the eroded depth and the cover rate is established, (ii) using the relation between R_{MIN} and H_f (Equation 18 in Section 2.1), the final eroded depth is determined, and finally, (iii) using H_f and the area of $S_{\theta,u}$, the emitted mass is calculated. In contrast with the emission model for planar beds, in the stockpile model R_{MIN} was not based on the minimum value of the dynamic threshold due to the relatively small size of the pile. It was assumed that emissions are mainly caused by aerodynamic entrainment. Therefore, the static threshold was used instead of the dynamic threshold.

The proposed model was developed for application to granular material with a particle size distribution containing non-erodible particles. If there were only erodible particles, the pile would suffer great deformations during erosion, specially due to the avalanche process. Therefore, the model for stockpiles is relevant only in the case of limited erosion.

In the wind tunnel experiments described in Section 3.1, a bimodal granu-

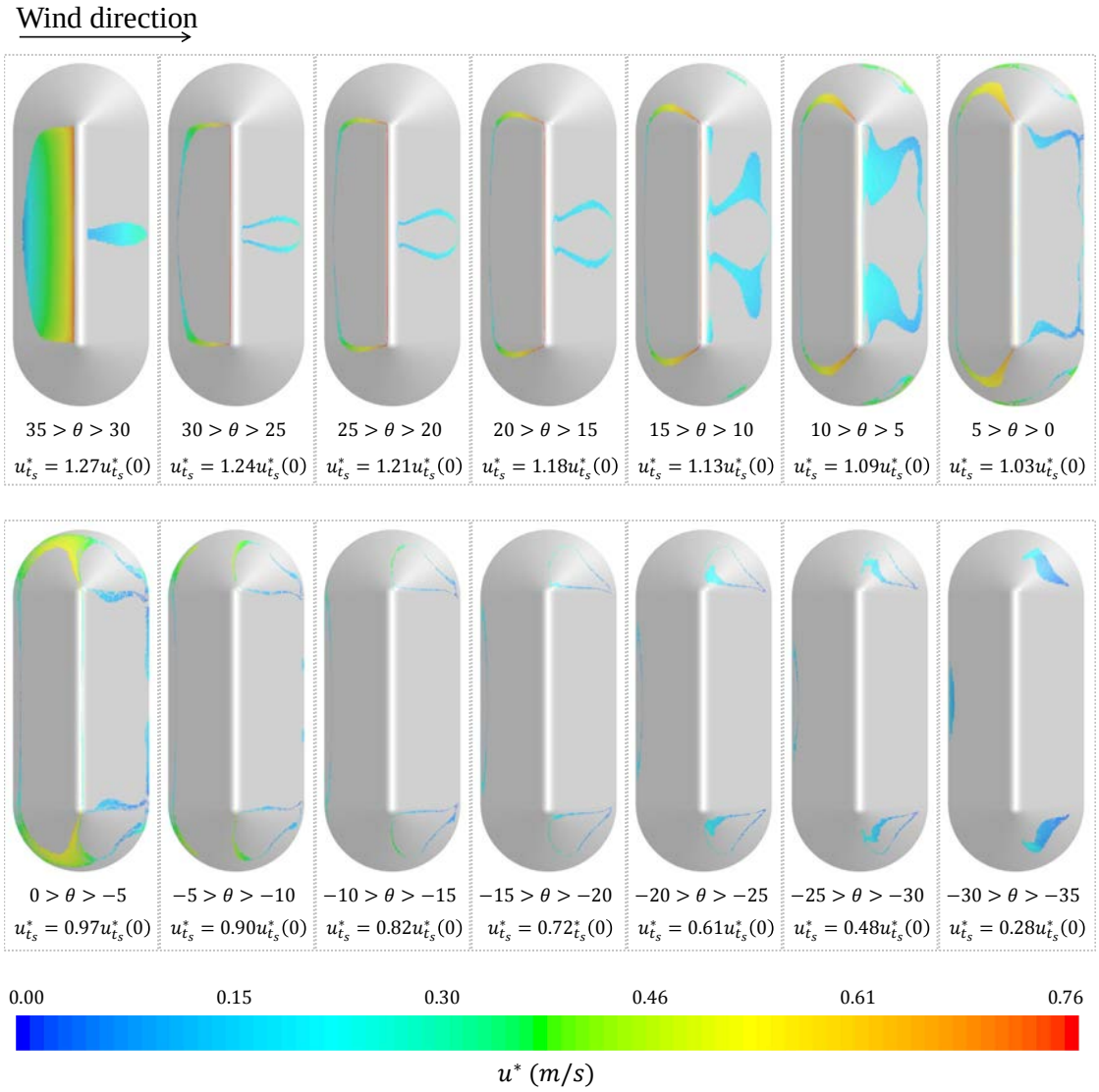

Figure 3.6: Isosurfaces of constant θ (intervals of 5°) with its corresponding thresholds relatively to a flat surface and the distribution of the friction velocity in each one of these surfaces ($U_\infty = 8$ m/s)

lometry of sand was used: fine white sand and coarse black sand with ranges of diameters from 56.0 to 194.2 μm and from 700.0 to 1300.0 μm, respectively. Among the subdivided areas of the pile, surfaces $S_{\theta,u}$ in which all black particles become erodible (areas where $u^* > u^*_{t_s}(1300)$) may be found. In this case, $u^*_S = u^*_0$, $R_{fric} = 1$ and $CR = 0$, which means that the model is not able to determine H_f using the formulation for R_{fric}. Figure 3.8 shows these problematical areas for the velocities of 6, 7 and 8 m/s, with the pile oriented 90° and 60° to the main flow direction. For the orientation of 90°, the values of shear for the velocities of 6 and 7 m/s are low enough so there are no areas containing only erodible particles. For

Figure 3.7: Top view of a sand pile with $\alpha_{NE} = 20\%$

the orientation of 60° there are areas where $u^* > u^*_{t_s}(1300)$ for all tested velocities, due to the higher levels of shear and the differences in the patterns of θ.

The areas highlighted in red (located near the pile crest) present positive values of θ, which means that the high levels of shear turn the black coarser particles to erodible particles, as the threshold in these areas are not low. The emissions in these regions are limited by the change of the pile shape on the crest, which becomes more rounded as erosion occurs. Figure 3.9 shows the contours of u_s/u_r, representing the shear stress levels over the pile, for two different rounded crests with radius $r = 1\ cm$ and $r = 5\ cm$ (the radius of the piles tested experimentally are 2 cm) and the pile oriented 90° and 60° to the main flow direction, from numerical simulations performed by Furieri (2012). As the crest becomes more rounded, the shear levels on the crest decrease, limiting further emissions.

As shown in Figure 3.8, for the orientation of 60°, the areas of the piles where the black particles become erodible present positive and negative values of θ. These zones with $\theta < 0$ are areas susceptible to avalanche, in which even small shear on the piles are enough to destabilise the surfaces, changing the pile shape to find a new stable position (with a smaller angle of repose).

It is important to notice that this problem represent a small part of the pile surface, about 1.0% of the total area of the pile for $U_\infty = 8\ m/s$ and the orientation of 90°, and 0.8%, 2.0% and 3.7% of the total area for the velocities 6, 7 and 8 m/s, respectively, and the orientation of 60°. Therefore, the changes on the pile shape as erosion occurs are not addressed in this study. In order to overcome the difficulty to estimate H_f on the problematical areas of the pile where the black particles become erodible, the following approximation in the modelling was used: all emissions from regions containing non-erodible particles were accounted and the values of H_f were registered for each case; for the isosurfaces $S_{\theta,u}$ in which all non-erodible black particles became erodible, the maximum value of H_f from the registered values was used to calculate the emissions.

Table 3.2 shows the results of modelled emissions compared to the experimental results for the orientation of 90° and 60°, including the percentage errors. There is a good agreement between the estimated and the measured mass, for both cover rates. Even so, improvements in the modelling are still needed in order to

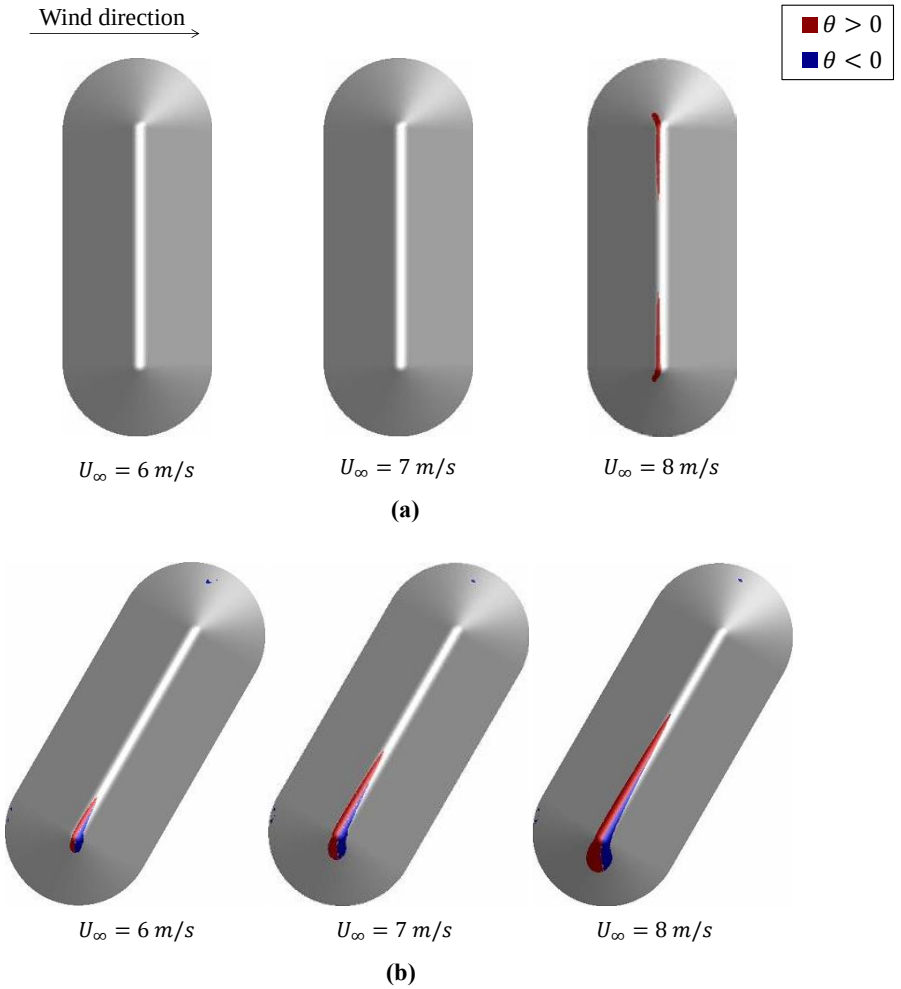

Figure 3.8: Areas on the pile surface where the black particles become erodible for the orientations of (a) 90° and (b) 60°

better represent the pile configuration. For instance, it is relevant to investigate the spatial variation of the particle size distribution on the pile surface, once the proportion of non-erodible particles have a great impact on emissions. In particular, if a higher proportion of black particles had been considered in the crest, which seems to be correct (as shown in Figure 3.7), the problematical areas without non-erodible particles would have been less representative, and the emitted mass would have been accurately estimated.

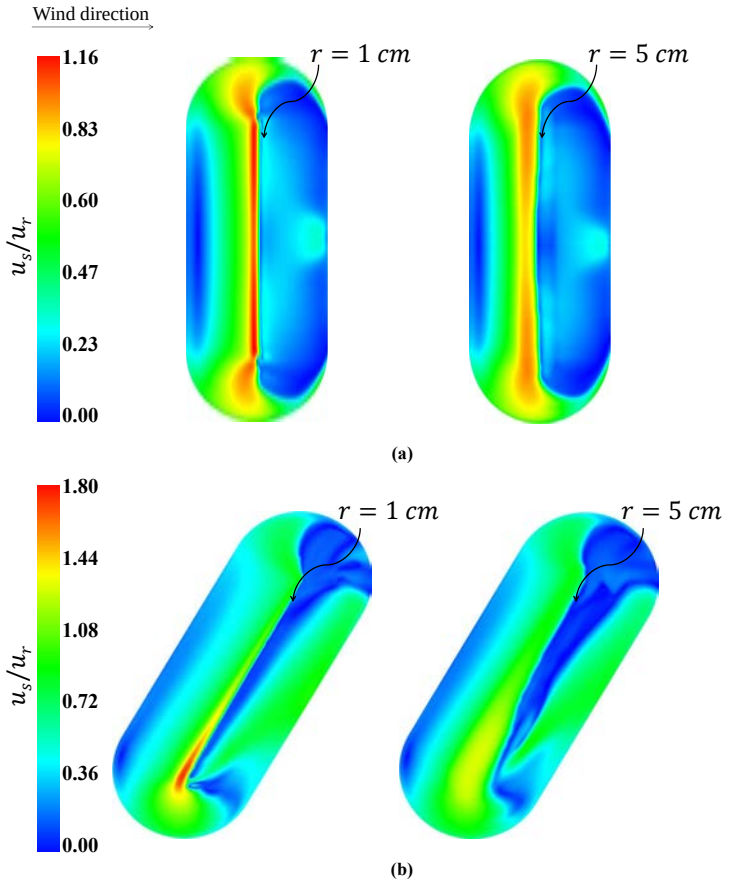

Figure 3.9: Contours of u_s/u_r for two different rounded crests with radius $r = 1\ cm$ and $r = 5\ cm$ for the orientations of (a) 90° and (b) 60°

Table 3.2: Comparison between the experimental and model results

α_{NE}	$U_\infty\ (m/s)$	Emitted mass 90° (g)			Emitted mass 60° (g)		
		Exp.	Mod.	Error	Exp.	Mod.	Error
10%	6	83.2	105.4	-26.7%	212.9	175.1	17.7%
	7	261.6	147.1	43.8%	451.8	329.9	27.0%
	8	399.2	362.6	9.2%	626.6	528.0	15.7%
20%	6	46.3	56.5	-22.0%	88.2	95.8	-8.6%
	7	140.3	79.3	43.5%	190.1	183.9	3.3%
	8	247.8	203.4	17.9%	356.4	297.2	16.6%

Chapter 4

Conclusion

In this thesis, it was proposed a model to quantify emissions due to wind erosion of granular materials considering the wide range of particle sizes of the particles. The influence of non-erodible particles on emissions was investigated by experimental and numerical approaches. The main issues addressed herein are: (i) Characteristics of turbulent flow over roughness elements representing non-erodible particles in bed of granular materials, (ii) Investigation of the pavement process, and (iii) Turbulent flow patterns observed around storage piles.

The proposed emission model takes into account two important phenomena during wind erosion: pavement and saltation. The effects of saltation were included by using the dynamic threshold instead of the static threshold. The influence of pavement was included by accounting the reduction of friction velocity on the erodible surface as erosion occurs. The friction velocity distribution over the erodible surface of a particle bed was assessed by means of numerical simulations on a domain partially covered by roughness elements. As the number and the size of the roughness elements increase, the wake zones of low shear downstream the elements increase and interact with the neighbouring elements, leading to a decrease of the mean friction velocity on the erodible surface. Previous analysis only referred to limited cases of roughness elements with cover rates lower than 12% (Turpin et al., 2010; Furieri et al., 2013a) whilst the present simulations extended cover rate values up to 40%. It was revealed that the mathematical form of the relation proposed by Furieri et al. (2013a) for the wall friction as a function of the geometrical parameters of the roughness elements (diameter, emergent height and cover rate) is still valid, but the numerical constants needed to be modified in order to cover the large range of real cases.

The numerical findings enabled the modelling of the pavement process as the non-erodible particles accumulate on the particle bed surface. The model successfully predicts the decrease on emissions as the proportion of non-erodible particles increase. In addition, the cover rate of non-erodible particles after the pavement phenomenon was quantified. Wind tunnel experiments with sand beds using a bimodal granulometry (containing fine and coarse sand) were carried out in or-

der to validate the emission model. A good agreement was found between the prediction of the model and the experimental results.

The emission model was extended to describe the erosion of granular stockpiles. The inclination of the surface modifies the erodibility of the particles: (i) the non-uniform friction velocity distribution on the pile surface, and (ii) the differences on the threshold friction velocity due to the inclination of the surface. Therefore, the idea of the model is to subdivide the pile in isosurfaces in which the threshold conditions and the friction velocity are constant and then treat each one of these areas as a different source where the emission model can be applied. Wind tunnel experiments with sand piles using a bimodal granulometry (containing fine and coarse sand) were carried out in order to validate the stockpile emission model. A good agreement was found between the modelled and the experimental results.

The impacts of a second stockpile and a building upstream the pile on emissions were also investigated. It was found that the flow interferences between the two piles increase emissions and the global amount can be more than twice the emissions from an isolated pile. The pile downstream the flow is much more affected than the pile upstream. The particles from the upstream pile impact the downstream pile, promoting more ejections. Furthermore, it was found that the changes on the flow due to the presence of the building increase emissions, especially from the upstream part of the pile.

Chapter 5

Perspectives for future work

The model proposed in this study is an important step towards a more accurate assessment of emissions from wind erosion of granular material beds and stockpiles. However, there are limitations in the model and further research is still needed. Moreover, research is also needed to investigate the pavement process in more general situations for applications to real conditions such as those found on industrial sites. The additional work recommendations are outlined bellow:

- Test and evaluate model predictions with different particle size distributions. The model was assessed using a monodisperse size distribution of non-erodible particles. Further experimental tests are necessary to investigate the effects of a wider diameter range of non-erodible particles. It is important to validate the model for granular materials closer to real size distributions found on industrial sites such as ores and coals. In addition, erodible and non-erodible particles kept their properties in the tests carried out in the present study, for all tested wind velocities. In order to provide measurements closer to real size distributions of granular materials on industrial sites, it is suggested to carry out experiments with a third mode of particles between the two previous. This range of particles sizes would then be non-erodible for low velocities and become erodible as the velocity increases.

- Particulate matter such as PM_{10} and $PM_{2.5}$, which are most interesting concerning air quality, were not investigated in this study. Therefore, it is recommended to improve the modelling by including a suspension criterion for emissions, investigating the different behaviour of the particles after entrainment, that is, transport and deposition of particles.

- Include the influence of moisture, temperature and atmospheric stability conditions on the emission model. Moisture can be included in the model as a modification in the take-off criterion with an additional cohesive force

between the particles. Then, the influence of cohesion needs to be investigated in more details by both theoretical and experimental techniques. The atmospheric stability conditions can be considered by means of numerical simulations comprising the energy conservation equation to include the heat exchange between the surface and the atmospheric flow.

- Consider the influence of the spatial distribution of the particles over the pile surface. It was assumed a homogeneous distribution of the particles over the pile surface as input data for the model. However, the real particle size distribution changes along the pile surface (larger concentration of coarse particles on the round crest and on the basis of the pile) due to its shape. Therefore, future studies should focus on enhancing the quality of the model considering the differences on the distribution of the particles over the pile. Techniques of digital analysis of the pile photographs can be used in order to investigate this issue.

- Include in the model the changes on the pile shape as erosion occurs. It has been noticed that the areas on the pile with high shear stress levels or very low thresholds can be unstable and the pile may change its shape to adjust to the erosion process and the flow. Therefore, it is suggested to perform numerical simulations in which the mesh is adapted as particles are emitted in order to investigate the evolution of the friction velocity distribution as the format of the pile modifies.

- Perform further numerical simulations of the flow over granular material beds in order to investigate the influence of non-erodible particles on the friction velocity distribution using Large Eddy Simulation (LES) methodology. The RANS steady simulations carried out in this thesis present only the mean field. The implementation of LES would assess more precisely the wind friction velocity enabling the study in greater detail of the vortical structures formed around the non-erodible particles and the evolution of the production of turbulence with the gradual increase of the surface cover.

- Evaluate the emission model to different configurations of stockpiles such as alternative shapes of piles and piles with the presence of an obstacle. Nonetheless, an important issue to resolve for future studies is to include in the modelling the extra emissions due to the impact of particles from other sources, a situation that was detected for example with the two parallel stockpiles. In addition, it is interesting to investigate the influence of more complex configurations (representing a real yard) on emissions both experimentally and numerically.

- Perform similarity analyses between the wind tunnel model and a real pile in order to accurately represent the field behaviour. The key parameters to be considered are: particle size distribution, size of the pile, height of the boundary layer and wind velocity.

References

Alfonsi, G. (2009). Reynolds-averaged navier–stokes equations for turbulence modeling. *Applied Mechanics Reviews*, 62(4):040802.

Almeida, M., Andrade Jr, J., and Herrmann, H. (2007). Aeolian transport of sand. *The European Physical Journal E*, 22(3):195–200.

Anderson, R. and Haff, P. (1991). Wind modification and bed response during saltation of sand in air. In Barndorff-Nielsen, O. and Willetts, B., editors, *Aeolian Grain Transport 1*, volume 1 of *Acta Mechanica Supplementum*, pages 21–51. Springer Vienna.

Andreotti, B. (2004). A two-species model of aeolian sand transport. *Journal of Fluid Mechanics*, 510:47–70.

Andreotti, B. and Claudin, P. (2012). *Physics of Sediment and Aeolian Transport*, pages 223–252. John Wiley & Sons, Inc.

Argyropoulos, C. and Markatos, N. (2015). Recent advances on the numerical modelling of turbulent flows. *Applied Mathematical Modelling*, 39(2):693–732.

Badr, T. (2007). *Quantification des émissions atmosphériques diffuses de particules produites par érosion éolienne. Quantification of fugitive dust emissions produced by wind erosion.* Phd thesis, Ecole des Mines de Douai, Université de Valenciennes et du Hainaut-Cambrésis.

Badr, T. and Harion, J.-L. (2005). Numerical modelling of flow over stockpiles: Implications on dust emissions. *Atmospheric Environment*, 39(30):5576 – 5584.

Badr, T. and Harion, J.-L. (2007). Effect of aggregate storage piles configuration on dust emissions. *Atmospheric Environment*, 41(2):360 – 368.

Bagnold, R. (1941). *The physics of blown sand and desert dunes*, volume 265. Methuen, London, reprint edition.

Berzi, D., Jenkins, J., and Valance, A. (2015). Periodic saltation over hydrodynamically rough beds: aeolian to aquatic. *Journal of Fluid Mechanics*, 786:190–209.

Blackwelder, R. and Haritonidis, J. (1983). Scaling of the bursting frequency in turbulent boundary layers. *Journal of Fluid Mechanics*, 132:87–103.

Blazek, J. (2015). *Computational fluid dynamics: principles and applications*. Butterworth-Heinemann.

Brown, S., Nickling, W. G., and Gillies, J. A. (2008). A wind tunnel examination of shear stress partitioning for an assortment of surface roughness distributions. *Journal of Geophysical Research: Earth Surface*, 113(F2).

Claudin, P. and Andreotti, B. (2006). A scaling law for aeolian dunes on mars, venus, earth, and for subaqueous ripples. *Earth and Planetary Science Letters*, 252(1):30–44.

Cong, X., Yang, S., Cao, S., Chen, Z., Dai, M., and Peng, S. (2012). Effect of aggregate stockpile configuration and layout on dust emissions in an open yard. *Applied Mathematical Modelling*, 36(11):5482 – 5491.

Cornelis, W. M., Gabriels, D., and Hartmann, R. (2004). A parameterisation for the threshold shear velocity to initiate deflation of dry and wet sediment. *Geomorphology*, 59(1):43–51.

Crawley, D. and Nickling, W. (2003). Drag partition for regularly-arrayed rough surfaces. *Boundary-Layer Meteorology*, 107(2):445–468.

Creyssels, M., Dupont, P., Moctar, A. O. E., Valance, A., Cantat, I., Jenkins, J., Pasini, J., and Rasmussen, K. (2009). Saltating particles in a turbulent boundary layer: Experiment and theory. *Journal of Fluid Mechanics*, 625:47–74.

Descamps, I. (2004). *Erosion éolienne d'un lit de particules à large spectre granulométrique. Wind erosion of a bed of particles with a wide size distribution*. Phd thesis, Ecole des Mines de Douai, Université de Valenciennes et du Hainaut-Cambrésis.

Descamps, I., Harion, J.-L., and Baudoin, B. (2005). Taking-off model of particles with a wide size distribution. *Chemical Engineering and Processing: Process Intensification*, 44(2):159–166.

Durán, O., Claudin, P., and Andreotti, B. (2011). On aeolian transport: Grain-scale interactions, dynamical mechanisms and scaling laws. *Aeolian Research*, 3(3):243 – 270.

Foucaut, J.-M. and Stanislas, M. (1996). Take-off threshold velocity of solid particles lying under a turbulent boundary layer. *Experiments in Fluids*, 20(5):377–382.

Furieri, B. (2012). *Erosion éolienne de tas de stockage de matières granulaires sur sites industriels : amélioration des méthodes de quantification*. PhD thesis, École Doctorale Sciences Pour l'Ingénieur, Mines Douai.

Furieri, B., Harion, J.-L., Milliez, M., Russeil, S., and Santos, J. M. (2013a). Numerical modelling of aeolian erosion over a surface with non-uniformly distributed roughness elements. *Earth Surface Processes and Landforms*, 39(2):156–166.

Furieri, B., Russeil, S., Santos, J. M., and Harion, J.-L. (2013b). Effects of non-erodible particles on aeolian erosion: Wind-tunnel simulations of a sand oblong storage pile. *Atmospheric Environment*, 79(0):672 – 680.

Gillette, D. and Stockton, P. (1989). The effect of nonerodible particles on wind erosion of erodible surfaces. *Journal of Geophysical Research: Atmospheres*, 94(D10):12885–12893.

Gillies, J., Nickling, W., and King, J. (2007). Shear stress partitioning in large patches of roughness in the atmospheric inertial sublayer. *Boundary-layer meteorology*, 122(2):367–396.

Greeley, R. and Iversen, J. D. (1985). *Wind as a Geological Process on Earth, Mars, Venus and Titan*. Cambridge University Press, New York.

Ho, T., Valance, A., Dupont, P., and Ould El Moctar, A. (2011). Scaling laws in aeolian sand transport. *Physical Review Letters,*, 106(9):094501.

Ho, T., Valance, A., Dupont, P., and Ould El Moctar, A. (2014). Aeolian sand transport: Length and height distributions of saltation trajectories. *Aeolian Research*, 12:65–74.

Ho, T.-D. (2012). *Etude expérimentale du transport de particules dans une couche limite turbulent*. PhD thesis, Université de Rennes 1.

Hsu, S. (1971). Wind stress criteria in eolian sand transport. *Journal of Geophysical Research*, 76(36):8684–8686.

Iversen, J., Wang, W., Rasmussen, K., Mikkelsen, H., and Leach, R. (1991). Roughness element effect on local and universal saltation transport. In Barndorff-Nielsen, O. and Willetts, B., editors, *Aeolian Grain Transport*, volume 2 of *Acta Mechanica Supplementum*, pages 65–75. Springer Vienna.

Iversen, J. and White, B. (1982). Saltation threshold on earth, mars and venus. *Sedimentology*, 29(1):111–119.

Iversen, J. D. and Rasmussen, K. R. (1994). The effect of surface slope on saltation threshold. *Sedimentology*, 41(4):721–728.

Jenkins, J. T. and Valance, A. (2014). Periodic trajectories in aeolian sand transport. *Physics of Fluids*, 26(7):073301.

Jimenez, J. and Moin, P. (1991). The minimal flow unit in near-wall turbulence. *Journal of Fluid Mechanics*, 225:213–240.

Kawamura, R. (1951). Study on sand movement by wind(relationship between sand flow and wind friction, and vertical density distribution of sand). *Tokyo Daigaku Rikogaku Kenkyusho Hokoku,(Tokyo)*, 5(3):95–112.

King, J., Nickling, W. G., and Gillies, J. A. (2005). Representation of vegetation and other nonerodible elements in aeolian shear stress partitioning models for predicting transport threshold. *Journal of Geophysical Research: Earth Surface*, 110(F4).

Kok, J., Mahowald, N., Fratini, G., Gillies, J., Ishizuka, M., Leys, J., Mikami, M., Park, M.-S., Park, S.-U., Van Pelt, R., and Zobeck, T. (2014). An improved dust emission model - part 1: Model description and comparison against measurements. *Atmospheric Chemistry and Physics*, 14(23):13023–13041.

Kok, J., Parteli, E., Michaels, T., and Karam, D. (2012). The physics of wind-blown sand and dust. *Reports on Progress in Physics*, 75(10):106901.

Lee, B. and Soliman, B. (1977). An investigation of the forces on three dimensional bluff bodies in rough wall turbulent boundary layers. *Journal of Fluids Engineering*, 99(3):503–509.

Lettau, K. and Lettau, H. (1978). xperimental and micrometeorological field studies of dune migration. Exploring the Worlds Driest Climate 101, University of Wisconsin, Madison.

Li, A. and Shao, Y. (2003). Numerical simulation of drag partition over rough surfaces. *Boundary-Layer Meteorology*, 108(3):317–342.

Lyles, L. and Allison, B. (1975). Wind erosion: The protective role of simulated standing stubble. *American Society of Agricultural Engineering*, 19(1):61–64.

Lyles, L., Schrandt, R. L., and Schmeidler, N. F. (1976). How aerodynamic roughness elements control sand movement. *TRANSACTIONS of the ASAE*, 17(1):134–139.

Marshall, J. (1971). Drag measurements in roughness arrays of varying density and distribution. *Agricultural Meteorology*, 8(0):269–292.

Marticorena, B. and Bergametti, G. (1995). Modeling the atmospheric dust cycle: 1. design of a soil-derived dust emission scheme. *Journal of Geophysical Research: Atmospheres*, 100(D8):16415–16430.

Mckenna Neuman, C. and Nickling, W. (1995). Aeolian sediment flux decay: Nonlinear behaviour on developing deflation lag surfaces. *Earth Surface Processes and Landforms*, 20(5):423–435.

Menter, F. (1992). Influence of freestream values on k-omega turbulence model predictions. *AIAA journal*, 30(6):1657–1659.

Menter, F. (1994). Two-equation eddy-viscosity turbulence models for engineering applications. *AIAA Journal*, 32(8):1598–1605.

Mollinger, A. and Nieuwstadt, F. (1996). Measurement of the lift force on a particle fixed to the wall in the sublayer of a fully developed turbulent boundary layer. *Journal of Fluid Mechanics*, 316:285–306.

Musick, H., Trujillo, S., and Truman, C. (1996). Wind-tunnel modelling of the influence of vegetation structure on saltation threshold. *Earth Surface Processes and Landforms*, 21(7):589–605.

Musick, H. B. and Gillette, D. A. (1990). Field evaluation of relationships between a vegetation structural parameter and sheltering against wind erosion. *Land Degradation & Development*, 2(2):87–94.

Nickling, W. and McKenna Neuman, C. (2009). Aeolian sediment transport. In Parsons, A. and Abrahams, A., editors, *Geomorphology of Desert Environments*, pages 517–555. Springer.

Nikuradse, J. (1933). Laws of flow in rough pipes. In *VDI Forschungsheft*.

Owen, P. (1964). Saltation of uniform grains in air. *Journal of Fluid Mechanics*, 20:225–242.

Pope, S. (2000). *Turbulent Flows*. Cambridge University Press.

Raupach, M. (1992). Drag and drag partition on rough surfaces. *Boundary-Layer Meteorology*, 60(4):375–395.

Raupach, M., Gillette, D., and Leys, J. (1993). The effect of roughness elements on wind erosion threshold. *Journal of Geophysical Research: Atmospheres*, 98(D2):3023–3029.

Ren, S. and Huang, N. (2010). A numerical model of the evolution of sand saltation with consideration of two feedback mechanisms. *The European Physical Journal E*, 33(4):351–358.

Santos, J. M. (2000). *Flow and Dispersion Around Isolated Buildings*. PhD thesis, Department of Chemical Engineering. University of Manchester, England.

Schlichting, H. (1936). Experimentelle untersuchungen zum rauhigkeitsproblem. *Ingenieur-Archiv*, 7(1):1–34.

Schlichting, H. (1979). *Boundary-Layer Theory*. 7 edition.

Shao, Y. (2008). *Physics and Modelling of Wind Erosion*, volume 37. Springer, 2nd revised and expanded edition.

Shao, Y. and Lu, H. (2000). A simple expression for wind erosion threshold friction velocity. *Journal of Geophysical Research: Atmospheres*, 105(D17):22437–22443.

Sherman, D., Li, B., Ellis, J., Farrell, E., Maia, L., and Granja, H. (2013). Recalibrating aeolian sand transport models. *Earth Surface Processes and Landforms*, 38(2):169–178.

Toraño, J., Rodriguez, R., Diego, I., Rivas, J., and Pelegry, A. (2007). Influence of the pile shape on wind erosion CFD emission simulation. *Applied Mathematical Modelling*, 31(11):2487 – 2502.

Turpin, C., Badr, T., and Harion, J.-L. (2010). Numerical modelling of aeolian erosion over rough surfaces. *Earth Surface Processes and Landforms*, 35(12):1418–1429.

Turpin, C. and Harion, J.-L. (2009). Numerical modeling of flow structures over various flat-topped stockpiles height: Implications on dust emissions. *Atmospheric Environment*, 43(35):5579 – 5587.

Ungar, J. E. and Haff, P. K. (1987). Steady-state saltation in air. *Sedimentology*, 34(2):289–299.

USEPA (2006). *Miscellaneous Sources, Industrial Wind Erosion, AP-42*.

Valance, A., Rasmussen, K. R., Ould El Moctar, A., and Dupont, P. (2015). The physics of aeolian sand transport. *Comptes Rendus Physique*, 16(1):105–117.

Walker, I. and Nickling, W. (2002). Dynamics of secondary airflow and sediment transport over and in the lee of transverse dunes. *Progress in Physical Geography*, 26(1):47–75.

Walter, B., Gromke, C., and Lehning, M. (2012). Shear-stress partitioning in live plant canopies and modifications to raupach's model. *Boundary-Layer Meteorology*, 144(2):217–241.

WHO (2006). *WHO Air Quality Guidelines for Particulate Matter, Ozone, Nitrogen Dioxide and Sulfur Dioxide. Global update 2005. Summary of Risk Assessment*. World Health Organization.

Wolfe, S. and Nickling, W. (1996). Shear stress partitioning in sparsely vegetated desert canopies. *Earth Surface Processes and Landforms*, 21(7):607–619.

Yu, L. and Righetto, A. (2001). Depth-averaged turbulence k–w model and applications. *Advances in Engineering Software*, 32(5):375–394.

Zimon, A. (1982). *Adhesion of dust and powder*. Springer.

Zingg, A. (1953). Wind tunnel studies of the movement of sedimentary material. In *Proceedings of the 5th Hydraulic Conference Bulletin*, volume 34, pages 111–135.